



저작자표시-비영리-변경금지 2.0 대한민국

이용자는 아래의 조건을 따르는 경우에 한하여 자유롭게

- 이 저작물을 복제, 배포, 전송, 전시, 공연 및 방송할 수 있습니다.

다음과 같은 조건을 따라야 합니다:



저작자표시. 귀하는 원저작자를 표시하여야 합니다.



비영리. 귀하는 이 저작물을 영리 목적으로 이용할 수 없습니다.



변경금지. 귀하는 이 저작물을 개작, 변형 또는 가공할 수 없습니다.

- 귀하는, 이 저작물의 재이용이나 배포의 경우, 이 저작물에 적용된 이용허락조건을 명확하게 나타내어야 합니다.
- 저작권자로부터 별도의 허가를 받으면 이러한 조건들은 적용되지 않습니다.

저작권법에 따른 이용자의 권리는 위의 내용에 의하여 영향을 받지 않습니다.

이것은 [이용허락규약\(Legal Code\)](#)을 이해하기 쉽게 요약한 것입니다.

[Disclaimer](#)

Doctoral Thesis

The Kinetics of Dissolution of Single Crystal Diamond
(100) and (110) in Nickel and Cobalt Films *and* Vapor-
Liquid-Solid Growth of Graphene Ribbons on Single
Crystal and Polycrystalline Cu Foils

Yunqing Li

Department of Materials Science and Engineering

Ulsan National Institute of Science and Technology

2022

The Kinetics of Dissolution of Single Crystal Diamond
(100) and (110) in Nickel and Cobalt Films *and* Vapor-
Liquid-Solid Growth of Graphene Ribbons on Single
Crystal and Polycrystalline Cu Foils

Yunqing Li

Department of Materials Science and Engineering

Ulsan National Institute of Science and Technology


The Kinetics of Dissolution of Single Crystal Diamond
(100) and (110) in Nickel and Cobalt Films *and* Vapor-
Liquid-Solid Growth of Graphene Ribbons on Single
Crystal and Polycrystalline Cu Foils

A thesis/dissertation submitted to
Ulsan National Institute of Science and Technology
in partial fulfillment of the
requirements for the degree of
Doctor of Philosophy

Yunqing Li

06.10.2022 of submission

Approved by

A handwritten signature in black ink, appearing to read 'Rodney Scott Ruoff', written over a horizontal line.

Advisor

Rodney Scott Ruoff

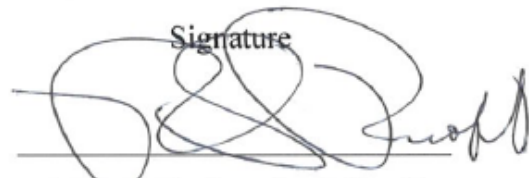
The Kinetics of Dissolution of Single Crystal Diamond
(100) and (110) in Nickel and Cobalt Films *and* Vapor-
Liquid-Solid Growth of Graphene Ribbons on Single
Crystal and Polycrystalline Cu Foils

Yunqing Li

This certifies that the thesis/dissertation of Yunqing Li is approved.

06.10.2022 of submission

Signature



Advisor: Rodney Scott Ruoff

Signature



Prof. Geunsik Lee

Signature



Prof. Tae Joo Shin

Signature



Prof. Hyung-Joon Shin

Signature



Prof. Zonghoon Lee

Abstract

The kinetics of dissolution of single crystal diamond (with surface orientation of 100 or 110, named as D(100) and D(110)) into nickel or cobalt films was measured, to the best of our knowledge, for the first time. This was possible through our discovery that at sufficiently high partial pressure of water vapor the rate determining step was breaking of C-C bonds at the diamond-metal interface; at lower partial pressures of water vapor, the rate determining step was found to be removal of carbon from the surface of the metal, rather than C-C bond breaking at the diamond-metal interface. The rate of diffusion from the diamond-metal interface to the surface of the metal film was found to never be rate-limiting. We found that single crystal diamond with surface orientation 111 could not be dissolved in either cobalt (Co) or nickel (Ni) films in the temperature range we studied. The details of this study are provided in Chapter 3. Time-of-flight-secondary ion mass spectrometry depth profiles show a concentration gradient of C from a certain depth into the metal film surface down to the M–D(100) interface, and residual gas analyzer measurements show that the gas products formed in the presence of water vapor by reaction of C atoms diffusing to, and thus present at, the metal surface are CO and H₂. As mentioned, we discovered two different regimes (we name them I and II) for the kinetics of dissolution of both D(100) and D(110), in which the rate-determining step was the removal of carbon atoms on the open metal surface (regime I, lower partial pressure of water vapor) or dissolution of diamond at the metal–diamond interface (regime II, higher partial pressure of water vapor) that yielded different Arrhenius parameters. We found that the rate of dissolution of diamond in Co was higher than that in Ni for both D(100) and D(110) and for both regimes I and II, and possible reasons are suggested. As mentioned, we also found that D(111) could not be dissolved at the Ni/D(111) and Co/D(111) interface in the presence of water vapor (over the same range of sample temperatures). The reaction paths for dissolution of C at the M–D(100) or M–D(110) interface and for removal of C from the free surfaces of Ni and Co were assessed through density functional theory modeling at 1273 K by colleagues Yongchul Kim and Prof. Geunsik Lee.

In Chapter 4, we describe the bottom-up direct growth of graphene ribbons catalyzed by deliberate introduction of silica particles onto a Cu(111) foil surface, and we ascribe their growth to a combination of vapor-liquid-solid (VLS) growth (longitudinal growth) and vapor-solid (VS) growth (lateral growth onto the already existing ribbon that extends longitudinally from the VLS growth). Micrometer-long single crystal graphene ribbons (tapered when grown above 900 °C, but uniform width when grown in the range 850 to 900 °C, as this latter temperature range is too low for VS growth) using silica particle seeds were synthesized on single crystal Cu(111) foil. We discovered that tapered and uniform-width

graphene ribbons grew strictly along the Cu<101> direction on Cu(111) and polycrystalline copper (Cu) foils. Silica particles on both the single crystal and polycrystalline Cu foils formed (semi-)molten Cu-Si-O droplets at growth temperatures, then catalyzed nucleation and drove the longitudinal growth of graphene ribbons. Longitudinal growth is likely by a vapor-liquid-solid (VLS) mechanism, but edge growth (above 900 °C) is due to catalytic activation of ethylene (C₂H₄) and attachment of C atoms or species (“vapor solid” or VS growth) at the edges. We found that the taper angle is determined only by the growth temperature and that the growth rates were independent of the particle size. A surface-diffusion vapor-liquid-solid growth model thus seems most appropriate for rationalizing the longitudinal growth. According to our kinetics study, we found the activation enthalpy (1.73 ± 0.03 eV) for longitudinal ribbon growth on Cu(111) from ethylene is lower than that for VS growth at the edges of the GRs ($2.78 \text{ eV} \pm 0.15 \text{ eV}$) and for the graphene island growth ($2.85 \pm 0.07 \text{ eV}$) that occurs concurrently. (That is, the Cu(111) surface has both GRs and hexagonal graphene islands. The graphene islands nucleate and grow on the regions of the Cu(111) surface where there is not a silica particle.

Contents

Abstract	i
List of Figures	vi
List of Tables	xiii
I. Background	1
1.1 Introduction of carbon materials.....	1
1.2 Dissolution of diamond in metal films.....	1
1.3 Synthesis of graphene ribbon.....	3
1.4 Vapor-liquid-solid (VLS) growth of ribbons.....	7
1.5 Kinetics study.....	10
References.....	12
II. Experimental techniques	14
2.1 Characterization techniques.....	14
2.1.1 Optical microscopy (OM).....	14
2.1.2 Scanning electron microscopy (SEM).....	14
2.1.3 Transmission electron microscopy (TEM).....	14
2.1.4 Atomic force microscopy (AFM).....	15
2.1.5 Raman spectroscopy.....	15
2.1.6 Time-of-flight secondary ion mass spectrometry (ToF-SIMS).....	16
2.1.7 Residual gas analyzer (RGA).....	16
2.1.8 X-ray diffraction (XRD) and <i>in situ</i> XRD.....	16
2.2 Experiment and sample preparation.....	17
2.2.1 Temperature calibration in quartz tube furnace and cold wall system.....	17
2.2.2 Diamond dissolution.....	18
2.2.3 Graphene ribbon growth.....	20
References.....	24

III. Kinetics of the Dissolution of diamond (100) and (110) Single Crystals in Nickel and Cobalt Films.....	25
3.1 Introduction.....	25
3.2 Results and discussion.....	25
3.2.1 Quartz tube furnace experiments.....	25
3.2.2 Cold wall system (RSR-M) experiments.....	47
3.2.3 XRD characterization.....	52
3.2.4 Theoretical modeling of reaction pathways and potential energy barriers.....	57
3.3 Conclusion.....	65
3.4 Experimental section.....	66
3.4.1 Materials and chemicals.....	66
3.4.2 Detailed methods.....	66
References.....	69
IV. Vapor-liquid-solid (VLS) growth of graphene ribbons on Cu foil and its kinetics study.....	72
4.1 Introduction.....	73
4.2 Results and discussion.....	73
4.2.1 Morphology and characterization of graphene ribbons.....	73
4.2.2 Growth behavior of graphene ribbons.....	81
4.2.3 Growth of graphene ribbon and its relationship with the Cu foil substrate.....	93
4.2.4 Kinetics analyses of graphene ribbon growth.....	95
4.3 Conclusion.....	105
4.4 Experimental section.....	106
4.4.1 Materials and chemicals.....	106
4.4.2 Detailed methods.....	106
References.....	108
Perspective.....	110
Acknowledgement.....	111

List of Figures

Figure 1.1 Metal-induced layer-exchange behaviors of several metals

Figure 1.2 SEM images of Ni/diamond (a) and Ni/HOPG (b) samples annealed at ~ 600 °C for 5 min in vacuum.

Figure 1.3 Anisotropic etch of single crystal (100) (a) and (110) (b) diamond plates in the presence of water vapor.

Figure 1.4 Schematic images of the sequence of steps to produce GNRs by electron-beam lithography.

Figure 1.5 Bottom-up synthesis of graphene ribbon by several methods: (a) particle cutting, (b) liquid synthesis and (c) unzipping of nanotubes.

Figure 1.6 Bottom-up organic synthesis of atomically precise GNRs.

Figure 1.7 Templated synthesis of graphene ribbon on (a) SiO₂/Si substrate, (b) SiC facet and (c) germanium substrate.

Figure 1.8 Vapor-liquid-solid growth of silicon nanowires.

Figure 1.9 Schematic images of possible nanowire structures grown at different conditions.

Figure 1.10 Vapor-liquid-solid growth of MoS₂ nanoribbons.

Figure 2.1 SEM images of (a) graphene FETs and (b) as-grown graphene ribbon.

Figure 2.2 TEM and cross-sectional TEM images of graphene.

Figure 2.3 Raman spectrum of different carbon materials.

Figure 2.4 (a) XRD spectra of single crystalline Cu foils with different high-index planes and (b) temperature-variable in situ XRD spectra of Ag-17 at. %Cu alloy films.

Figure 2.5 Water bubbler at different temperatures.

Figure 2.6 Schematic configuration of the water bubbler connected to the quartz tube furnace and the cold wall system chamber.

Figure 2.7 (a) The quartz tube furnace-water bubbler system and (b) the home-built RSR-M cold wall-water bubbler system. Note that the bubbler connected to the RSR-M system has the same configuration as that shown in (a).

Figure 2.8 (a) XRD and (b-d) EBSD characterizations of a Cu(111) foil produced through thermal annealing of polycrystalline Cu foil.

Figure 2.9 (a-c) HRTEM study of amorphous silica particles. The average particle size (from 50 particles) is 20 nm. (d) XRD of the silica particles. A single broad peak ($2\theta = 21.8^\circ$) is observed indicating that the silica particles used are amorphous.

Figure 3.1 EBSD characterization of (a) a 1 mm-thick single crystal diamond plate with a (100) surface, (b) a 0.3 mm-thick single crystal diamond plate with a (110) surface, and (c) a 1 mm-thick single crystal diamond plate with a (111) surface.

Figure 3.2 (a) Raman spectra after experiment without water vapor that were measured at the open metal surface (upper spectrum), and at the diamond surface after removal of the Ni film (lower spectrum). (b) Schematic of the Ni-diamond system; the green arrows show the diffusion direction of the C atoms. (c) SEM image of graphite film formed on the open Ni surface. (d) Raman spectra obtained after the experiment with water vapor present in the quartz chamber which were measured at the open metal surface (upper spectrum) and at the diamond surface after the removal of the Ni_xO_y/Ni film (lower spectrum). (e) Schematic of C diffusion through a Ni film and oxidation of C atoms at the open Ni surface. (f) SEM image of the nickel (oxide) surface.

Figure 3.3 SEM images of (a) wrinkled graphite film on the diamond surface; a Ni/D sample was heat treated at 1009±1 °C for 30 mins in Ar(g) (760±1 Torr) atmosphere with no water vapor present. (b) Bare diamond surface; a Ni/D sample was exposed to 1009±1 °C temperature for 30 mins, during which water vapor mixed with Ar(g) flowed through the reaction chamber (760±1 Torr pressure; no graphite/graphene was found).

Figure 3.4 (a-b) Arrhenius plots of the dissolution rates of single crystal diamonds with (100) surfaces coated with (a) a 500-nm thick Ni film and (b) a 500-nm thick Co film, at different water bubbler temperatures. (c-d) Arrhenius plots of the dissolution rates of single crystal diamond with (110) surfaces coated with (c) 500-nm thick Ni film, and (d) 500-nm thick Co film, at different water bubbler temperatures. (e) Real-time residual gas analyzer (RGA) analysis of water vapor-Ni-diamond reaction products. (f) Schematic of diamond dissolution with water vapor present: the surface reaction (regime I when this is rate limiting, step (iii)) and the metal diamond interface where diamond dissolves into the metal through breaking of C-C bonds at the M-D interface (regime II when this is rate limiting, step (i)). Step (ii) represents diffusion of C atoms through the Ni film—this is never rate limiting for our study.

Figure 3.5 Dissolution depth and mass loss *versus* time for D(110) coated with 500-nm thick Ni film at 963 °C with the water bubbler temperature of 43 °C.

Figure 3.6 Arrhenius plots of the dissolution rates based on mass loss or dissolution depth of single crystal diamonds with (110) surfaces coated with (a) 500-nm thick Ni film and (b) 500-nm thick Co film at different water bubbler temperatures.

Figure 3.7 3D microscopic images of D(110) samples coated with a 500-nm thick Ni film and treated at 963 °C (the bubbler temperature of 43 °C) for 30 mins, 60 mins, and 90 mins of the heat treatment.

Figure 3.8 (a) An optical microscope (OM) image of the entire dissolution region of a D(110) plate and (b) its schematic image showing two vertical D(111) side walls and two sloping D(111) side walls.

Figure 3.9 XRD patterns of Ni/Co films on (a-b) D(100), and (c-d) D(110) substrates. We note that there is no peak belonging to the Co film between 43 and 44 degrees and the background peaks in this range are due to the carbon paste we used to fix the sample for the variable temperature in-situ XRD measurements.

Figure 3.10 Schematic image of the combined CVD-RGA system.

Figure 3.11 Response of the residual gas analyzer (RGA) to the gases/vapors leaked from the reaction chamber into the RGA chamber. The reaction chamber conditions: 1050 °C furnace temperature, 43 °C bubbler temperature, 760±1 Torr pressure. At ~2200 s, Ar(g) was switched to flow through the water bubbler (water vapor started to flow into the reaction chamber).

Figure 3.12 Diamond dissolution depths (depths to which 500-nm thick Ni/Co films “sank” into the D(100) due to dissolution of diamond) as a function of time at different sample temperatures (the bubbler temperature was 25 °C). Dashed and solid lines correspond to 500-nm thick Co on D(100) and 500-nm thick Ni on D(100) samples, respectively.

Figure 3.13 Raman spectra measured at the open Ni surfaces of the 500-nm thick Ni/D(100) samples heat treated at 600 °C, 650 °C, and 700 °C.

Figure 3.14 (a-b) Spectropyrometer measurements of the emissivity of 500-nm thick Ni coated D(100) sample in the cold wall system and (c-d) time of flight-secondary ion mass spectrometry (ToF-SIMS) depth profiles measured for the Ni /D(100) sample with water vapor present for the conditions used in the continuous diamond dissolution experiments (c) and in the experiments with a fully oxidized metal layer (d).

Figure 3.15 An optical microscope (OM) image of a pierced D(100) plate obtained after the dissolution experiment (3 hours at 1050±1 °C, 770±5 Torr pressure, under continuous flow (1000 sccm Ar(g)) of water vapor (bubbler temperature, 25 °C).

Figure 3.16 Time of flight-secondary ion mass spectrometry (ToF-SIMS) depth profiles of a 500-nm thick Co/D(100) sample after heat treatment at 1000±1 °C for 10 mins with water vapor present in the reaction chamber.

Figure 3.17 Time of flight-secondary ion mass spectrometry (ToF-SIMS) depth profiles of (a) a 500-nm thick Ni/D(100) sample after heat treatment at 1000±1 °C for 10mins without water vapor in the reaction chamber; (b) a pristine 500-nm thick Ni/D(100) sample.

Figure 3.18 SEM images of the diamond surface taken (a) in the bare region (uncoated by Ni), (b) at the edge of the Ni-coated region, and (c) within the Ni-coated region after removing the NiO layer.

Figure 3.19 SEM images of (a) graphite film formed on the Pt surface after 1000±1 °C heat treatment for 3 hours (770±5 Torr) without water vapor present in the cold wall system reaction chamber; (b) Pt surface after exposure to a continuous flow of Ar(g) and 1000 sccm of water vapor (bubbler temperature, 25 °C) at 1000±1 °C. No graphite was observed.

Figure 3.20 Synchrotron-based GIXD patterns of (a) an as-deposited (pristine) Ni film on the D(100) surface, (b) Ni film after heating at 1009±1 °C for 1 h without water vapor and (c) Ni oxide/Ni film on the D(100) surface obtained after heating at 1009±1 °C for 10 min with water vapor (bubbler temperature 25 °C). (d) *In-situ* XRD study of a 500-nm thick Ni film on the D(100) surface. (e) Powder XRD (P-XRD) patterns of bare single crystal diamond with a (100) surface (upper curve) and nickel coated diamond heated at 1009±1 °C for 10 min with water vapor present (bubbler temperature 25 °C) contributing to the dissolution of diamond into the Ni film (lower curve).

Figure 3.21 Variable temperature *in-situ* XRD analyses of (a) 500-nm thick Co film on the D(100) surface, (b) 500-nm thick Ni film and (c) Co film on the D(110) surface. (d) P-XRD measurements of 500-nm thick Ni film on the D(111) surface. Note that the peak intensity is weak since the 1 mm x 1 mm area of the Ni film region on the D(111) surface is small.

Figure 3.22 P-XRD analysis of 500-nm thick Ni/Co film on (a-b) D(100) substrates and (c-d) D(110) substrates after dissolution experiments. We suggest that only fcc-Co exists (not hcp) in the Co/D(100) and Co/D(110) samples because the XRD pattern for Co/D(100) (b) is comparable to the fcc-Ni/D(100) XRD pattern (a), and the XRD pattern for Co/D(110) (d) is comparable to the fcc-Ni/D(110) XRD pattern (c), and also that the CoO peaks shown in (b), (d) are in agreement with the fcc-CoO phases but

not the hcp-CoO phases. In other words, and possibly due to the influence of the diamond substrates, the fcc-Co film does *not* convert to hcp after cooling to room temperature.

Figure 3.23 (a-b) Potential energy curves calculated for (a) a H₂O molecule reacting with Ni(100) (green) or Co(100) (blue), and (b) for C-C bond breaking at the Ni(100)/D(100) (green) or Co(100)/D(100) (blue) interfaces. The corresponding atomic structures of the initial, intermediate, and final configurations are shown as insets. (c-d) Potential energy curves calculated for a C atom diffusing from (c) the Ni(100)/D(100) interface (green) through the octahedral site (O*) or (d) the Co(110)/D(110) interface (blue) through the tetrahedral site (T*). The corresponding atomic structures of the initial, intermediate, and final configurations are shown as insets.

Figure 3.24 (left) Potential energy curves for a H₂O molecule reacting with the Ni(100) or Co(100) surfaces; (right) atomic structures of the initial physisorbed molecule ($x=0.0$), the transition state ($x=0.4$) and other intermediate configurations.

Figure 3.25 Potential energy curve for the surface reaction on Ni(100). (a) Potential energy curve for C atom migration from an octahedral (O*) site at the subsurface to an O* site at the surface, as shown in the inserted schematic image, which shows the reaction process from $x=0.0$ to 1.0 (1). The O atom migrates from the original O* site to the O* site that the C atom had occupied yielding formation of -Ni-C-O (2), followed by release of one CO into the atmosphere (3). (b) Potential energy curve for C atom migration from an O* site at the subsurface to an O* site at the surface, as shown in the inserted schematic diagram, which shows the reaction process from $x=0.0$ to 1.0 (1). The O atom migrates from the original O* site to an O* site that the C atom had occupied forming -Ni-C-O (2), followed by release of one CO into the atmosphere (3). Note that there are two possible paths for the migration of the O atom at the metal surface because there are two inequivalent half-octahedral sites that the C atom occupied relative to the position of the O atom at the surface. We calculated the two paths and provide the potential energy curve for both. The energy barriers at each step for these two paths are lower than the energy barrier of the surface reaction between a Ni atom and a H₂O molecule.

Figure 3.26 Potential energy curve for the surface reaction on Co(100). Potential energy curve for one C atom migration from an octahedral site (O*) at the subsurface to an O* site at the surface, as shown in the inserted schematic, which shows the reaction process from $x=0.0$ to 1.0 (1). The oxygen atom migrates from the original O* site to the O* site that the C atom had occupied and forms the -Co-C-O state (2), and the -Co-C-O state decomposes and releases a CO(g) molecule into the atmosphere (3). The path calculated is the same as that calculated in Figure 3.25a, which has a lower energy barrier in steps (1) and (2) compared with the energy barrier for steps (1) and (2) in Figure 3.25b. The energy barriers at each step for this path are lower than the energy barrier of the surface reaction between a Co atom and a H₂O molecule.

Figure 3.27 (left) Potential energy curves for a H₂O molecule reacting with the Ni(110) or Co(110) surface; (right) atomic structures of the initial physisorbed ($x=0.0$) state, the transition state ($x=0.4$) and other intermediate configurations.

Figure 3.28 Potential energy curve for the surface reaction on (a) Ni(110) and (b) Co(110). One C atom jumps from an octahedral (O*) site at the subsurface to a tetrahedral (T*) site, then to the surface, as shown in the inserted schematic; from $x=0.0$ to 1.0 (1), the O atom migrates from the original O* site to the T* site that the C atom occupied and forms -M-C-O (2), and the -M-C-O then releases a CO molecule into the atmosphere (3). Thus: From $x=0.0$ to 1.0 the indicated C atom moves to the surface, from $x=1.0$ to 2.0 a surface O atom and that same surface C atom migrate and react, and from $x=2.0$ to 3.0 CO desorbs. The appearance of a C atom on the M(110) surface thus occurs in two steps, as shown in the inserted schematic: from $x=0.0$ to 0.5, a C atom in the sublayer moves to a T* site just below the open surface, and from $x=0.5$ to 1.0, this C atom moves from the T* site to the open surface.

For Ni(110), this diffusion from subsurface to the surface has the highest energy barrier (161 kJ/mol) when the C atom migrates to the open surface. For Co(110) the highest energy barrier (165 kJ/mol) is for the C atom passing through the T* site.

Figure 3.29 (left) Potential energy curves for C atom diffusion at the Ni(100)/D(100) (green curve) and Co(100)/D(100) (blue curve) interfaces; (right) atomic structures of the initial ($x=0.0$), intermediate, and final ($x=1.0$) configurations.

Figure 3.30 (left) Potential energy curves for C atom diffusion at the Ni(110)/D(110) (green curve) and Co(110)/D(110) (blue curve) interfaces through the (a) *tetrahedral* and (b) *octahedral* interfacial sites; (right) atomic structures of the initial ($x=0.0$), intermediate ($x=0.2, 0.4, 0.6$, and 0.8), and final ($x=1.0$) configurations.

Figure 3.31 Potential energy curves of carbon diffusion barriers in fcc-Ni and fcc-Co. The C atom diffuses from an octahedral site to a tetrahedral site, then back to the octahedral site ($O^* \rightarrow T^* \rightarrow O^*$). We show the C atom diffusion energy barrier from the O^* site to T^* site only, due to symmetry.

Figure 4.1 (a) SEM images of a hexagonal graphene island and a graphene ribbon with a silica particle at its tip. (b) Raman maps of a GR showing G band intensity, I_D/I_G ratio, and FWHM of 2D band. (c) A $\sim 35\mu\text{m}$ -length monolayer GR grown on Cu(111) foil substrate. (d) SAED patterns at 4 different positions on the ribbon. (e) HRTEM atomic image of graphene lattice. (f) $I_{DS} \sim V_{GS} - V_{Dirac}$ transportation curve of one GR-FET, (inserts: OM and SEM images of GR-FETs, and curve showing the total resistance vs. back-gate voltage ($R_{tot} \sim V_{GS} - V_{Dirac}$) of the GR-FET). (g) Data on carrier mobility vs. intrinsic carrier density measured at 300 K.

Figure 4.2 (a) AFM height image of a graphene ribbon (GR) and the catalytic particle. (b) AFM amplitude error image of a particle contacted to a tapered GR.

Figure 4.3 (a-b) SEM images of (a) graphene islands and (b) graphene ribbons (GRs) on a bare Cu(111) foil or a Cu(111) foil coated with silica particles. This shows that that in the presence of the silica particles, graphene islands and GRs grow under the same CVD conditions and co-exist.

Figure 4.4 Temperature-time profile for the growth of graphene island/ribbon. In general, the growth conditions for monolayer graphene islands and GRs were found to be the same, and that without silica particles no ribbons were formed and only graphene islands were grown.

Figure 4.5 (a) Optical images (OM) of a hexagonal monolayer graphene island and a monolayer GR transferred on 300nm-SiO₂/Si wafer. (b) Raman spectra of graphene island and of GR (The selected positions are shown in a and labeled as 1, 2, 3). Raman spectra show low D band peak intensity for graphene island and GR.

Figure 4.6 TEM image of GR transferred onto a TEM grid.

Figure 4.7 (a) SEM image of a GR from a sample transferred onto a TEM grid. (b) SAED pattern of a GR. The TEM study found that the GR at the elongated region is single crystal without grain boundaries.

Figure 4.8 SEM images of GRs grown on a Cu(111) foil. To try to study the movement of particles during GR growth we obtained SEM images at different stages (cycle) of growth. As we used a quartz tube CVD system, some silica particles from the tube reactor were deposited on the Cu(111) foil substrate. (We note that this was in the initial stages of our work. We later were able to eliminate all contamination particles in our CVD-7 system in CMCM.) A first growth cycle was done as shown in a-b. We selected two particles: 1# and 2#. We then used a H₂ plasma cleaner (10 SCCM H₂, 120W, 10 mins) to remove the GRs from the Cu(111) foil and carried out the growth a second time using the same Cu foil under the same growth condition. (500 SCCM Ar, 250 SCCM H₂, 0.3 SCCM 1% C₂H₄/Ar, 30

min). We then examined the relative positions of the two particles on the Cu foil. We found that these same particles moved on the Cu(111) foil surface and the GRs grew along the direction of motion of the particle.

Figure 4.9 (a) SEM image of one particle at the tip of a GR. (b-d) EDS mapping of elemental (b) oxygen, (c) silicon and (d) copper. (e) EDS elemental analysis results of the particle. It is seen that the particles consist of silicon and oxygen, but the presence of copper cannot be ascertained since the analysis was carried out on a Cu substrate. The GR was therefore transferred onto a Au TEM grid for EDS analysis. The results are described in the main text.

Figure 4.10 (a) EDS elemental analysis of the particle attached to a GR transferred onto a gold (Au) TEM grid. (b) SEM images of GRs connected or not connected to particles. (c) SEM image and Raman map of the G band intensity of isotopic ^{13}C labelled GRs. (d) SEM image of a multilayer GR. (e) Schematic image showing particle mediated and VS growth behaviors.

Figure 4.11 (a) SEM image of a GR where the particle dissolved into the underlying Cu. (b) The C_2^- species map at the early sputter stage and its (c) 3D image show the position of the ribbon. (d) Si. species map at the middle sputter stage showing silicon element distribution, (e-f) 3D images of C_2^- and Si species distributions.

Figure 4.12 Since the particle was likely a molten/semi molten alloy at the growth temperature, the particles merged, which sometimes (a) stopped growth, or continued (b-c) to grow a GR.

Figure 4.13 (a) TEM and (b) SEM images of a particle connected to a GR were typically nearly-spherical; we note that not all of particles guiding the growth of GRs are “so spherical”. The morphology changes (compared to irregular shape of the as-received commercial silica particles) suggests that the particles were molten during growth of the GRs.

Figure 4.14 (a) SEM and (b) AFM images of a monolayer GR. (c) SEM and (d) AFM images of a multilayer GR. (c-d) show that the height of this multilayer GR at the center is higher than at the edge.

Figure 4.15 (a) High-magnification SEM image of a GR. The darkness contrast at the center region is shown. (b) SAED pattern of multilayer GR at the contrast region, indicating that the multilayer GR is a single crystal even though its thickness is not uniform. (c) Cross-sectional TEM image of the GR at the central region. We see that the central region is the thickest and the thickness gradually decreases along the normal to the growth direction. Also, we know that adlayers were grown on the top of the graphene layer, different from the conventional CVD growth of multilayer graphene (islands). (d) Schematic image of a multilayer GR showing the growth sequence of adlayers. Cross-sectional TEM images show that the thickness is maximum at the center of a multilayer GR gradually decreased on both sides normal to the ribbon direction. One possible reason for this is that the particle moved in the vicinity of the center during the growth. As the ribbon grows, carbon adatoms coming from the particle would have to migrate longer distances to attach to the graphene edges. We suggest they do not contribute to edge growth and that, also, the thickness of the adlayers is reduced along the direction normal to the long axis of the GR.

Figure 4.16 HRTEM images of the GR at the contrast region shown in the Figure 4.15b at (a) under-focused, (b) focused and (c) over- focused conditions. This proves that the darkness contrast of multilayer GR at the center is due to the layer number difference.

Figure 4.17 (a) SEM image of a multilayer GR with one particle connected to it. (b) The green line in the schematic shows the “contrast region” in the ribbon. (c) SEM image of multilayer GRs connected to two particles. The two particles were formed through the division of a single particle during the growth process. (d) Diagram of the “contrast region” in the ribbon, highlighted by the green line.

Figure 4.18 Raman map of the G band intensity of a ^{13}C -labelled monolayer GR. The intensity contrast reveals that the GR became wider, and also that particle mediated elongation continued after the ethylene gas was turned off and the $^{13}\text{CH}_4$ gas was then introduced.

Figure 4.19 (a) Symmetry of different Cu crystal planes. (b-e) SEM images and electron backscatter diffraction (EBSD) maps of GRs grown on (b) Cu(101), (c) Cu(-11-1), (d) Cu(010) and (e) Cu(1-13) planes. (f) High angle annular dark field (HAADF) image and SAED pattern of a GR. (g-h) Schematic images of graphene growth direction with respect to edge type.

Figure 4.20 (a-b) SEM images of GR growth, showing different start points of the particle. (c) HRTEM atomic image of a GR at the edge region and its SAED pattern. The growth direction of the GR (rose arrow marked in (c)) was strictly along the graphene zigzag direction, as shown in the SAED pattern. It should be noted that there is a small angle between the direction of the ribbon edge and the ribbon growth direction as the GR is needle shaped. The edge of the GR has atomic-scale kinks as shown in (c). This suggests that the needle-shaped ribbon width changes along the growth direction by the formation of atomic-scale kinks. In other words, the GR has zigzag edges with kinks present.

Figure 4.21 (a) Raman G band map of ^{13}C -labelled graphene ribbon grown at 925 °C. (b) The growth rates of *particle-mediated VLS* and *VS* at different growth temperatures. (c) Arrhenius plots for particle mediated growth and VS growth. (d) SEM images of GRs grown at different temperatures. (e) Statistical data of the angle distribution at different growth temperatures. (f) Angle distribution of GRs grown from silica particles of different sizes at 950°C. (g) Schematic image showing surface diffusion mechanism.

Figure 4.22 Raman G band maps of two different ^{13}C -labelled GRs grown at (a) 950 °C and (b) 900 °C, and then transferred on to 300nm-SiO₂/Si wafer.

Figure 4.23 (a-c) Raman G band maps of ^{13}C -labelled graphene islands transferred on 300nm-SiO₂/Si wafer grown at 950 °C, 925 °C and 900 °C, respectively. In the absence of silica particles, no GRs were grown. As shown in Figure S4b, graphene islands and GRs coexisted, during ^{13}C -labelled GR growth. Hence, we determined the growth rates of graphene islands and the average growth rates at the different temperatures were same as for the VS growth part of the ribbons. For graphene islands we extracted the activation enthalpy for growth, 2.71 ± 0.06 eV, which matches well with that obtained for the VS portion of growth of the GRs (2.71 ± 0.05 eV).

Figure 4.24 Morphology of GRs grown at different temperatures. At 850 °C, no graphene ribbons/islands were grown on the Cu foil. At 860 °C, the angle is close to 0°, showing that VS growth does not occur at this temperature. With only VLS growth, uniform width GRs grow under these conditions.

Figure 4.25 SEM image of GRs grown at 880 °C with 0.8 SCCM 1% C₂H₄ diluted in Ar, 500 SCCM Ar, and 250 SCCM H₂ for 1 hour. Note that a higher areal density of GRs is obtained.

Figure 4.26 TEM and EDS study of (a) pristine silica particle and (b) silica particle after trying to grow GRs at 850 °C. TEM and diffraction patterns suggest that the shape of the silica particle does not change at 850 °C. The composition of the particle (as determined from EDS element analysis) also shows no change. We note here that the Cu line in the spectrum has been artificially introduced *only to verify the presence of Cu if any* and therefore, the corresponding yellow line segments are deliberately introduced artifacts. The actual result suggests that the Cu signal should be at the level of background noise. In other words, the particle did not form any copper alloy(s) at 850 °C.

List of Tables

- Table 1.1** Maximum etch rates of diamond film by Fe, Ni, and Pt metal films in H₂ at 950 °C.
- Table 3.1** Water weight loss in the water bubbler at different bubbler temperatures. The values were obtained by averaging three values of water weight loss in the bubbler (each value was measured after 1 hour of Ar(g) flow through the bubbler during 3-hour experiments).
- Table 3.2** Calculated and experimental values obtained for the collisional flux Z_{surf} and the mole fraction at different bubbler temperatures.
- Table 3.3** Dissolution rates of D(100) coated with a 500-nm thick Ni/Co film. Each value is the average of three independent values. We used a 3D microscope to measure the depth of dissolved diamond after removing the Ni/Co film.
- Table 3.4** Dissolution rates of D(110) coated with 500-nm thick Ni/Co film. Each value is the average of four independent values. We used a 3D microscope to measure the depth of dissolved diamond after removing the Ni/Co film.
- Table 3.5** ΔH^\ddagger and pre-factor A values, from a study of the dissolution of D(100) and D(110) coated with a 500-nm thick Ni or Co film. Arrhenius equation: $\ln k = \frac{-\Delta H^\ddagger}{R} \left(\frac{1}{T}\right) + \ln A$, where k is the dissolution rate, ΔH^\ddagger is the activation enthalpy, A is the pre-exponential factor, R is the universal gas constant, T is the temperature of the sample (in Kelvin). Note that the activation enthalpies and the prefactors were calculated by measuring the depth of the dissolved section in the diamond plate after the experiment.
- Table 3.6** Mass loss dissolution rates of D(110) coated with 500-nm thick 2 x 2 mm Ni film.
- Table 3.7** Mass loss dissolution rates of D(110) coated with 500-nm thick 2 x 2 mm Co film.
- Table 3.8** ΔH^\ddagger and A' values of the dissolution of D(110) coated with 500-nm thick Ni film (2 mm x 2 mm) based on mass loss.
- Table 3.9** Ratios of experimentally measured diamond dissolution rates (Co vs. Ni) for D(100) and D(110) samples (i.e., the ratio of the dissolution rate of Co coated D($1k0$) to the dissolution rate of Ni coated D($1k0$), where k is equal to either 0 or 1). (The dissolution rates and thus their ratios were calculated based on the dissolution depth measurements).
- Table 3.10** Energy barrier values describing the formation of -Ni-C-O or -Co-C-O states on Ni/Co(100) and Ni/Co(110) surfaces and the decomposition to release CO into the gas phase.
- Table 3.11** The detailed parameters of the simulation model.
- Table 4.1** Carrier mobility and intrinsic carrier density of 15 GR-FETs at 300 K. (Two significant figures are shown for the average mobility values at the bottom of the table.)
- Table 4.2** Carrier mobility and intrinsic carrier density of 8 GR-FETs at 10 K. (Two significant figures are shown for the average mobility values at the bottom of the table.)
- Table 4.3** Data from 10 ¹³C-labelled growths of GRs at different growth temperatures. The fit values of the activation enthalpies using the Arrhenius equation for particle-mediated VLS and VS growth are 1.22 ± 0.19 eV and 2.71 ± 0.05 eV, respectively.

Table 4.4 Data for five separate ^{13}C -labelled growths of graphene islands at different growth temperatures.

Table 4.5 Graphene ribbon lengths for the 10 longest GRs that could be found in SEM images. It shows the length of each the 10 longest GRs at each of 3 different temperatures (900, 950, and 1000 °C), identified from SEM images by evaluating a 1 cm x 1 cm region of the Cu(111) foil that contained *many* GRs.

Table 4.6 Ribbon maximum width observed in a 1 cm x 1 cm region of Cu(111) foil. It shows the maximum width found for a GR among all GRs examined in SEM images, at each temperature: namely, 7# at 900 °C, 5# at 950 °C and 2# at 1000 °C, that are listed in Table 4.5 in bold text (the longest are also the widest, as expected). The activation enthalpy of the GR width growth was fit as 2.78 ± 0.15 eV.

Table 4.7 Graphene island with maximum diameter. It shows the maximum growth “diameter” (vertex-to-vertex across the hexagon) of the graphene islands at each temperature, from evaluating a 1 cm x 1 cm region with SEM imaging. The activation enthalpy of the graphene island growth is 2.85 ± 0.07 eV.

I Background

1.1 Introduction of carbon materials

Carbon has allotropes including diamond (sp^3 -carbon bonding throughout), graphite (sp^2 -carbon bonding throughout), and fullerenes and nanotubes (hybrid sp^3 - sp^2 carbon bonding throughout). Carbon appears in pseudo-1D and 2D materials as well as 3D structures, e.g., nanodot, nanoribbon, graphene, nanotube, fiber, glassy carbon, graphite, diamond, and so on. The wide range of bonding motifs (sp , sp^2 , sp^3 , hybrid) adopted by carbon lead to a very wide range of structures and this amplifies the range of applications for carbon.

Generally, carbon material has two types of carbon hybridized bond: sp^3 (diamond family) and sp^2 (graphite family). In terms of diamond family, it includes diamond, diamond-like carbon (DLC) and (F)-diamane.^{1,2} And as for graphite family, it includes graphite, graphene, and often the carbon-nanotubes (CNTs) and fullerenes (C_{60}) are incorrectly included as “ sp^2 ” when in fact their carbon-carbon bonding involves “re-hybridized” sp^2 - sp^3 orbitals such as has been presented by Haddon in a series of papers³⁻⁵), carbon fibers, turbostratic carbon and so on. Our focus here is on diamond, and graphene (as ribbons).

1.2 Dissolution of diamond in metal films

Metal-induced layer exchange of amorphous carbon and then formation of graphite/graphene were investigated on several metal films (**Figure 1.1**).⁶ Especially, multilayer graphene film on insulator

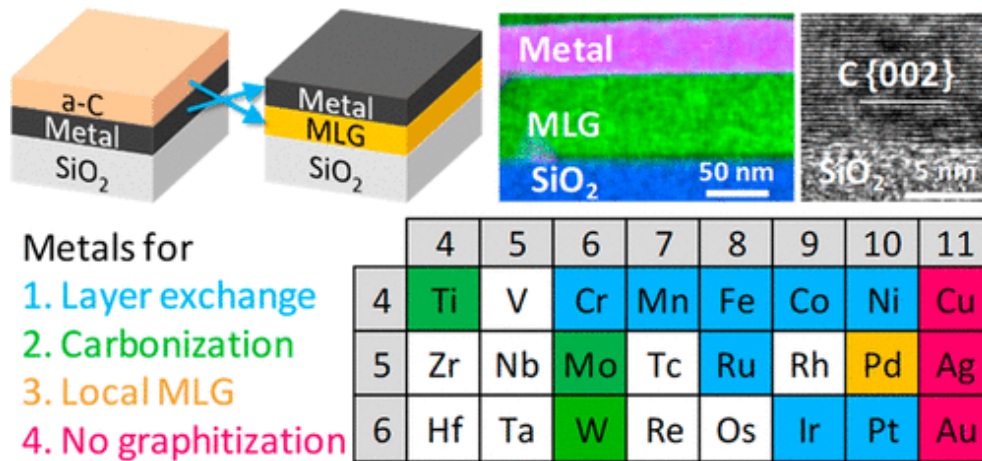


Figure 1.1 Metal-induced layer-exchange behaviors of several metals⁶.

Was reported to be formed by Ni and Co-induced layer exchange of amorphous carbon.^{7,8} This suggests Ni and Co films can induce formation of graphene/graphite due to their reasonably high carbon solubility and carbon diffusion rate at temperatures around 1000 °C. In contrast to amorphous carbon,

HOPG (highly oriented pyrolytic graphite) pieces were reported to not dissolve well in the Ni film below 1000 °C (**Figure 1.2**).⁹ In contrast, Diamond is reported to dissolve well in several metals above 600 °C.¹⁰⁻¹²

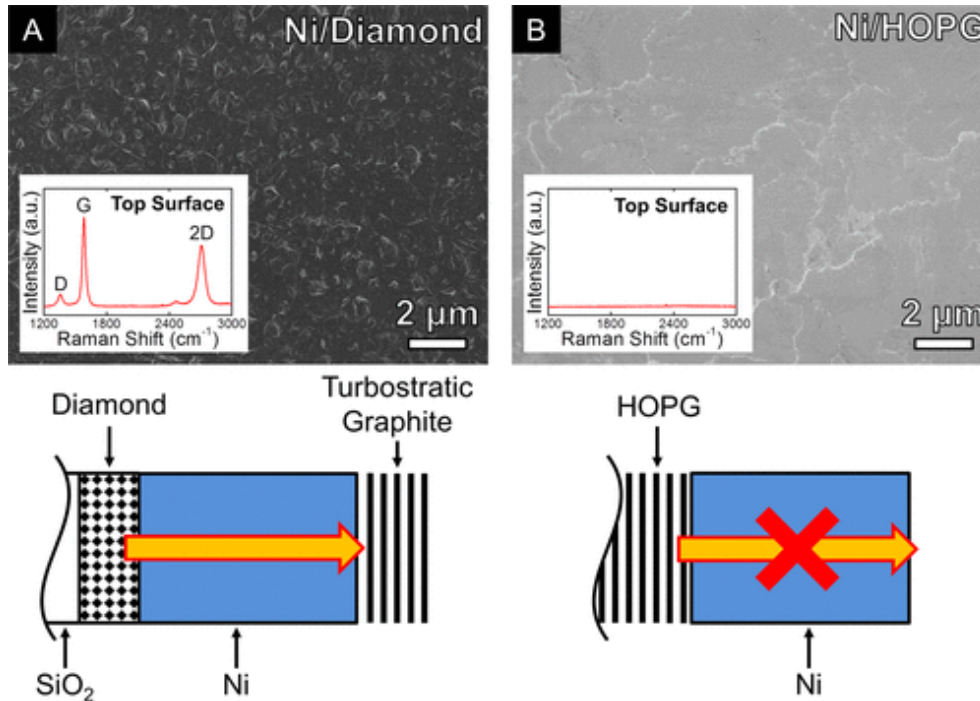


Figure 1.2 SEM images of Ni/diamond (a) and Ni/HOPG (b) samples annealed at ~600 °C for 5 min in vacuum. Sketches indicating the effect of annealing on each of the samples are also shown.⁹

When the metal open surface and metal/diamond interface form graphite, the further dissolution of diamond will not occur. To dissolve the diamond with no barrier to continuous dissolution, continuous removal of carbon from the metal film is necessary. The of dissolution of diamond coated with Fe, Ni and Pt films under hydrogen (H₂) atmosphere at temperature of 850-950 °C, in which the dissolved carbon atoms could continuously react with H₂ at the metal surface and be removed by the H₂ gas, has been reported¹³, as shown in **Table 1.1**.

Table 1.1 Maximum etch rates of diamond film by Fe, Ni, and Pt metal films in H₂ at 950 °C.¹³

Metal	Etch rate (μm min ⁻¹)	Metal thickness (μm)
Fe	8	0.1-1.0
Ni	0.27	0.2-11
Pt	0.005	0.2-11

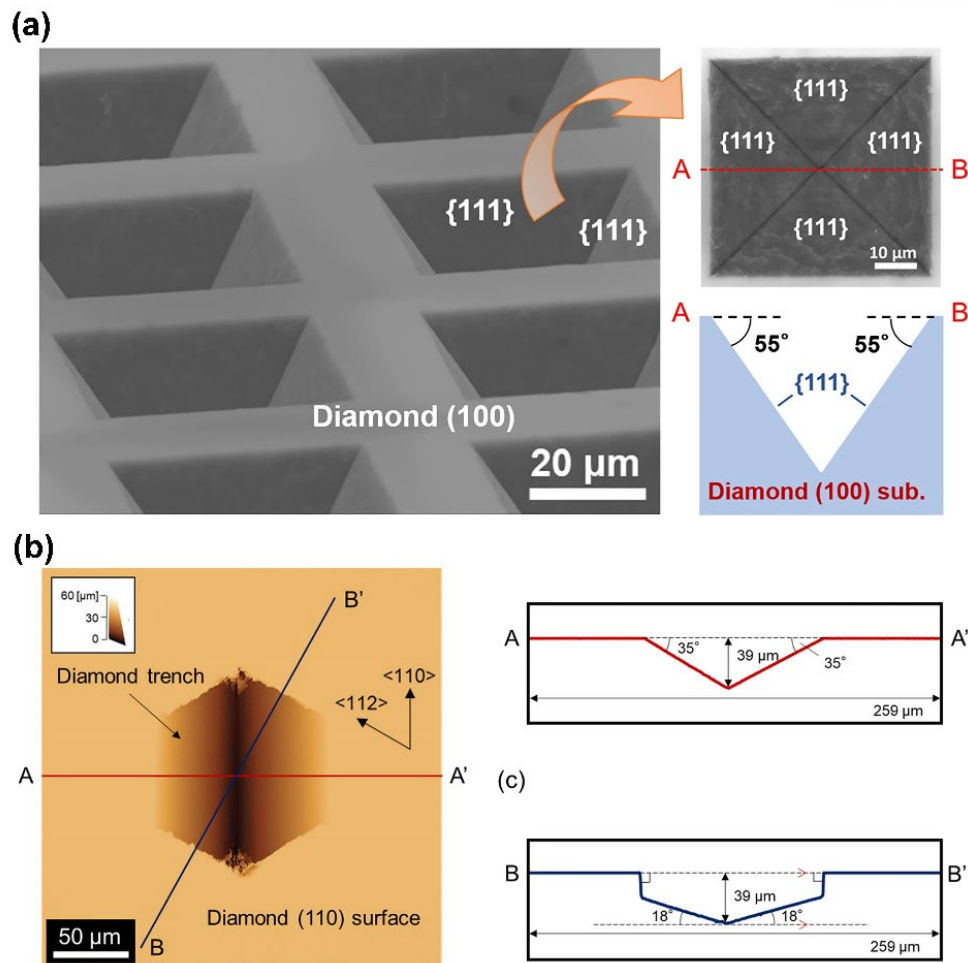


Figure 1.3 Anisotropic etch of single crystal (100) (a) and (110) (b) diamond plates in the presence of water vapor.^{11,12}

Recently, water vapor (rather than hydrogen gas) was used to drive the dissolution of diamond in Ni coated-single crystal diamond (100) and (110) plates,^{14,15} in which the dissolution depends on the crystal geometry, in other words, the dissolution was found to be anisotropic. Since the water vapor-induced dissolution of diamond when coated by certain metal films leads to the anisotropic “etching” of diamond it can be used to form certain types of diamond structures that might be useful for applications.

1.3 Synthesis of graphene ribbon

Graphene ribbon is a potential candidate for electronic devices due to its excellent mechanical, thermal, and electronic properties. The first reports of graphene ribbons involved photolithographic and electron-beam lithographic patterning of graphene film, following by reactive-ion etching (RIE)^{16,17} The schematic images are shown in **Figure 1.4**.

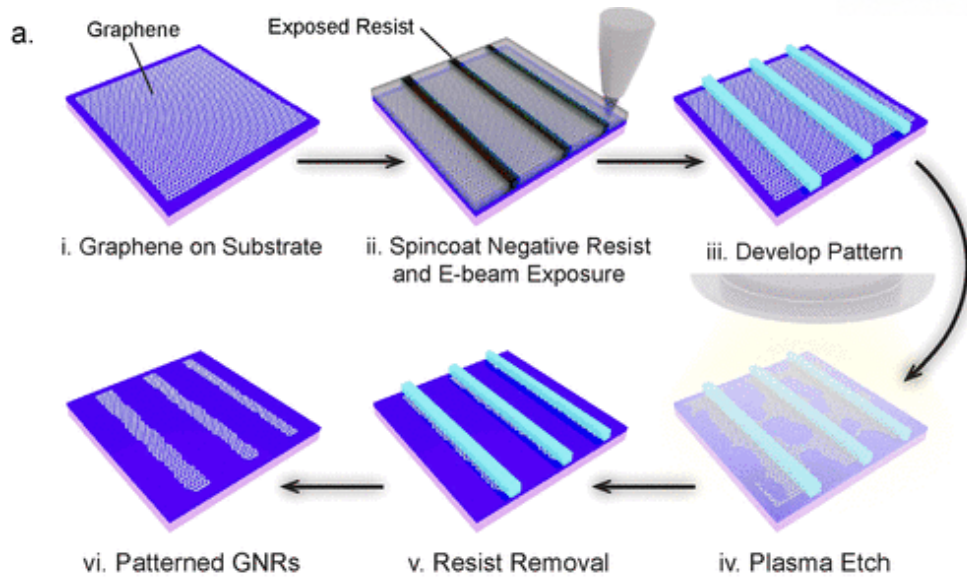


Figure 1.4 Schematic images of the sequence of steps to produce GNRs by electron-beam lithography.¹⁸

Such lithographic methods can produce graphene ribbons on several types of substrates, in which the output depends on the lithography used, being slower for electron-beam lithography. Due to the spatial resolution limit of electron-beam lithography, when making sub-5 nm-width graphene ribbons, the final product usually has disconnected parts.¹⁹ Other reported approaches have included (**Figure 1.5**¹⁸): (1) unzipping graphite by liquid phase methods;²⁰ (2) unzipping carbon nanotubes (CNTs) by solution or plasma methods;²¹ (3) directly “cutting” the graphene film using nanoparticles²².

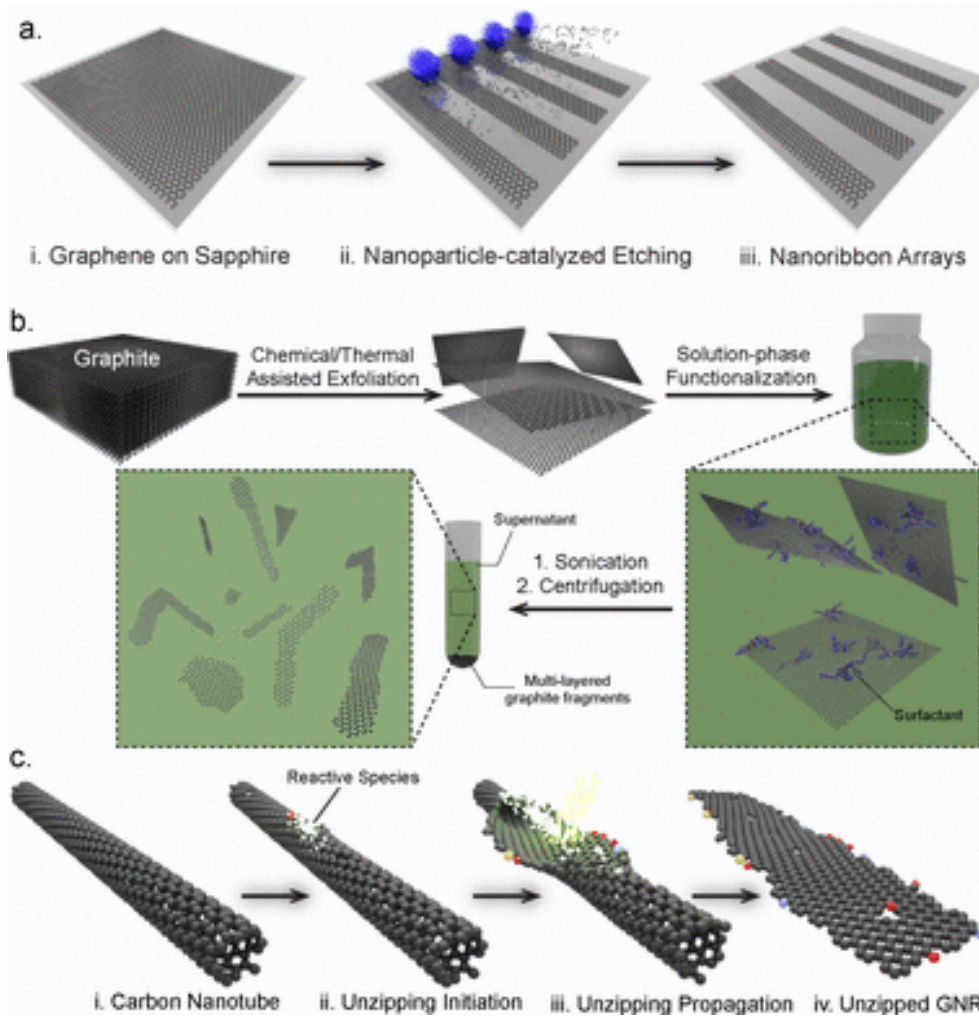


Figure 1.5 Bottom-up synthesis of graphene ribbon by several methods: (a) particle cutting, (b) liquid synthesis and (c) unzipping of nanotubes.¹⁸

However, these ‘bottom-up’ methods are primarily uncontrollable (for such parameters as graphene ribbon width, achieving smooth edges, alignment-control, substrate-transfer) but the reported yields are larger than as made by lithographic patterning. Chemical synthesis of graphene ribbons with uniform widths and smooth edges has been reported (**Figure 1.6**).²³ To date, such synthesized ribbons have not been long enough (they are <50 nm in length) to merge into high performance devices.²⁴ But this bottom-up synthesis with ‘perfect’ control of structure seems promising, because the desired physics can be “dialed in” through synthesis of desired ribbon structures.

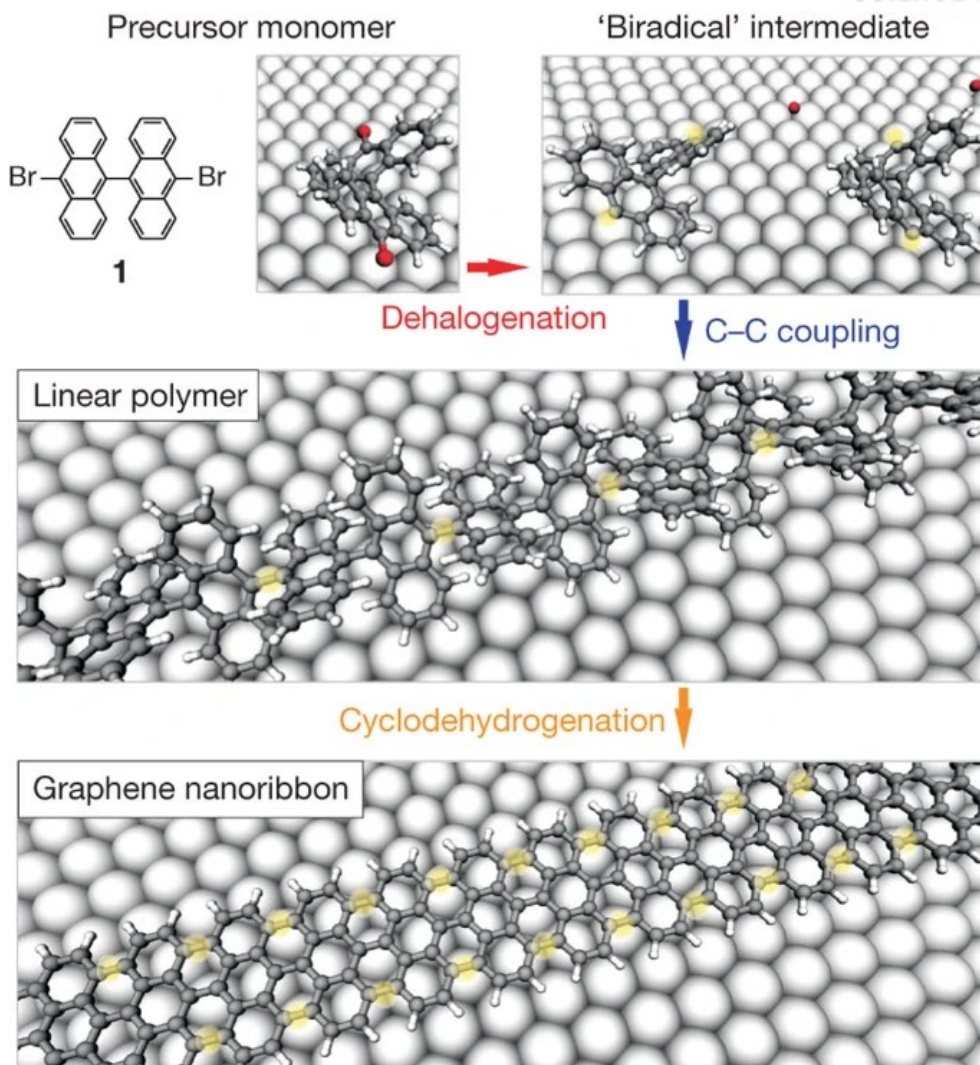


Figure 1.6 Bottom-up organic synthesis of atomically precise GNRs.²³

Templated synthesis methods have been reported (**Figure 1.7**): (i) Kato et al.²⁵ first used the nickel nanobars as the template and then directly grew graphene ribbon on SiO₂/Si substrate. They controlled the site and alignment of graphene ribbons, which were reported to exhibit good semiconducting performance. Metal residue on such graphene ribbons might mean that their integration into semiconductor manufacturing processes might be difficult.²⁶ (ii) Sprinkle, et al.²⁷ reported scalable templated growth of self-organized graphene ribbon on SiC nanofacets. (iii) Jacobberger, et al.²⁸ reported direct oriented growth of graphene ribbons on germanium; these (ii) and (iii) methods required high temperature and the reported growth rates are low. For graphene ribbon synthesis, a current challenge is straightforward synthesis of high yield, width- and alignment- controllable and “easy-to-handle” graphene ribbons with uniform edges.

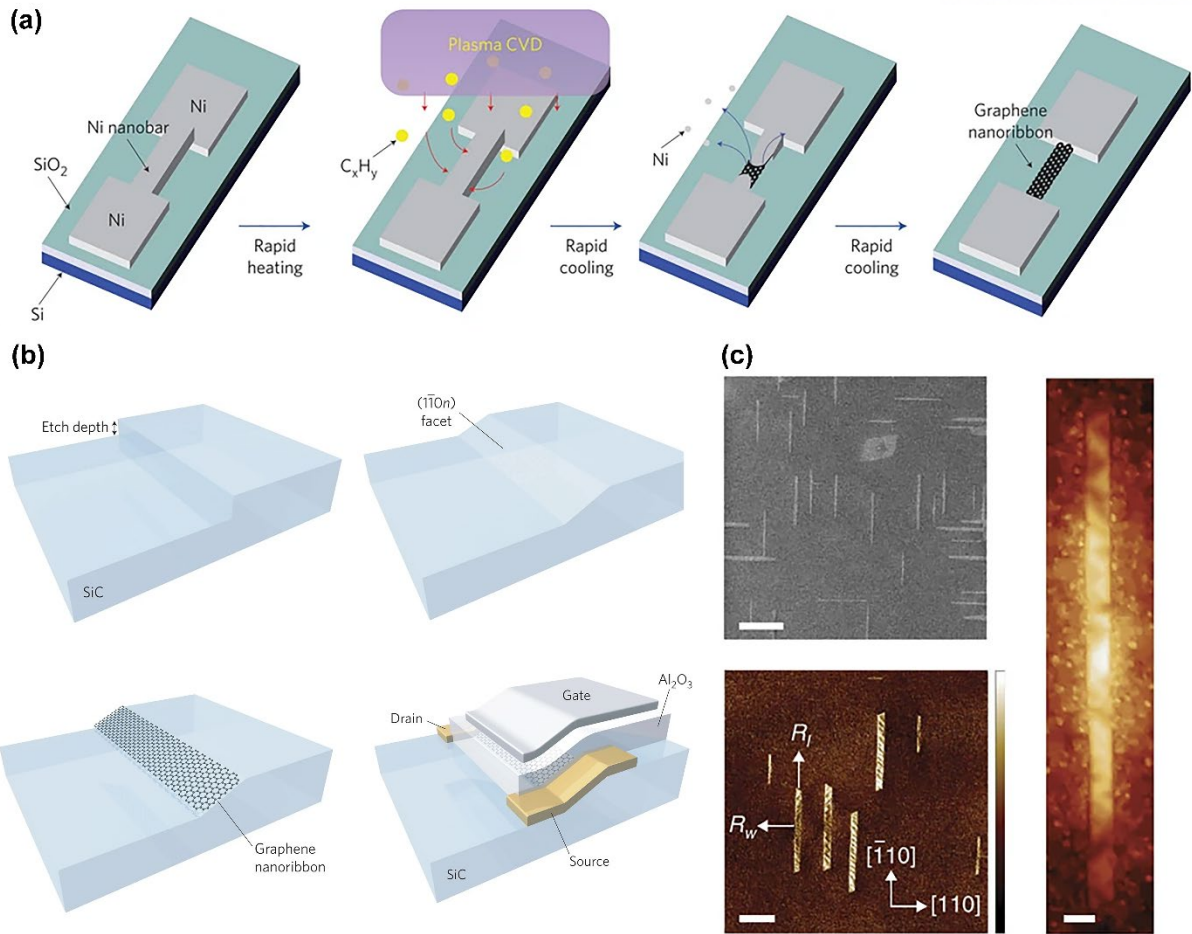


Figure 1.7 Templated synthesis of graphene ribbon on (a) SiO₂/Si substrate, (b) SiC facet and (c) germanium substrate.^{25,27,28}

1.4 Vapor-liquid-solid (VLS) growth

A wide range of one dimensional (1D) semiconductor nanowires catalyzed by a nanoparticle and thus VLS growth have been reported;^{29,30} the first study of VLS growth as reported by Wagner and Ellis was actually of relatively large-diameter “wires” of silicon from large Au particles that melted on Si substrates due to formation of the Au-Si eutectic (**Figure 1.8**).³¹

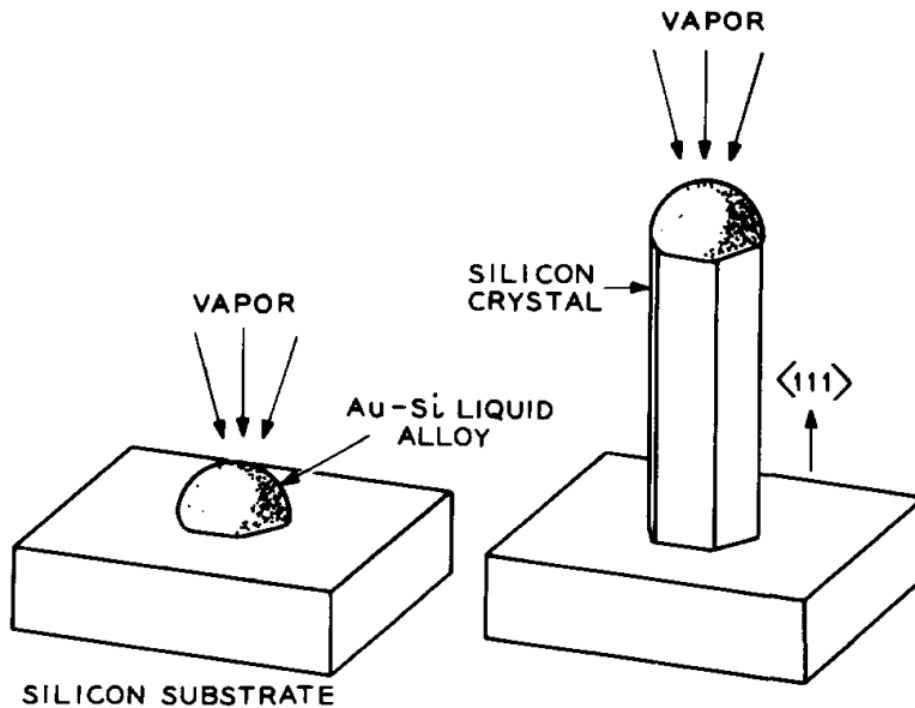


Figure 1.8 Vapor-liquid-solid growth of silicon nanowires.³¹

For nanowires, typically, gaseous precursors decompose on the surface of a nanoparticle and the active species diffuse either through the particle (“bulk” diffusion), or “around” the particle (surface diffusion), such that at the liquid-solid interface, a nanowire grows. If the catalyst particle is not molten at the growth temperature, the growth is typically referred to as vapor-solid-solid (VSS) growth. In VLS growth, selecting a suitable catalytic particle and controlling growth conditions can in some cases allow to vary the morphology of the nanoobjects including their size and shape (**Figure 1.9**).³²

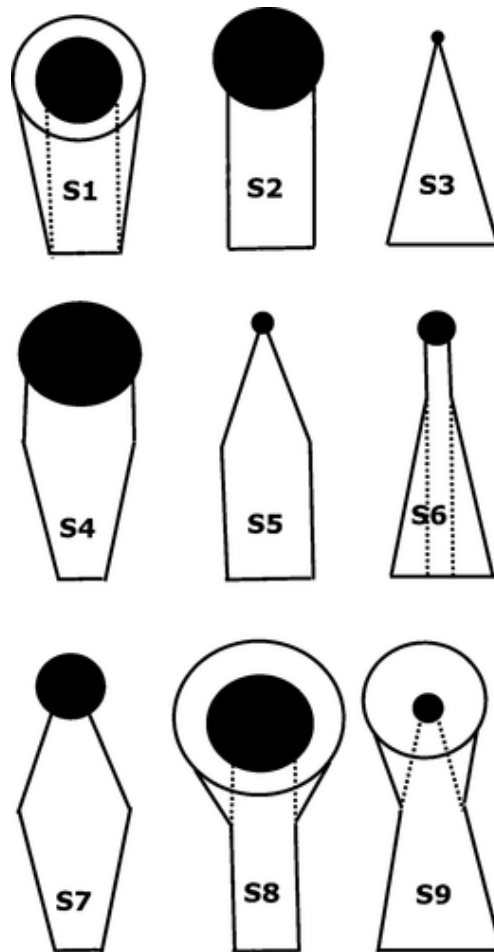


Figure 1.9 Schematic images of possible nanowire structures grown at different conditions.³²

The VLS growth of primarily uniform-width MoS₂ nanoribbons by forming Na–Mo–O droplets on NaCl and MoS₂ substrates at high temperature³³ and tapered MoS₂ nanoribbons grown on SiO₂/Si substrate by using Ni particles³⁴ have been reported, and other than the graphene ribbons described here, are the only 2D material ribbons to have been grown by VLS that we are currently aware of (**Figure 1.10**).

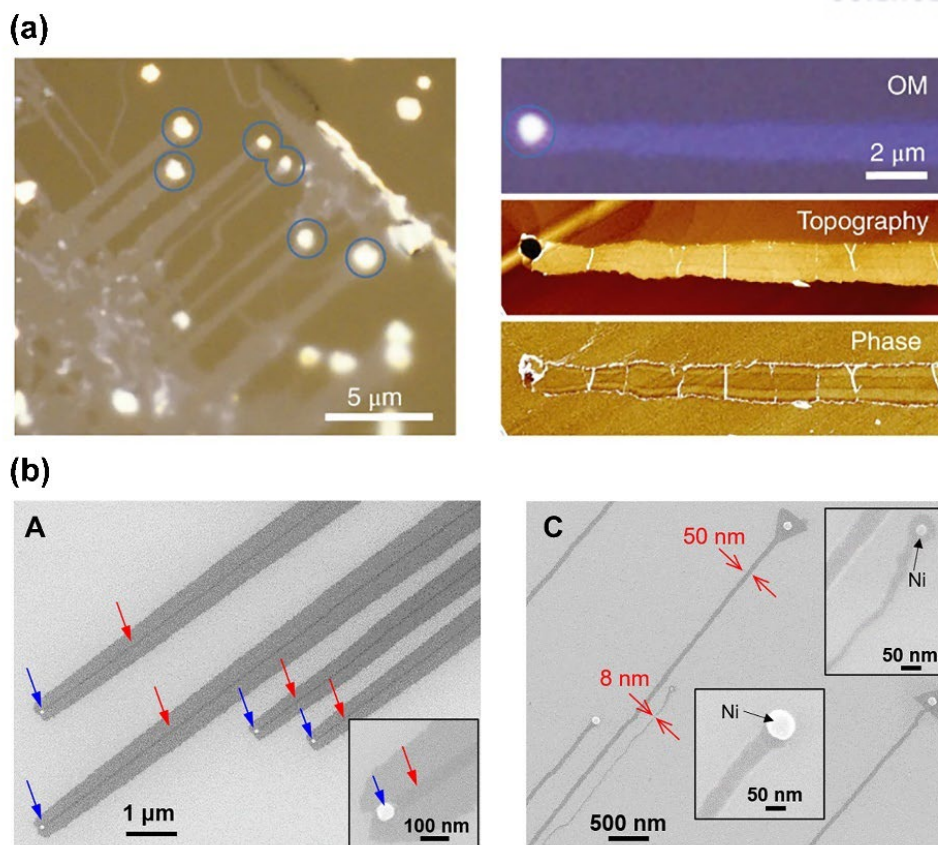


Figure 1.10 Vapor-liquid-solid growth of MoS₂ nanoribbons.^{33,34}

1.5 Kinetics study

The rates of chemical reactions is of fundamental interest. For example, in terms of temperature and based on the Arrhenius equation it is possible in some situations to learn about the activation energies/enthalpies of the chemical reactions and the pre-exponential factor (entropy term) and from these parameters to sometimes discern details about the rate limiting step at a given temperature and for certain reaction conditions. By comparing to theoretical calculations, it is possible to suggest a detailed (that is, with atomistic details) reaction pathway for the chemical reaction, in which some of the parameters of the potential energy surface can be compared to experimental values.

We studied the rate of dissolution of single crystal diamond (100) and (110) into Ni and Co films and describe this in detail in Chapter 3. We studied: the diamond dissolution rates at different temperatures, and thus the fit values for the activation enthalpies for the rate limiting step in several different kinetics regimes, and through modeling by our collaborators Yong Chul Kim and Professor Geunsik Lee, the detailed reaction pathway of C-C bond breaking at the metal-diamond interface and subsequent diffusion of the C atom into the Ni or Co.

Separately, we studied the rates of particle-mediated growth of graphene ribbons on Cu foil and describe this in detail in Chapter 4. We studied silica-particle mediated-VLS growth of graphene ribbons: the growth rates at different temperatures and thus obtained fit values to the activation enthalpy of longitudinal growth and of the activation enthalpy for lateral growth of such graphene ribbons.

References

- [1] Robertson, J., Diamond-like amorphous carbon. *Mat Sci Eng R* **2002**, 37 (4-6), 129-281.
- [2] Bakharev, P. V.; Huang, M.; Saxena, M.; Lee, S. W.; Joo, S. H.; Park, S. O.; Dong, J. C.; Camacho-Mojica, D. C.; Jin, S.; Kwon, Y.; Biswal, M.; Ding, F.; Kwak, S. K.; Lee, Z.; Ruoff, R. S., Chemically induced transformation of chemical vapour deposition grown bilayer graphene into fluorinated single-layer diamond. *Nat Nanotechnol* **2020**, 15 (1), 59-+.
- [3] Haddon, R. C., C60 sphere or polyhedron?," *J. Am Chem Soc* **1997**, 119, 1797–1798.
- [4] Haddon, R. C.; Scott, L. T., π -orbital conjugation and rehybridization in bridged annulenes and deformed molecules in general: π -orbital axis vector analysis. *Pure Appl Chem* **1986**, 58, 137–142.
- [5] Haddon, R. C., Hybridization and the orientation and alignment of π -orbitals in nonplanar conjugated organic molecules: π -orbital axis vector analysis (POAV2). *J Am Chem Soc* **1986**, 108, 2837–2842.
- [6] Nakajima, Y.; Murata, H.; Saitoh, N.; Yoshizawa, N.; Suemasu, T.; Toko, K., Metal Catalysts for Layer-Exchange Growth of Multilayer Graphene. *Acs Appl Mater Inter* **2018**, 10 (48), 41664-41669.
- [7] Murata, H.; Toko, K.; Suemasu, T., Multilayer graphene on insulator formed by Co-induced layer exchange. *Jpn J Appl Phys* **2017**, 56 (5).
- [8] Murata, H.; Saitoh, N.; Yoshizawa, N.; Suemasu, T.; Toko, K., High-quality multilayer graphene on an insulator formed by diffusion controlled Ni-induced layer exchange. *Appl Phys Lett* **2017**, 111 (24).
- [9] Weatherup, R. S.; Baetz, C.; Dlubak, B.; Bayer, B. C.; Kidambi, P. R.; Blume, R.; Schloegl, R.; Hofmann, S., Introducing Carbon Diffusion Barriers for Uniform, High-Quality Graphene Growth from Solid Sources. *Nano Lett* **2013**, 13 (10), 4624-4631.
- [10] Jin, S.; Graebner, J. E.; Kammlott, G. W.; Tiefel, T. H.; Kosinski, S. G.; Chen, L. H.; Fastnacht, R. A., Massive Thinning of Diamond Films by a Diffusion Process. *Appl Phys Lett* **1992**, 60 (16), 1948-1950.
- [11] Guan, Z. F.; Deng, F.; Liu, Q. Z.; Lau, S. S.; Hewett, C. A., Ni-diamond interactions. *Mater Chem Phys* **1996**, 46 (2-3), 230-232.
- [12] Thornton, A. G.; Wilks, J., Clean Surface-Reactions between Diamond and Steel. *Nature* **1978**, 274 (5673), 792-793.
- [13] Ralchenko, V. G.; Kononenko, T. V.; Pimenov, S. M.; Chernenko, N. V.; Loubnin, E. N.; Armejev, V. Y.; Zlobin, A. Y., Catalytic Interaction of Fe, Ni and Pt with Diamond Films - Patterning Applications. *Diam Relat Mater* **1993**, 2 (5-7), 904-909.
- [14] Nagai, M.; Nakanishi, K.; Takahashi, H.; Kato, H.; Makino, T.; Yamasaki, S.; Matsumoto, T.; Inokuma, T.; Tokuda, N., Anisotropic diamond etching through thermochemical reaction between Ni and diamond in high-temperature water vapour. *Sci Rep-Uk* **2018**, 8.
- [15] Nagai, M.; Nakamura, Y.; Yamada, T.; Tabakoya, T.; Matsumoto, T.; Inokuma, T.; Nebel, C. E.; Makino, T.; Yamasaki, S.; Tokuda, N., Formation of U-shaped diamond trenches with vertical {111} sidewalls by anisotropic etching of diamond (110) surfaces. *Diam Relat Mater* **2020**, 103.
- [16] Geng, Z. S.; Hahnlein, B.; Granzner, R.; Auge, M.; Lebedev, A. A.; Davydov, V. Y.; Kittler, M.; Pezoldt, J.; Schwierz, F., Graphene Nanoribbons for Electronic Devices. *Ann Phys-Berlin* **2017**, 529 (11).
- [17] Xu, W. T.; Lee, T. W., Recent progress in fabrication techniques of graphene nanoribbons. *Mater Horizons* **2016**, 3 (3), 186-207.
- [18] Saraswat, V.; Jacobberger, R. M.; Arnold, M. S., Materials Science Challenges to Graphene Nanoribbon Electronics. *Acs Nano* **2021**, 15 (3), 3674-3708.

- [19] Wang, X. R.; Dai, H. J., Etching and narrowing of graphene from the edges. *Nat Chem* **2010**, *2* (8), 661-665.
- [20] Li, X. L.; Wang, X. R.; Zhang, L.; Lee, S. W.; Dai, H. J., Chemically derived, ultrasmooth graphene nanoribbon semiconductors. *Science* **2008**, *319* (5867), 1229-1232.
- [21] Jiao, L. Y.; Zhang, L.; Wang, X. R.; Diankov, G.; Dai, H. J., Narrow graphene nanoribbons from carbon nanotubes. *Nature* **2009**, *458* (7240), 877-880.
- [22] Campos, L. C.; Manfrinato, V. R.; Sanchez-Yamagishi, J. D.; Kong, J.; Jarillo-Herrero, P., Anisotropic Etching and Nanoribbon Formation in Single-Layer Graphene. *Nano Lett* **2009**, *9* (7), 2600-2604.
- [23] Cai, J. M.; Ruffieux, P.; Jaafar, R.; Bieri, M.; Braun, T.; Blankenburg, S.; Muoth, M.; Seitsonen, A. P.; Saleh, M.; Feng, X. L.; Mullen, K.; Fasel, R., Atomically precise bottom-up fabrication of graphene nanoribbons. *Nature* **2010**, *466* (7305), 470-473.
- [24] Di Giovannantonio, M.; Deniz, O.; Urgel, J. I.; Widmer, R.; Dienel, T.; Stolz, S.; Sanchez-Sanchez, C.; Muntwiler, M.; Dumslaff, T.; Berger, R.; Narita, A.; Feng, X. L.; Mullen, K.; Ruffieux, P.; Fasel, R., On-Surface Growth Dynamics of Graphene Nanoribbons: The Role of Halogen Functionalization. *ACS Nano* **2018**, *12* (1), 74-81.
- [25] Kato, T.; Hatakeyama, R., Site- and alignment-controlled growth of graphene nanoribbons from nickel nanobars. *Nat Nanotechnol* **2012**, *7* (10), 651-656.
- [26] Lupina, G.; Kitzmann, J.; Costina, I.; Lukosius, M.; Wenger, C.; Wolff, A.; Vaziri, S.; Ostling, M.; Pasternak, I.; Krajewska, A.; Strupinski, W.; Kataria, S.; Gahoi, A.; Lemme, M. C.; Ruhl, G.; Zoth, G.; Luxenhofer, O.; Mehr, W., Residual Metallic Contamination of Transferred Chemical Vapor Deposited Graphene. *ACS Nano* **2015**, *9* (5), 4776-4785.
- [27] Sprinkle, M.; Ruan, M.; Hu, Y.; Hankinson, J.; Rubio-Roy, M.; Zhang, B.; Wu, X.; Berger, C.; de Heer, W. A., Scalable templated growth of graphene nanoribbons on SiC. *Nat Nanotechnol* **2010**, *5* (10), 727-731.
- [28] Jacobberger, R. M.; Kiraly, B.; Fortin-Deschenes, M.; Levesque, P. L.; McElhinny, K. M.; Brady, G. J.; Delgado, R. R.; Roy, S. S.; Mannix, A.; Lagally, M. G.; Evans, P. G.; Desjardins, P.; Martel, R.; Hersam, M. C.; Guisinger, N. P.; Arnold, M. S., Direct oriented growth of armchair graphene nanoribbons on germanium. *Nat Commun* **2015**, *6*.
- [29] Chen, C. C.; Yeh, C. C.; Chen, C. H.; Yu, M. Y.; Liu, H. L.; Wu, J. J.; Chen, K. H.; Chen, L. C.; Peng, J. Y.; Chen, Y. F., Catalytic growth and characterization of gallium nitride nanowires. *J Am Chem Soc* **2001**, *123* (12), 2791-2798.
- [30] Tsivion, D.; Schwartzman, M.; Popovitz-Biro, R.; von Huth, P.; Joselevich, E., Guided Growth of Millimeter-Long Horizontal Nanowires with Controlled Orientations. *Science* **2011**, *333* (6045), 1003-1007.
- [31] Wagner, R. S.; Ellis, W. C., Vapor-Liquid-Solid Mechanism of Single Crystal Growth (New Method Growth Catalysis from Impurity Whisker Epitaxial + Large Crystals Si E). *Appl Phys Lett* **1964**, *4* (5), 89-&.
- [32] Mohammad, S. N., Analysis of the vapor-liquid-solid mechanism for nanowire growth and a model for this mechanism. *Nano Lett* **2008**, *8* (5), 1532-1538.
- [33] Li, S. S.; Lin, Y. C.; Zhao, W.; Wu, J.; Wang, Z.; Hu, Z. H.; Shen, Y. D.; Tang, D. M.; Wang, J. Y.; Zhang, Q.; Zhu, H.; Chu, L. Q.; Zhao, W. J.; Liu, C.; Sun, Z. P.; Taniguchi, T.; Osada, M.; Chen, W.; Xu, Q. H.; Wee, A. T. S.; Suenaga, K.; Ding, F.; Eda, G., Vapour-liquid-solid growth of monolayer MoS₂ nanoribbons. *Nat Mater* **2018**, *17* (6), 535-+.
- [34] X. F. Li, B. C. Li, J. C. Lei, K. V. Bets, X. H. Sang, E. Okogbue, Y. Liu, R. R. Unocic, B. I. Yakobson, J. Hone, A. R. Harutyunyan, *Sci. Adv.* **2021**, *7*, 1.

II Experimental techniques

2.1 Characterization techniques

2.1.1 Optical microscopy (OM)

Optical microscopy is a basic technique to check sample morphology and structure. In this work, we used OM (ZEISS AxioScope 5) to check the morphology and structure of diamond samples after experiments, the morphology of graphene ribbon transferred on SiO₂/Si substrate, and the graphene ribbon field-effect transistors (GR-FETs).

2.1.2 Scanning electron microscopy (SEM)

Scanning electron microscopy was used in our work to check the micro-morphology/structure of samples^{1,2}. We used SEM (FEI Verios 460) to check the formation of graphite/graphene on the diamond after experiments, graphene ribbons on Cu foils and GR-FETs. EDS plugin (Octane Elect EDS System) in the SEM was used to check the composition of particles and EBSD plugin (Hikari from Ametek) in the SEM was used to check the crystallographic orientations of the Cu foils.

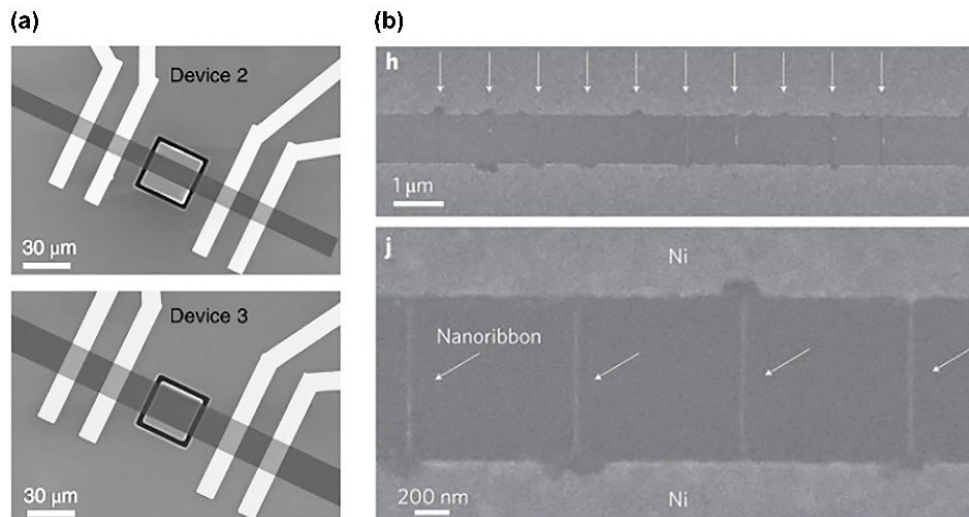


Figure 2.1 SEM images of (a) graphene FETs and (b) as-grown graphene ribbon.^{1,2}

2.1.3 Transmission electron microscopy (TEM)

Transmission electron microscopy is used, among other things, to obtain structure information at the atomic scale.^{3,4} One can learn about atomic defects in the material, the atom-to-atom bonding, stacking of atomic layers, and other useful information. In this work, we used HRTEM (HR-TEM, FEI Titan3 G2 60-300) and obtained high-resolution atomic scale images of monolayer graphene such as to check whether the graphene ribbon is single crystal or not and to study the edge structure of graphene ribbons. Based on focus-ion-beam (FIB) sample preparation cross-sectional high resolution atomic images of

multilayer graphene ribbons were obtained. We used the EDX plugin in the HRTEM to measure the composition of particles connected to the graphene ribbons that had been transferred onto a Au TEM grid.

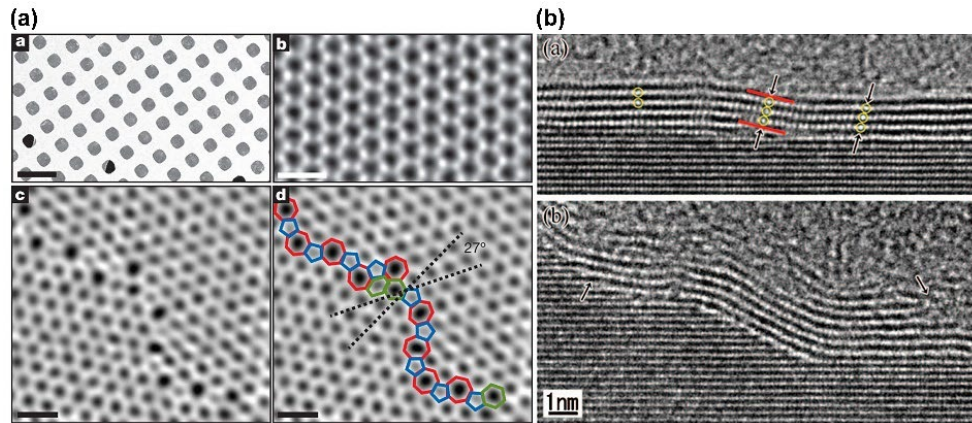


Figure 2.2 TEM and cross-sectional TEM images of graphene.^{3,4}

2.1.4 Atomic force microscopy (AFM)

Atomic force microscopy is a surface characterization tool that can be used to measure the thickness of materials and also the thickness uniformity of thin films. We used AFM (Bruker Dimension Icon) to study the morphology of graphene ribbons on Cu foils.

2.1.5 Raman spectroscopy (Raman)

Raman spectroscopy is particularly useful for characterization of carbon materials. As shown in **Figure 2.3**,⁵ diamond has a characteristic peak at around 1330 cm^{-1} , and graphene at around 1580 cm^{-1} . The D band intensity can inform about defects and the ‘quality’ of graphene, and the ratio of G band versus 2D band intensity (I_G/I_{2D}) can be used to determine the number of stacked layers of multilayer graphene, while the shape of the 2D band can help one understand the stacking order of multilayer graphene.⁶ Raman spectroscopy can be used to ascertain the presence of metal oxide at the surface.^{7,8} We used Raman spectroscopy (WITec, 532 nm wavelength laser) in our studies of graphene ribbons and to evaluate the possible formation of graphite, and metal oxide on the metal film, in our studies of the dissolution of diamond into metal films.

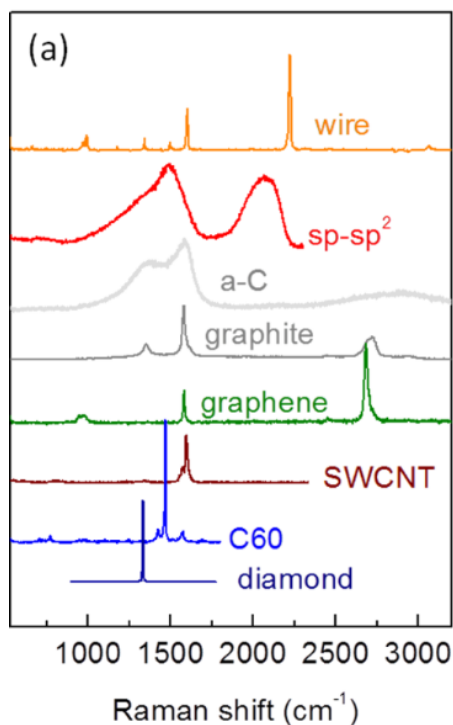


Figure 2.3 Raman spectrum of different carbon materials.⁵

2.1.6 Time-of-flight secondary ion mass spectrometry (ToF-SIMS)

Time-of-flight secondary ion mass spectrometry is a surface-sensitive analytical method. It uses a pulsed ion beam to remove molecules/atomic species from the sample surface. We used ToF-SIMS (ION-TOF GmbH TOF.SIMS 5) to check the depth profile of element distribution in the Ni and Co films on diamond, and the silicon element depth profile in the Cu foils that graphene ribbons were grown on.

2.1.7 Residual gas analyzer (RGA)

A Residual Gas Analyzer is a mass spectrometer that can be used to analyze gas molecules up to molecular weight (for our system) of 200 amu, and at gas pressures even up to 1 atm. We used an SRS-RGA-300 to analyze the gas products appearing in the *isothermal quartz tube CVD system* during the dissolution of diamond in the presence of water vapor.

2.1.8 X-ray diffraction (XRD) and *in situ* XRD

We used Powder XRD (Rigaku SmartLab) to analyze the crystalline structure of the Ni and Co films on the single crystal diamond samples, and of the Cu foil used in our graphene ribbon studies. We also used *in situ* XRD (Panalytical/Empyrean ALPHA-1) to analyze the Ni and Co film during a programmed heat treatment process. A typical XRD measurement result is shown in **Figure 2.4**.

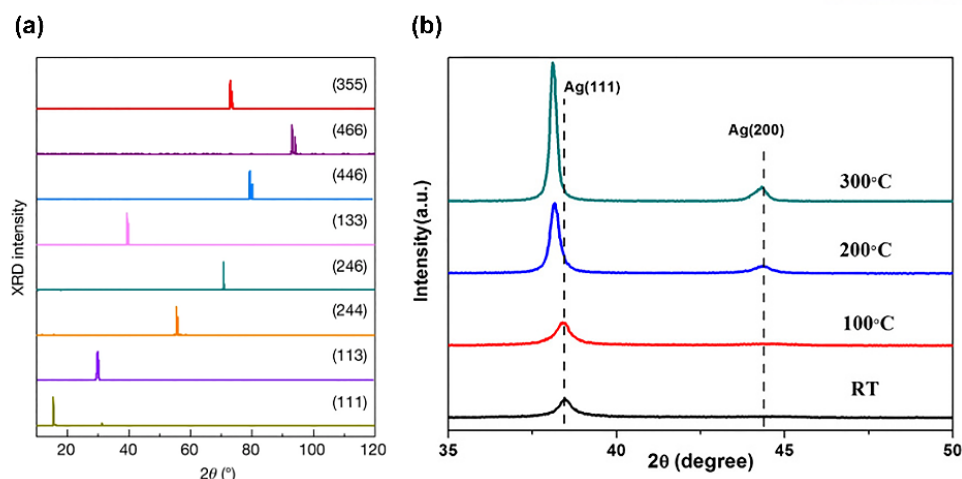


Figure 2.4 (a) XRD spectra of single crystalline Cu foils with different high-index planes and (b) temperature-variable in situ XRD spectra of Ag–17 at. %Cu alloy films.^{9,10}

2.2 Experiment and sample preparation

2.2.1 Temperature calibration in quartz tube furnace and cold wall system

Isothermal quartz tube furnace: To measure the actual temperature of the sample, a thermocouple attached to the quartz sample holder was used to read all of the temperature points we used in our study. That is, the temperature reported by the tube furnace is not the actual temperature at the position of the sample inside the quartz tube. This is because the “furnace temperature” is the temperature at the position of a thermocouple that is mounted adjacent to the outside of the quartz tube, and that is embedded in the insulation surrounding the quartz tube. For this reason, we inserted a thermocouple that was very close to the diamond sample.

RSR-M cold wall system: The diamond samples were placed in a tungsten(W) crucible that was resistively (that is “Joule”) heated. To calibrate the sample temperature measured by a pyrometer, we used 99.98% purity copper(Cu) foil (Goodfellow, 50 μm thick). A small piece of Cu foil was put in a W crucible and heated to its melting temperature under 770 ± 1 Torr pressure. The standard melting temperature of Cu (~ 1085 $^{\circ}\text{C}$, 760 Torr) was used to calibrate our temperature measurements—by so calibrating the pyrometer.

Water bubbler configuration and temperature: A hot plate or ice water was used to maintain a constant water bath temperature during the entire run of water vapor induced dissolution of diamond. The bubbler was filled with deionized water, and 1000 sccm Ar(g) flowed through it for a long period (typically 5 hours) with the goal of removing any dissolved gas including oxygen. A glass beaker was filled with sufficient water and the water bubbler was submerged in it. A thermometer in the water did

not touch the beaker wall. An ice water bath provided a constant 0 °C, and ice was added as needed. A thermocouple in the bath measured the temperature, including when the hot plate was used rather than ice water. We unscrewed the water bubbler and immediately inserted a thermometer into the bubbler for 5 mins to check the water temperature in it without removing the glass container. No temperature difference between the water in the glass beaker and the water in the bubbler was found. **Figure 2.5** is a photo of the bubbler in the bath attached to the quartz tube furnace at different bubbler temperatures. The configuration of the water bubbler attached to the cold wall system is identical.

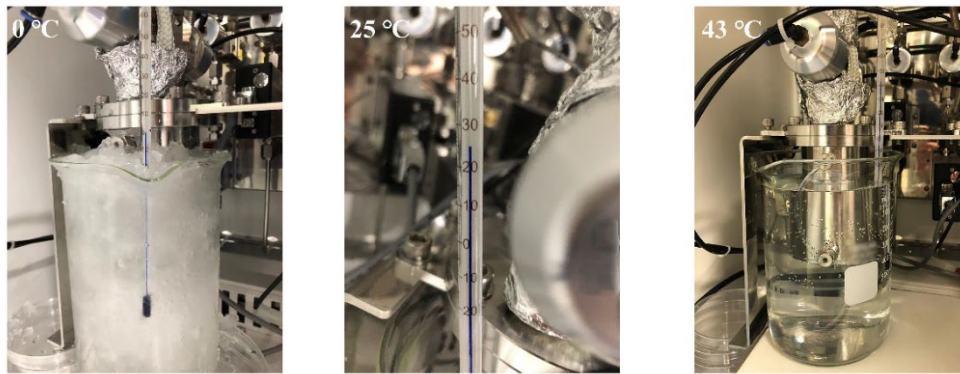


Figure 2.5 Water bubbler at different temperatures.

2.2.2 Diamond dissolution

0.3 mm and 1 mm-thick 3x3 mm HPHT IIa-type single crystal diamond plates with (100), (110) and (111) surface planes were used. First, the diamond plates were cleaned with acetone in an ultrasonic bath for 30 mins to remove organic impurities, then the samples were immersed for 15 mins in a hydrogen peroxide (H₂O₂)/ sulfuric acid (H₂SO₄) solution (2:1 by volume) at 120 °C¹¹ to remove any surface contaminants. Ni or Co films (2 mm x 2 mm square) were then deposited onto the diamond plates through the 304 steel metal masks by DC sputtering (SRN120, SORONA). 500-nm thick Nickel (Ni) or Cobalt (Co) films were sputtered onto a 0.3 mm thick, 3 mm x 3 mm single crystal diamond D(100) and D(110) plates (note that some 3 x 3 mm D(100) samples we used were 1 mm thick and there is no difference in them except for the thickness) or onto a 1 mm thick, 1.5 x 1.5 mm single crystal diamond D(111) substrates. The thickness of the Ni or Co films was measured by a surface profiler.

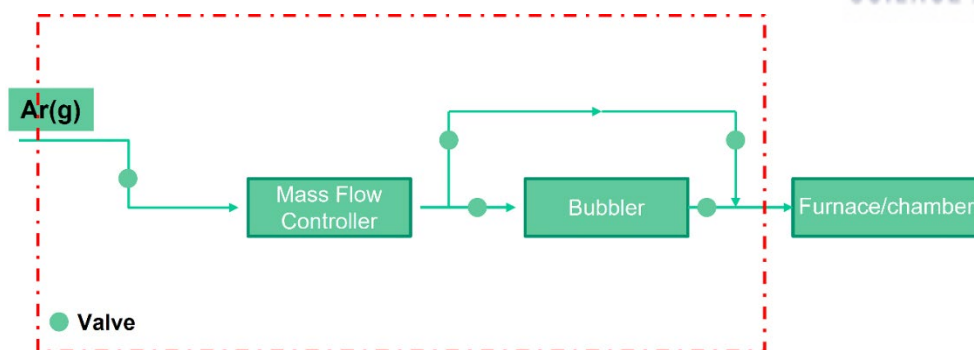


Figure 2.6 Schematic configuration of the water bubbler connected to the quartz tube furnace and the cold wall system chamber.

A schematic image of system configuration was shown in **Figure 2.6**. In detail, a 2-inch diameter quartz tube CVD furnace equipped with a water bubbler placed upstream was used and a gas switcher was used to control the supply of water vapor (**Figure 2.7a**). A rapid joule-heating system with an 8 cm-diameter quartz window on top of its stainless-steel water-jacket was used for experiments involving rapid heating and cooling to enable visual observation and video recording of the sample during heating and cooling (**Figure 2.7b**); The system was also equipped with a water bubbler held in a constant temperature water bath. The working pressure in both systems was set by a pressure controller (MKS, 600 Series). After any experiments involving heat treatment with or without exposure to water vapor, the samples were either directly used for further study, or put into an acid solution (5 mL 30% hydrogen peroxide (H_2O_2), 10 mL 37% hydrochloric acid (HCl) and 100ml deionized(DI) water) to remove the metal films.

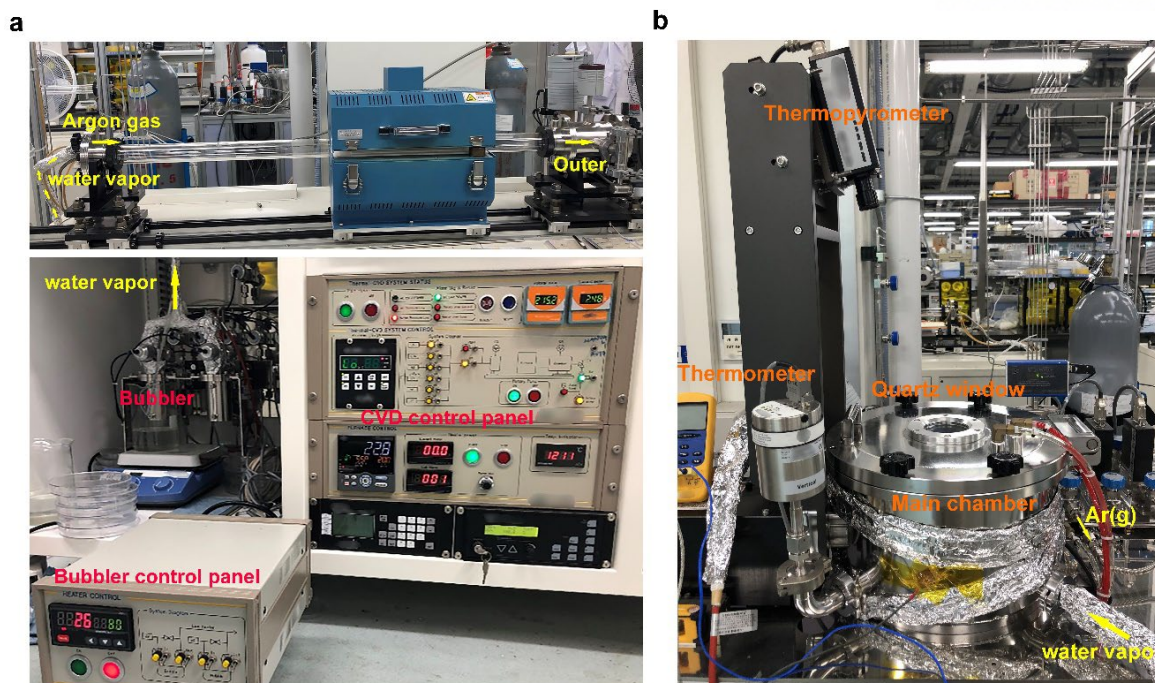


Figure 2.7 (a) The quartz tube furnace-water bubbler system and (b) the home-built RSR-M cold wall-water bubbler system. Note that the bubbler connected to the RSR-M system has the same configuration as that shown in (a).

2.2.3 Graphene ribbon growth

Large area Cu(111) foil was prepared by thermal annealing of a 7 x 7 cm, 50 μm -thick polycrystalline Cu foil under Ar and H_2 mixed gas at atmospheric pressure at 1060 $^\circ\text{C}$ for 18 h using the “contact-free annealing” (CFA) method.¹² The crystallographic orientation of the as-prepared Cu(111) foil was determined from X-ray diffraction (XRD) and EBSD as shown in **Figure 2.8**.

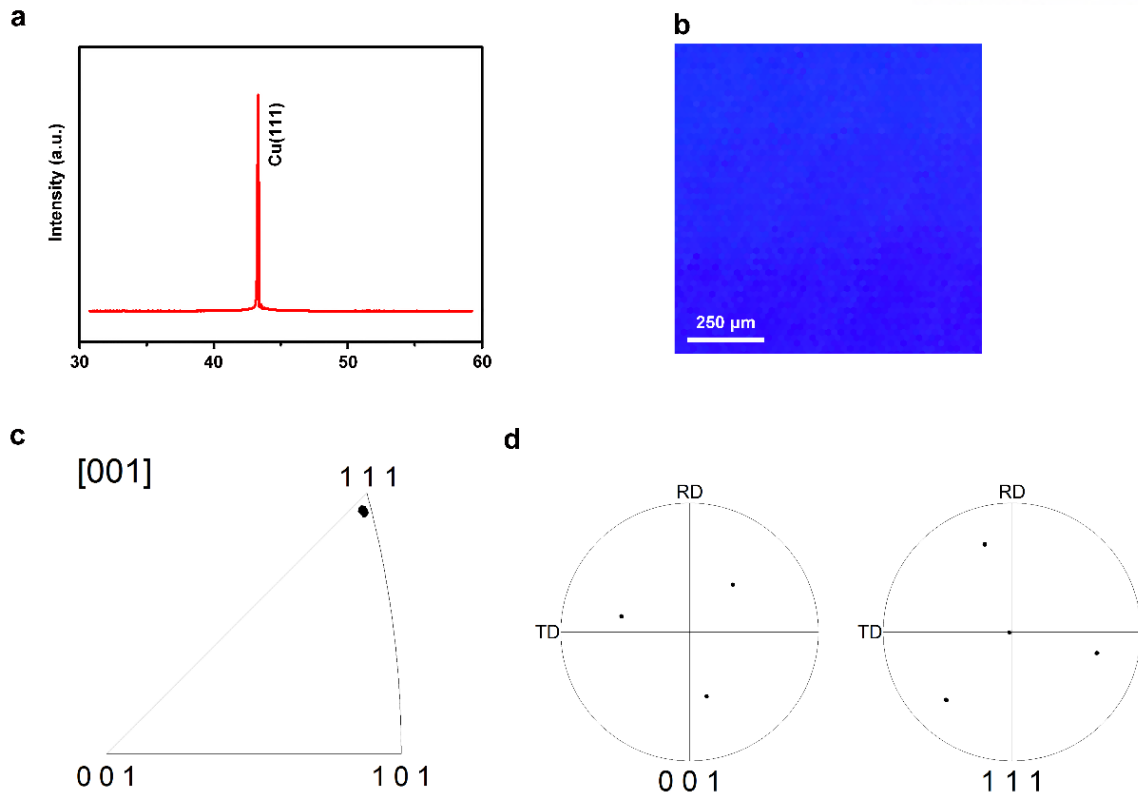


Figure 2.8 (a) XRD and (b-d) EBSD characterizations of a Cu(111) foil produced through thermal annealing of polycrystalline Cu foil.

Commercial silica particles were used as catalyst to grow graphene ribbons, and the XRD and TEM characterizations of the (previously, silica) particles are detailed in **Figure 2.9**. To disperse silica particles on the Cu foil, 10 μg of silica particles was added to 50 mL of deionized (DI) water. After ultrasonic mixing for 30 min, the dispersion was spin-coated onto the Cu foil at 1500 rpm for 30s. The Cu foils were then cut into small pieces to grow graphene ribbons.

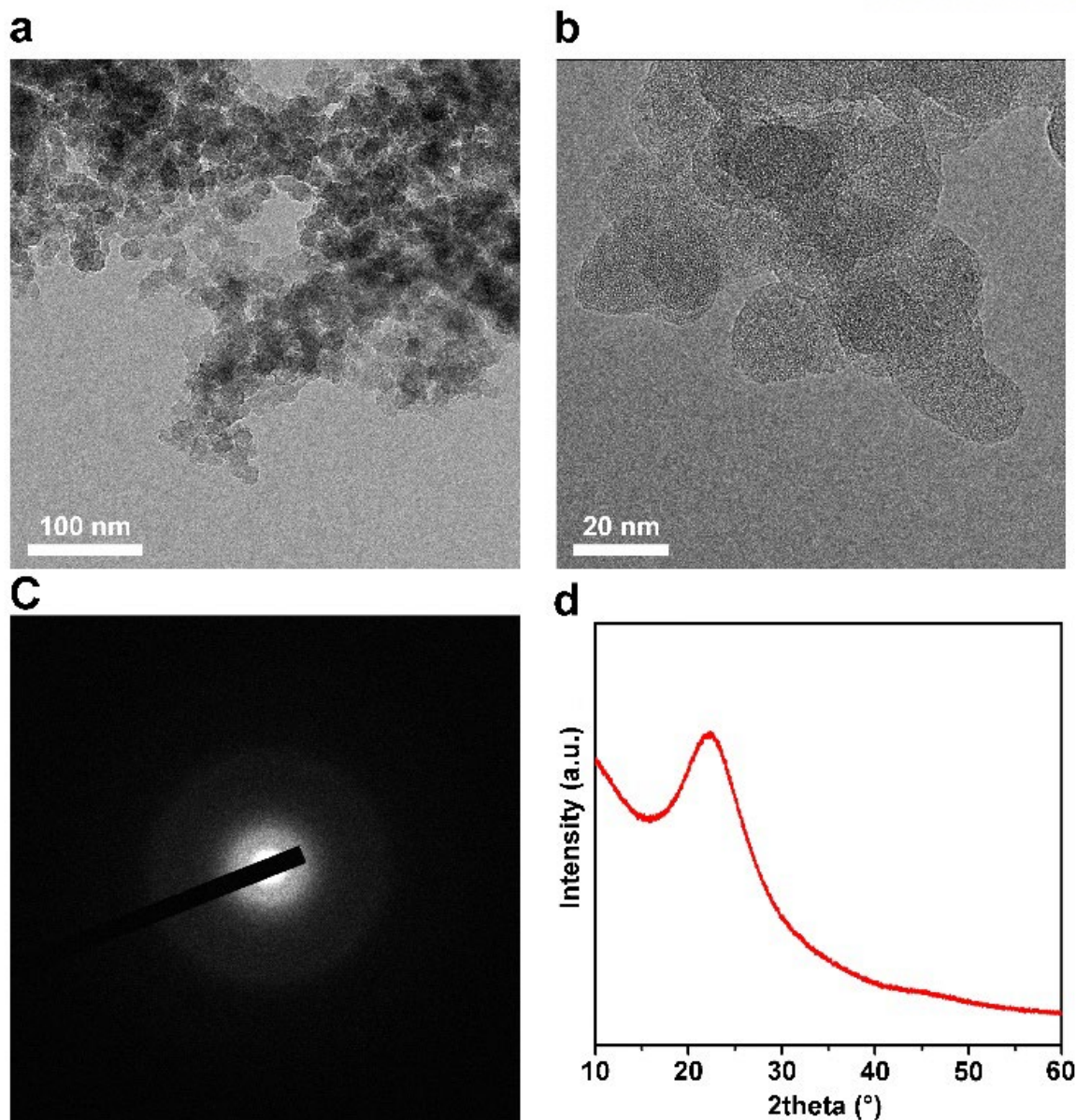


Figure 2.9 (a-c) HRTEM study of amorphous silica particles. The average particle size (from 50 particles) is 20 nm. (d) XRD of the silica particles. A single broad peak ($2\theta = 21.8^\circ$) is observed indicating that the silica particles used are amorphous.

For graphene ribbon growth, we introduced 500 SCCM Ar, 200~250 SCCM H₂ and 0.2~0.5 SCCM 1% C₂H₄ diluted in Ar for 20~50 mins at 950 °C (760 Torr). The growth temperature-time profile is shown in Figure S5. For isotopic ¹³C labelled experiments, we first used 500 SCCM Ar, 250 SCCM H₂ and 0.3 SCCM 1% diluted C₂H₄ in Ar at 25 mins. The diluted C₂H₄ gas was then switched off followed by immediately introducing 2 SCCM ¹³CH₄ gas for a certain time after pumping out the remaining diluted C₂H₄ gas and recovering to atmospheric pressure within 5 mins.

After growth, the graphene ribbons were transferred using a poly methyl methacrylate (PMMA)-coated wet etching method. First, the top foil surface was spin-coated with PMMA (3000 rpm for 60s) and an H₂ plasma washer (120 W, 10 mins) was used to remove graphene on the backside of the Cu foil. Then, a mixed solution (250 mL DI water, 20 mL ~30% hydrochloric acid and 3 mL ~30% hydrogen peroxide in water) was used to etch the Cu foil substrate. The PMMA-coated sample was floated on the surface of the mixed solution and left to stand for 1.5 h. After all the Cu foil was etched away, a 0.2 mm-thick Polyethylene terephthalate (PET) film was used to transfer the PMMA/GRs into DI water for washing for 30 mins. Finally, PMMA/Graphene ribbons were transferred onto the target substrate and the PMMA film was removed by washing successively with acetone, ethanol and DI water.

References

- [1] Fan, X. G.; Forsberg, F.; Smith, A. D.; Schroder, S.; Wagner, S.; Rodjegard, H.; Fischer, A. C.; Ostling, M.; Lemme, M. C.; Niklaus, F., Graphene ribbons with suspended masses as transducers in ultra-small nanoelectromechanical accelerometers. *Nat Electron* **2019**, *2* (9), 394-404.
- [2] Kato, T.; Hatakeyama, R., Site- and alignment-controlled growth of graphene nanoribbons from nickel nanobars. *Nat Nanotechnol* **2012**, *7* (10), 651-656.
- [3] Huang, P. Y.; Ruiz-Vargas, C. S.; van der Zande, A. M.; Whitney, W. S.; Levendorf, M. P.; Kevek, J. W.; Garg, S.; Alden, J. S.; Hustedt, C. J.; Zhu, Y.; Park, J.; McEuen, P. L.; Muller, D. A., Grains and grain boundaries in single-layer graphene atomic patchwork quilts. *Nature* **2011**, *469* (7330), 389-+.
- [4] Norimatsu, W.; Kusunoki, M., Selective formation of ABC-stacked graphene layers on SiC(0001). *Phys Rev B* **2010**, *81* (16).
- [5] Milani, A.; Tommasini, M.; Russo, V.; Bassi, A. L.; Lucotti, A.; Cataldo, F.; Casari, C. S., Raman spectroscopy as a tool to investigate the structure and electronic properties of carbon-atom wires. *Beilstein J Nanotech* **2015**, *6*, 480-491.
- [6] Wu, J. B.; Lin, M. L.; Cong, X.; Liu, H. N.; Tan, P. H., Raman spectroscopy of graphene-based materials and its applications in related devices. *Chem Soc Rev* **2018**, *47* (5), 1822-1873.
- [7] Mironova-Ulmane, N.; Kuzmin, A.; Steins, I.; Grabis, J.; Sildos, I.; Pars, M., Raman scattering in nanosized nickel oxide NiO. *J Phys Conf Ser* **2007**, *93*.
- [8] Li, Y.; Qiu, W. L.; Qin, F.; Fang, H.; Hadjiev, V. G.; Litvinov, D.; Bao, J. M., Identification of Cobalt Oxides with Raman Scattering and Fourier Transform Infrared Spectroscopy. *J Phys Chem C* **2016**, *120* (8), 4511-4516.
- [9] Yang, G.; Fu, X. J.; Zhou, J., Dielectric properties of the silver-copper alloy films deposited by magnetron sputtering. *J Opt Soc Am B* **2013**, *30* (2), 282-287.
- [10] Wu, M. H.; Zhang, Z. B.; Xu, X. Z.; Zhang, Z. H.; Duan, Y. R.; Dong, J. C.; Qiao, R. X.; You, S. F.; Wang, L.; Qi, J. J.; Zou, D. X.; Shang, N. Z.; Yang, Y. B.; Li, H.; Zhu, L.; Sun, J. L.; Yu, H. J.; Gao, P.; Bai, X. D.; Jiang, Y.; Wang, Z. J.; Ding, F.; Yu, D. P.; Wang, E. G.; Liu, K. H., Seeded growth of large single-crystal copper foils with high-index facets. *Nature* **2020**, *581* (7809), 406-+.
- [11] Nagai, M.; Nakanishi, K.; Takahashi, H.; Kato, H.; Makino, T.; Yamasaki, S.; Matsumoto, T.; Inokuma, T.; Tokuda, N., Anisotropic diamond etching through thermochemical reaction between Ni and diamond in high-temperature water vapour. *Sci Rep-Uk* **2018**, *8*.
- [12] Jin, S.; Huang, M.; Kwon, Y.; Zhang, L. N.; Li, B. W.; Oh, S.; Dong, J. C.; Luo, D.; Biswal, M.; Cunnning, B. V.; Bakharev, P. V.; Moon, I.; Yoo, W. J.; Camacho-Mojica, D. C.; Kim, Y. J.; Lee, S. H.; Wang, B.; Seong, W. K.; Saxena, M.; Ding, F.; Shin, H. J.; Ruoff, R. S., Colossal grain growth yields single-crystal metal foils by contact-free annealing. *Science* **2018**, *362* (6418), 1021-+.

III Kinetics of the Dissolution of diamond (100) and (110) Single Crystals in Nickel and Cobalt Films

3.1 Introduction

Diamond has the highest atom concentration and thermal conductivity, the largest shear modulus and shear strength, the highest tensile strength, and the highest hardness of all known materials, among other exceptional properties¹⁻⁵. Due to these remarkable properties, there is a wide range of potential applications of bulk diamond and diamond thin films^{2,6-8}. Yet, in order to fully utilize the whole array of diamond based structures' potential, it is indispensable to develop an efficient method of diamond patterning and surface morphology modification. Conventional patterning methods, such as hard mask⁹ or lithography¹⁰ based reactive ion etching (RIE), molding¹¹, laser patterning¹² are time consuming and might entail considerable damage of the diamond¹³⁻¹⁷. Alternatively, it has recently been demonstrated that water vapor enables the continuous dissolution of carbon from single crystal diamond with (100) and (110) surface orientation into thin nickel film^{18,19}. However, to date there has not been any comprehensive study on the interaction between diamond and metal at the metal-diamond interface, the dissolution of C and its diffusion in the metal film as well as the water induced reaction at the open metal surface.

Our work is a comprehensive experimental and theoretical study on the kinetics of the dissolution of single crystal diamond with the (100) and (110) surface planes into Ni and Co films. Two experimental systems were used to elucidate the diamond dissolution process. The first one is a conventional isothermal hot wall (quartz tube) system which was used to determine the corresponding activation enthalpies for diamond dissolution and water induced metal surface reactions. The other experimental setup used in our study is a cold wall system that has a joule heating sample holder (i.e., resistive heating) which can heat from room temperature to, e.g., 1050 °C, within 10 seconds and cool down from 1050 °C to room temperature within 8 seconds. The fast-cooling regime enables “trapping” of the carbon atoms dissolved in the metal film so that we were able to observe the carbon concentration gradient in the metal films by time of flight-secondary ion mass spectrometry (ToF-SIMS).

The epitaxial relation at the metal-diamond interface has been studied by synchrotron-based XRD, powder XRD and variable temperature *in-situ* XRD measurements. We have also conducted the DFT modeling for the reactions at the metal open surface and at the metal/diamond interface to thoroughly describe the diamond dissolution process.

3.2 Results and discussion

3.2.1 Quartz tube furnace experiments

In order to study the kinetics of diamond dissolution, we sputter deposited 500-nm thick Ni and Co films onto the single crystal diamond plates of (100) and (110) surface orientation. After heat treatment of 500-nm thick Ni film coated single crystal diamond plate with a (100) surface (see **Figure 3.1** for EBSD characterization on three types of single crystal diamond plates with a (100), (110) and (111) surface) at 1009 ± 1 °C for 30 mins under a 1000 sccm flow of Ar(g) at 760 ± 1 Torr pressure followed by cooling to room temperature in 15 mins, graphite films were observed on the surface of the Ni film and at the Ni/D(100) interface.

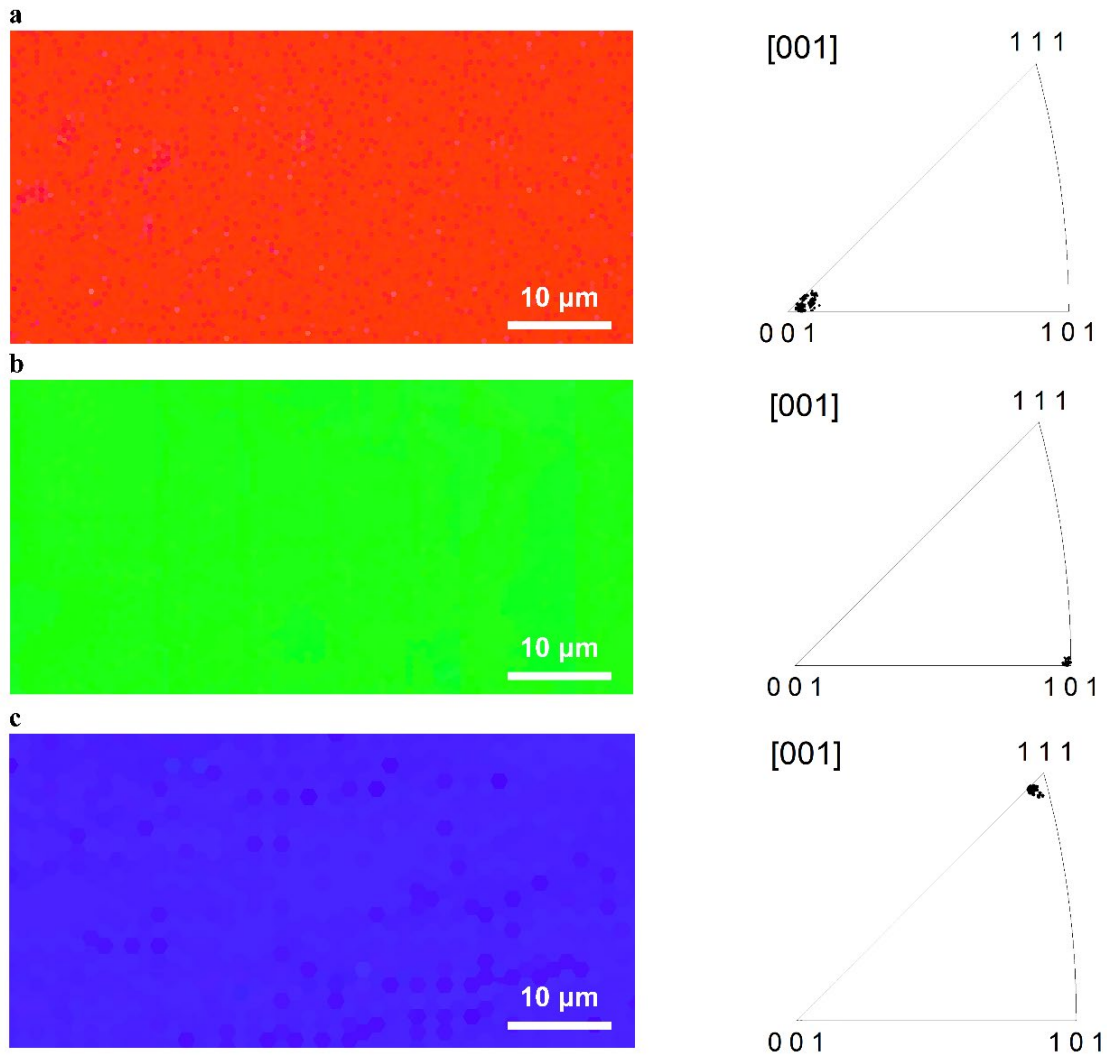


Figure 3.1 EBSD characterization of (a) a 1 mm-thick single crystal diamond plate with a (100) surface, (b) a 0.3 mm-thick single crystal diamond plate with a (110) surface, and (c) a 1 mm-thick single crystal diamond plate with a (111) surface.

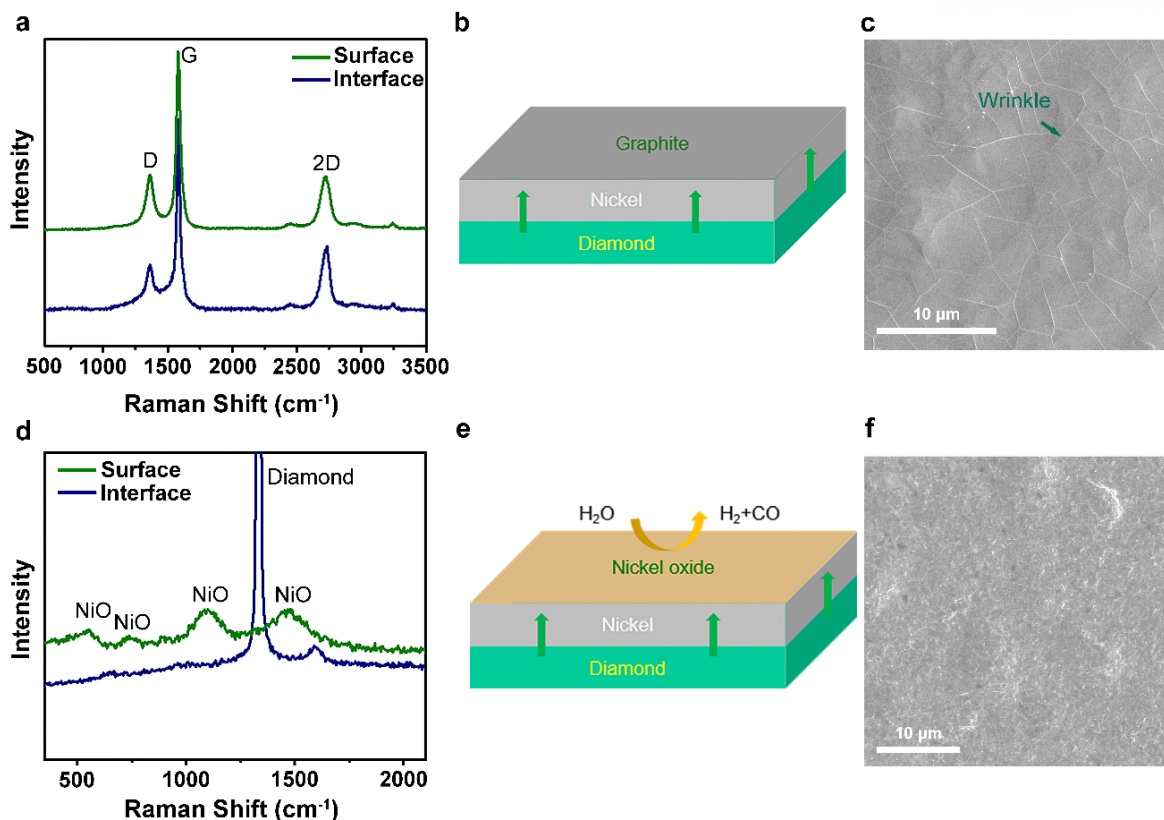


Figure 3.2 (a) Raman spectra after experiment without water vapor that were measured at the open metal surface (upper spectrum), and at the diamond surface after removal of the Ni film (lower spectrum). (b) Schematic of the Ni-diamond system; the green arrows show the diffusion direction of the C atoms. (c) SEM image of graphite film formed on the open Ni surface. (d) Raman spectra obtained after the experiment with water vapor present in the quartz chamber which were measured at the open metal surface (upper spectrum) and at the diamond surface after the removal of the $\text{Ni}_x\text{O}_y/\text{Ni}$ film (lower spectrum). (e) Schematic of C diffusion through a Ni film and oxidation of C atoms at the open Ni surface. (f) SEM image of the nickel (oxide) surface.

The Raman spectra of these graphite films (D $\sim 1350\text{ cm}^{-1}$, G $\sim 2580\text{ cm}^{-1}$ and 2D $\sim 2700\text{ cm}^{-1}$ band)²⁰ are shown in **Figure 3.2a**. The Raman characterization suggests that some of the C at the Ni/D(100) interface “dissolved” and diffused into and through the Ni film at $1009\pm 1\text{ }^\circ\text{C}$. The configuration of the Ni-diamond sample and the direction of C diffusion are schematically shown in **Figure 3.2b**. The scanning electron microscope (SEM) images (**Figure 3.2c**) show wrinkles²¹ in the graphite film formed on the metal surface. After the Ni film was removed wrinkles were also observed in the graphite film on the diamond surface, which had been formed at the Ni/D(100) interface (**Figure 3.3a**). Note that no further dissolution of diamond was detected after prolonged heat treatment (over 12 hours) of the samples (500-nm thick Ni film on the D(100) surface) under the conditions mentioned above.

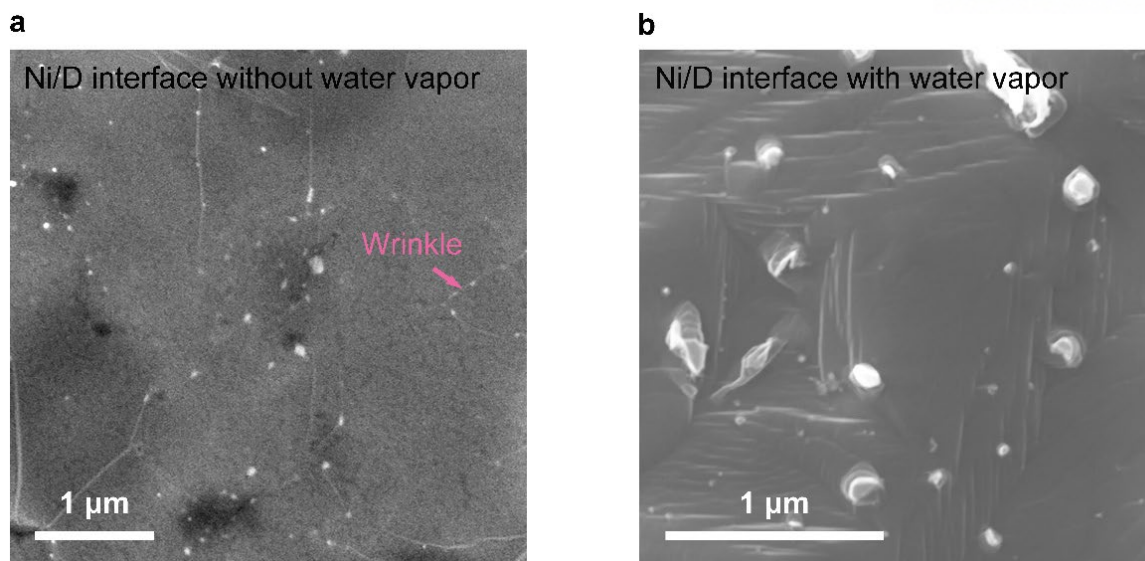


Figure 3.3 SEM images of (a) wrinkled graphite film on the diamond surface; a Ni/D sample was heat treated at 1009 ± 1 °C for 30 mins in Ar(g) (760 ± 1 Torr) atmosphere with no water vapor present. (b) Bare diamond surface; a Ni/D sample was exposed to 1009 ± 1 °C temperature for 30 mins, during which water vapor mixed with Ar(g) flowed through the reaction chamber (760 ± 1 Torr pressure; no graphite/graphene was found).

In contrast, with water vapor present (see the configurations for quartz tube furnace experiments and for the “RSR-M” cold wall system experiments that are described in the next section in **Figures 2.7-2.8**) in the quartz tube reaction chamber during the heat treatment at 1009 ± 1 °C (see details in **Figure 2.5** and the notes for temperature calibration) for 30 mins under a 1000 sccm flow of Ar(g) at 760 ± 1 Torr total pressure, an oxide layer was formed at the open metal surface and the continuous dissolution of diamond at the metal/diamond interface was observed, as shown in **Figure 3.2d**. Evidently H₂O reacts with the Ni film, and the dissolved C is essentially removed “by” the water vapor as reported by Nagai et al¹⁸. The concentration gradient of C in the Ni or Co film established by the continuous removal of C at the surface drives the continuous dissolution of the diamond at the M/D(100) interface as shown schematically in **Figure 3.2e**. Raman (**Figure 3.2d**) and SEM (**Figure 3.2f**) analyses show that no graphite film was formed on the open metal surface and this is because the C could be continuously removed by the water vapor. After the Ni film was removed, no graphite film was observed at the Ni/D(100) interface, as shown in **Figure 3.3b**. Owing to the driving force of the C concentration gradient (which is formed and maintained by the continuous reaction between water vapor and C at the open metal surface), C atoms continuously diffuse from the interface to the open metal surface; this continuous ‘outflow’ of C prevents the formation of graphene/graphite at the metal/diamond interface. The Ni/D(110) results are similar to the results on Ni/D(100) described above.

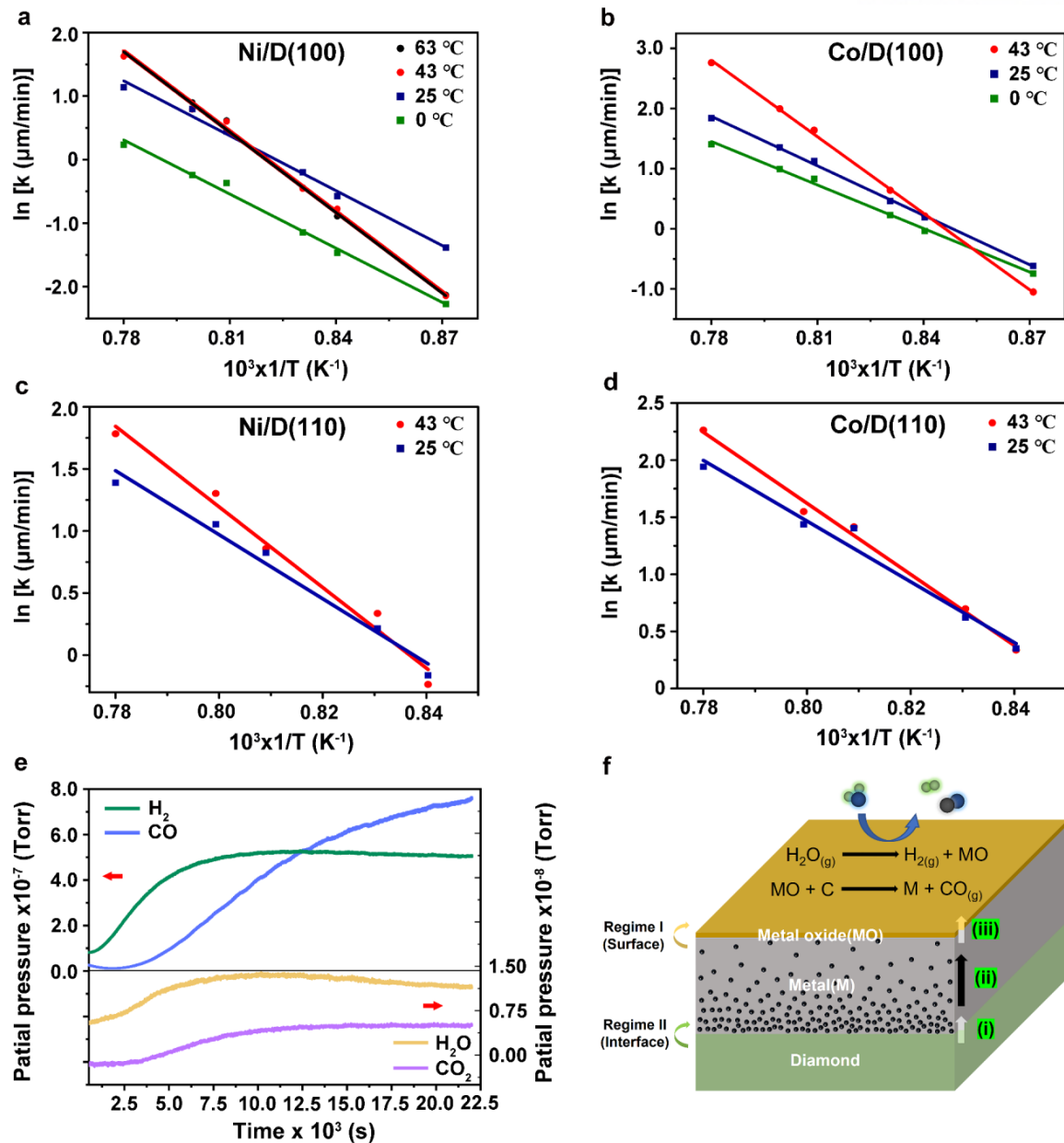


Figure 3.4 (a-b) Arrhenius plots of the dissolution rates of single crystal diamonds with (100) surfaces coated with (a) a 500-nm thick Ni film and (b) a 500-nm thick Co film, at different water bubbler temperatures. (c-d) Arrhenius plots of the dissolution rates of single crystal diamond with (110) surfaces coated with (c) 500-nm thick Ni film, and (d) 500-nm thick Co film, at different water bubbler temperatures. (e) Real-time residual gas analyzer (RGA) analysis of water vapor-Ni-diamond reaction products. (f) Schematic of diamond dissolution with water vapor present: the surface reaction (regime I when this is rate limiting, step (iii)) and the metal diamond interface where diamond dissolves into the metal through breaking of C-C bonds at the M-D interface (regime II when this is rate limiting, step (i)). Step (ii) represents diffusion of C atoms through the Ni film—this is never rate limiting for our study.

The collisional flux (Z_{surf})²² of H₂O molecules on the metal surface is, per the ideal gas law:

$$Z_{surf} = \frac{P_v}{(2\pi mkT)^{1/2}} \quad \text{Eq 3.1}$$

where P_v is the partial pressure of water vapor estimated by measuring the water loss in the bubbler, m is the mass of a water molecule, k is the Boltzmann constant and T is the absolute sample temperature (in Kelvin). At 0 °C (bubbler temperature), the mole fraction of H₂O (in Ar(g)) is 0.0062 and the collisional flux at 1009±1 °C is 1.1E+7 nm⁻²s⁻¹. At the bubbler temperature of 43 °C the mole fraction increased to 0.077 and the collisional flux at 1009±1 °C increased ~12x to 1.35E+8 nm⁻² s⁻¹. The detailed values of the measured mass loss of water in the bubbler, and the collisional flux and mole fractions are shown in **Tables 3.1-3.2**.

Table 3.1 Water weight loss in the water bubbler at different bubbler temperatures. The values were obtained by averaging three values of water weight loss in the bubbler (each value was measured after 1 hour of Ar(g) flow through the bubbler during 3-hour experiments).

T/ °C	0 °C	25 °C	43 °C	63 °C
Calculated²³ (g/h)	0.31	1.46	4.48	13.97
Experimental (g/h)	0.30	1.27	4.02	12.88

Table 3.2 Calculated and experimental values obtained for the collisional flux Z_{surf} and the mole fraction at different bubbler temperatures.

	T/ °C	0 °C	25 °C	43 °C	63 °C
Calculated Z_{surf} ($\text{nm}^{-2}\text{s}^{-1}$)	917±1	1.16E+7	5.36E+7	1.55E+8	4.10E+8
	963±1	1.14E+7	5.26E+7	1.52E+8	4.02E+8
	1009±1	1.12E+7	5.16E+7	1.49E+8	3.95E+8
Mole fraction (X_v)		0.0064	0.029	0.085	0.225
Experimental Z_{surf} ($\text{nm}^{-2}\text{s}^{-1}$)	917±1	1.13E+7	4.68E+7	1.40E+8	3.84E+8
	963±1	1.11E+7	4.59E+7	1.38E+8	3.77E+8
	1009±1	1.09E+7	4.50E+7	1.35E+8	3.70E+8
Mole fraction (X_v)		0.0062	0.026	0.077	0.21

Figures 3.4a-d show Arrhenius plots for the rates of dissolution of D(100) and D(110) in 500-nm thick Ni and Co films, measured for different water vapor partial pressures (i.e., at different temperatures of the water bubbler unit) at the sample temperature range of 875-1009±1 °C (the corresponding values of the dissolution rates are provided in **Tables 3.3-3.4**). Based on the fact that for each D/Metal system two different slopes (activation energies) were obtained for the Arrhenius plots at different water bubbler temperatures, we may suggest two regimes (referred to as Regime I and Regime II for relatively low (≤ 25 °C) and high (≥ 43 °C) water bubbler temperatures, respectively) to describe the water induced diamond dissolution process. The Arrhenius plots in **Figure 3.4a** and **b** have essentially identical slopes for bath temperatures of 0 °C and 25 °C even though the concentration of water vapor is about 4x higher at 25 °C than at 0 °C (Mole fraction in Argon gas: 0.0064 for 0 °C and 0.0029 for 25 °C). For water bubbler temperatures of 43 °C and 63 °C, we discovered for 500-nm thick Ni film on D(100) plate, that the dissolution rates and the slopes of the Arrhenius plots are essentially identical.

Table 3.3 Dissolution rates of D(100) coated with a 500-nm thick Ni/Co film. Each value is the average of three independent values. We used a 3D microscope to measure the depth of dissolved diamond after removing the Ni/Co film.

	T/°C	0 °C ($\mu\text{m}/\text{min}$)	25 °C ($\mu\text{m}/\text{min}$)	43 °C ($\mu\text{m}/\text{min}$)	63 °C ($\mu\text{m}/\text{min}$)
Ni/D(100)	875±1	0.1034	0.2513	0.1168	0.1193
	917±1	0.2307	0.5629	0.4090	0.4105
	931±1	0.3192	0.8222	0.6332	0.6464
	963±1	0.6944	1.559	1.825	1.851
	978±1	0.7859	2.218	2.439	2.462
	1009±1	1.266	3.124	5.073	5.090
Co/D(100)	875±1	0.4752	0.5411	0.3505	N/A
	917±1	0.9654	1.211	1.238	N/A
	931±1	1.259	1.587	1.902	N/A
	963±1	2.300	3.090	5.162	N/A
	978±1	2.704	3.870	7.369	N/A
	1009±1	4.083	6.322	15.86	N/A

Table 3.4 Dissolution rates of D(110) coated with 500-nm thick Ni/Co film. Each value is the average of four independent values. We used a 3D microscope to measure the depth of dissolved diamond after removing the Ni/Co film.

	T/°C	25 °C ($\mu\text{m}/\text{min}$)	43 °C ($\mu\text{m}/\text{min}$)
Ni/D(110)	917±1	0.8557	0.7944
	931±1	1.240	1.398
	963±1	2.283	2.358
	978±1	2.870	3.685
	1009±1	4.011	5.953
Co/D(110)	917±1	1.421	1.422
	931±1	1.861	2.007
	963±1	4.072	4.124
	978±1	4.212	4.710
	1009±1	6.970	9.610

The values of the activation enthalpy ΔH^\ddagger , and the pre-factor, A , measured for the diamond dissolution rates, k ($\ln k = -\Delta H^\ddagger/RT + \ln A$), in Regimes I and II are given in **Table 3.5** for D(100) and D(110). We note that the experimental activation energies of C diffusion in Ni and Co reported in the literature are 137 kJ/mol (for the temperature range 873 K-1673 K) and 154 kJ/mol (for the temperature range 976 K-1673 K), respectively.^{24,25} These reported values are substantially lower than the ΔH^\ddagger values obtained for both Regimes. This suggests that diffusion of C through the Ni or Co films is not the rate limiting step in either Regime.

Table 3.5 ΔH^\ddagger and pre-factor A values, from a study of the dissolution of D(100) and D(110) coated with a 500-nm thick Ni or Co film. Arrhenius equation: $\ln k = \frac{-\Delta H^\ddagger}{R} \left(\frac{1}{T}\right) + \ln A$, where k is the dissolution rate, ΔH^\ddagger is the activation enthalpy, A is the pre-exponential factor, R is the universal gas constant, T is the temperature of the sample (in Kelvin). Note that the activation enthalpies and the prefactors were calculated by measuring the depth of the dissolved section in the diamond plate after the experiment.

	T/°C	Activation enthalpy ΔH^\ddagger (kJ/mol)	Prefactor A (units $\mu\text{m/s}$)
Ni/D(100)	0	236±6	1.00±0.15
	25	240±5	1.10±0.10
	43	351±7	1.66±0.14
	63	350±6	1.56±0.14
Co/D(100)	0	201±5	0.92±0.08
	25	228±4	1.05±0.05
	43	353±5	1.60±0.07
Ni/D(110)	25	214±4	0.98±0.05
	43	270±5	1.23±0.05
Co/D(110)	25	221±4	1.03±0.06
	43	266±3	1.20±0.05

Metal film geometry and kinetics of diamond dissolution obtained as a function of mass loss of diamond:
We also acquired the Arrhenius parameter based on the mass difference (mass loss) of the diamond plates before and after the dissolution experiments. First of all, based on the dissolution depth (**Figure 3.5a**) and the mass loss (**Figure 3.5b**) measurements, it is evident that the diamond dissolution rate is constant.

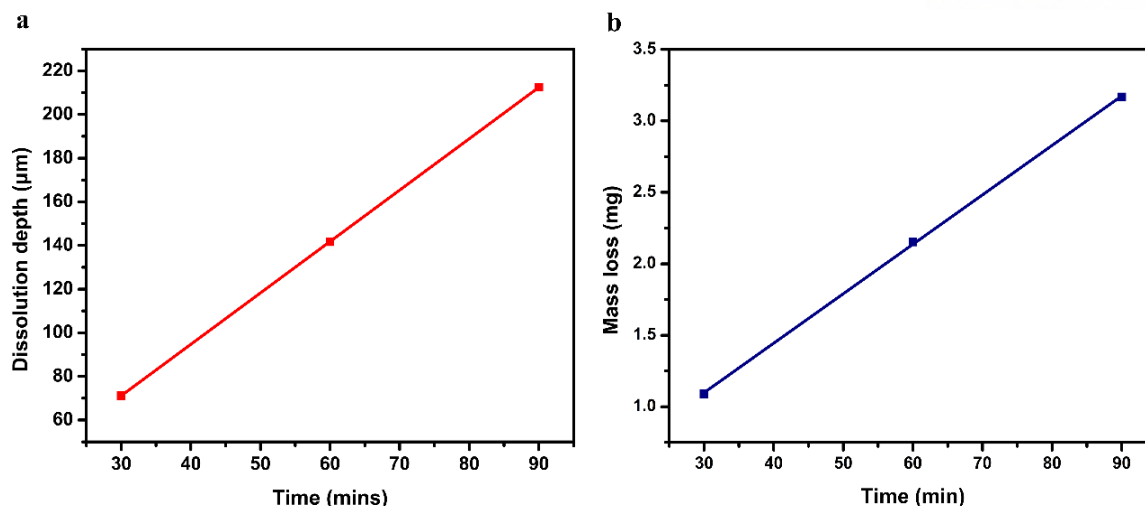


Figure 3.5 Dissolution depth and mass loss *versus* time for D(110) coated with 500-nm thick Ni film at 963 °C with the water bubbler temperature of 43 °C.

Tables 3.6 and **3.7** show the rates of D(110) mass loss coated with 500-nm thick Ni and 500-nm thick Co films, respectively. The corresponding Arrhenius plots are shown in **Figures 3.6a, b**. The activation enthalpies and the pre-exponential factors of the Arrhenius plots obtained based on the diamond mass loss measurements are provided in **Table 3.8**. The obtained ΔH^\ddagger values of D(110) are 224 ± 3 kJ/mol for Ni and 191 ± 3 kJ/mol for Co (the bubbler temperature of 25 °C), and 258 ± 2 kJ/mol for Ni and 259 ± 3 kJ/mol for Co (the bubbler temperature of 43 °C). These values agree well with the activation enthalpies obtained for the depths of dissolution (214 ± 4 kJ/mol for Ni and 221 ± 4 kJ/mol for Co (bubbler temperature 25 °C), and 270 ± 5 kJ/mol for Ni and 266 ± 3 kJ/mol for Co (bubbler temperature 43 °C)). The pre-exponential factors A determined by mass loss measurements are 0.83 ± 0.04 mg/s for Ni and 0.71 ± 0.04 mg/s for Co (the bubbler temperature of 25 °C), and 1.02 ± 0.05 mg/s for Ni and 1.01 ± 0.05 mg/s for Co (the bubbler temperature of 43 °C); from the measurements of depths, the corresponding pre-exponential factors are 0.98 ± 0.05 $\mu\text{m/s}$ for Ni and 1.03 ± 0.06 $\mu\text{m/s}$ for Co (the bubbler temperature of 25 °C), and 1.23 ± 0.05 $\mu\text{m/s}$ for Ni and 1.20 ± 0.05 $\mu\text{m/s}$ for Co (the bubbler temperature of 43 °C). The 3D microscope images of the D(110) samples after the dissolution experiments and after removing the Ni film by dipping in acid solution are shown in **Figure 3.7**. The images were taken for the 500-nm thick Ni film coated D(110) samples after 30 min, 60 min, and 90 min heat treatments at 963 °C (the bubbler temperature of 43 °C). Because of the partial dewetting of the Ni film, the side wall of the dissolved diamond region is not perfectly flat. **Figure 3.8** shows an optical microscope image of the entire dissolution region of the D(110) plate and a schematic illustrating two vertical D(111) side walls and two sloped D(111) sidewalls. The fraction of the projected area of the sloped sidewalls is quite

small compared to the “nominally flat” surface; we suggest this is why the mass loss is essentially a linear function of time.

Table 3.6 Mass loss dissolution rates of D(110) coated with 500-nm thick 2 x 2 mm Ni film.

Bubbler Temp (°C)	Sample Temp (°C)	Before (mg)	After (mg)	Time (min)	Mass loss (mg)	Mass loss rate (mg/min)
25	1009	9.634	6.804	45	2.830	0.063
	978	10.026	7.614	60	2.412	0.040
	963	11.468	9.616	60	1.852	0.031
	931	11.123	8.960	120	2.163	0.018
	917	11.601	9.871	140	1.730	0.012
43	1009	11.656	9.106	30	2.550	0.081
	978	9.681	6.797	60	2.884	0.048
	963	10.119	7.966	60	2.153	0.036
	931	11.525	10.382	60	1.143	0.019
	917	12.308	11.206	90	1.102	0.012

Table 3.7 Mass loss dissolution rates of D(110) coated with 500-nm thick 2 x 2 mm Co film.

Bubbler Temp (°C)	Sample Temp (°C)	Before (mg)	After (mg)	Time (min)	Mass loss (mg)	Mass loss rate (mg/min)
25	1009	11.753	8.651	30	3.102	0.103
	978	11.588	7.327	60	4.261	0.071
	963	9.833	6.174	60	3.659	0.061
	931	10.946	7.884	90	3.062	0.034
	917	11.861	9.519	90	2.342	0.026
43	1009	10.402	7.540	20	2.862	0.143
	978	9.651	7.162	30	2.489	0.083
	963	11.457	8.666	45	2.791	0.062
	931	9.925	7.943	60	1.982	0.033
	917	10.395	9.134	60	1.261	0.021

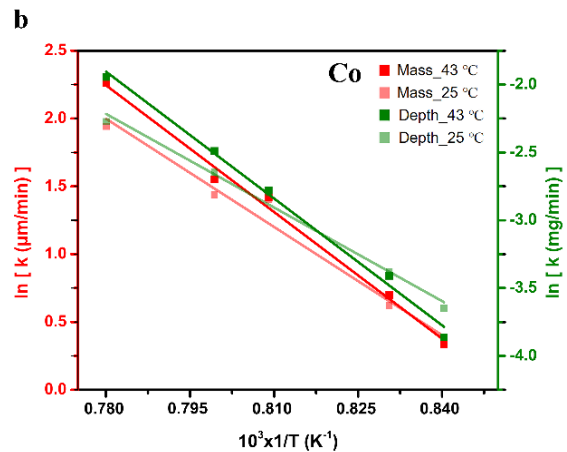
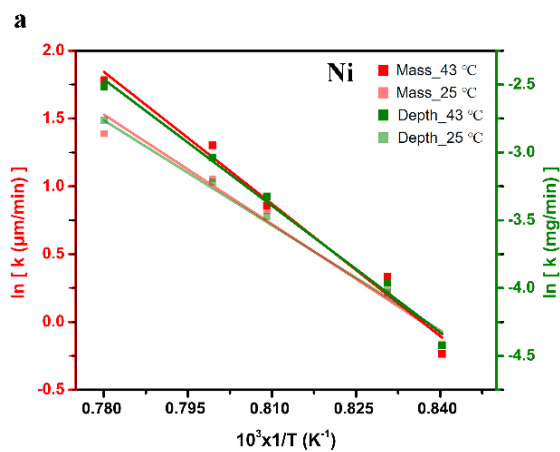


Figure 3.6 Arrhenius plots of the dissolution rates based on mass loss or dissolution depth of single crystal diamonds with (110) surfaces coated with (a) 500-nm thick Ni film and (b) 500-nm thick Co film at different water bubbler temperatures.

Table 3.8 ΔH^\ddagger and A' values of the dissolution of D(110) coated with 500-nm thick Ni film (2 mm x 2 mm) based on mass loss.

	T/°C	Activation enthalpy ΔH^\ddagger (kJ/mol)	Prefactor A' (units mg/s)
Ni	25	224±3	0.83±0.04
	43	258±2	1.02±0.05
Co	25	191±3	0.71±0.04
	43	259±3	1.01±0.05

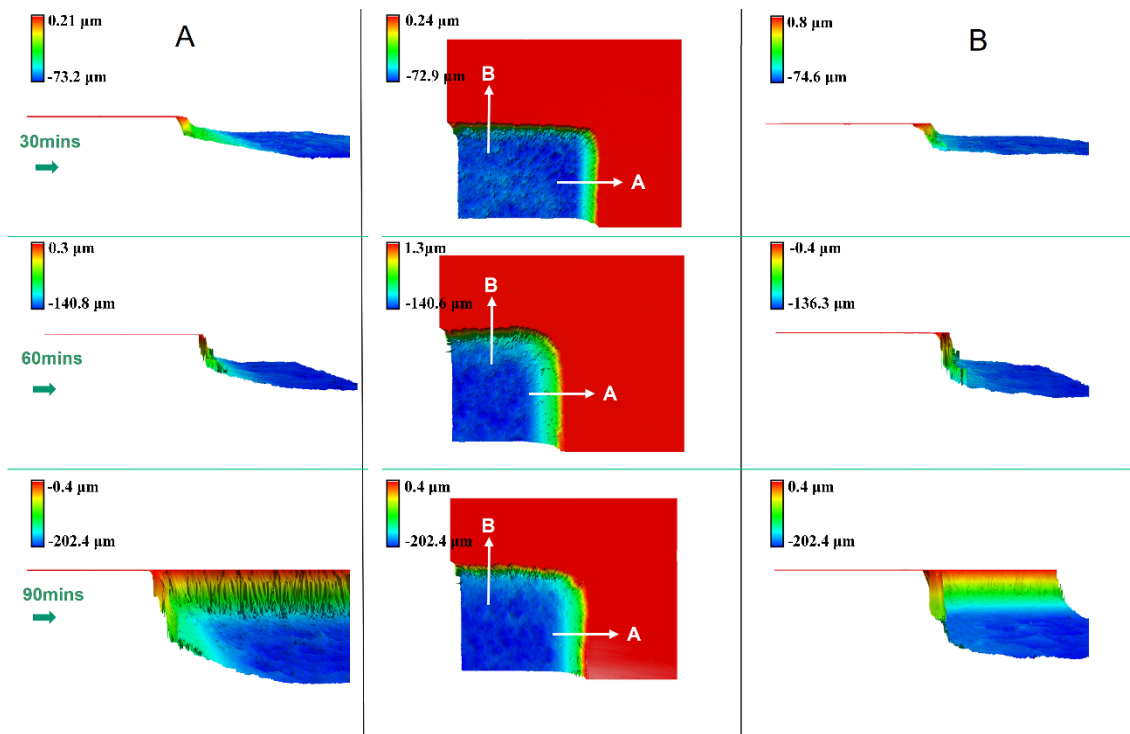


Figure 3.7 3D microscopic images of D(110) samples coated with a 500-nm thick Ni film and treated at 963 °C (the bubbler temperature of 43 °C) for 30 mins, 60 mins, and 90 mins of the heat treatment.

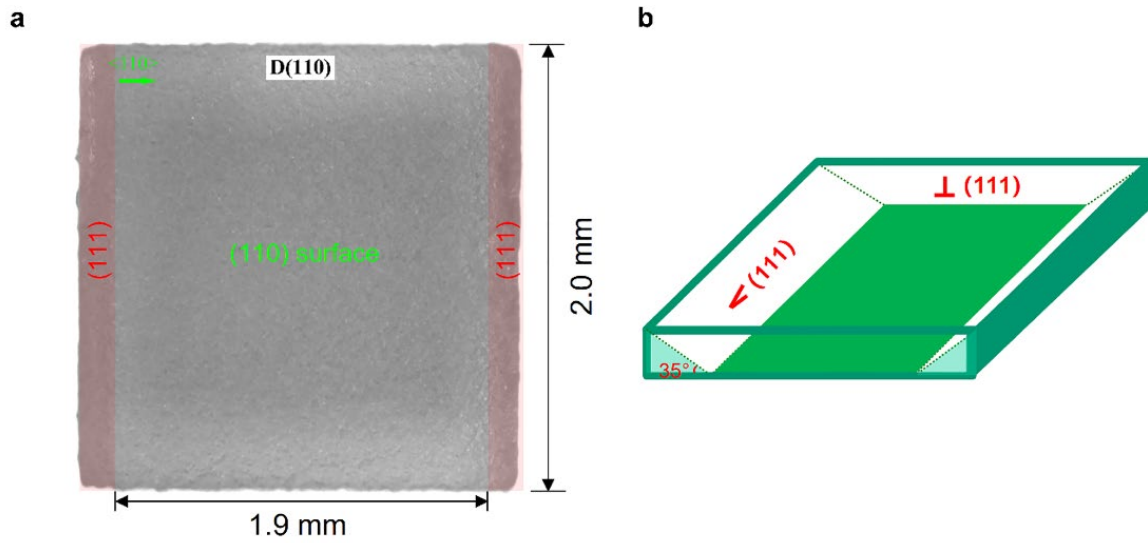


Figure 3.8 (a) An optical microscope (OM) image of the entire dissolution region of a D(110) plate and (b) its schematic image showing two vertical D(111) side walls and two sloping D(111) side walls.

We fitted the Arrhenius equation to the data reported by Nagai, et al¹⁸ of dissolution rates of D(100) coated with Ni film in the presence of water vapor (we assume their water bubbler temperature was 25 °C) at three different furnace temperatures (900, 950, and 1000 °C), obtaining 437 kJ/mol for the enthalpy of activation and 0.726 μm/s for the prefactor. Their reported maximum dissolution rate of ~8.7 μm/min at 1000 °C is higher than our value of 3.12 μm/min for Ni/D(100) at the furnace temperature of 1009 °C and at 25 °C bubbler temperature. Our results suggest that the Co film yields a much higher dissolution rate (up to 15.9 μm/min) of diamond than Ni coating, as shown in **Table 3.4**.

Tables 3.3 and 3.4 also show that the rate of dissolution of diamond into Co was *always* higher than that into Ni (up to 4.6x on D(100) and 1.7x on D(110)). The reported solubility at 1000 °C of C is 3.41 at% in Co and 2.03 at% in Ni²⁶. In general, the carbon diffusion coefficient in Ni or Co can be obtained from the following equation:

$$D_{dif} = A * \exp \frac{-E_a}{RT} \quad \text{Eq 3.2}$$

in which, D_{dif} is the diffusion coefficient, A the “frequency factor”, E_a the activation enthalpy, R the gas constant, and T the temperature (K). Based on the reported activation enthalpy and frequency factor at about 1000 °C^{24,25} we calculated $D_{dif}(Co) = 1.63E-7 \text{ cm}^2/\text{s}$ and $D_{dif}(Ni) = 2.78E-7 \text{ cm}^2/\text{s}$. $D_{dif}(Co)$

is lower than $D_{dif}(Ni)$, however, diamond has a higher rate of dissolution in Co. Thus, we suggest that “the normal rate” of diffusion of carbon atoms through the metal films doesn’t play a critical role in the difference in the rates of dissolution of diamond in Ni and Co films.

Could this higher rate of dissolution in Co versus into Ni be due to grain boundaries? Bulk Co has a martensitic transformation²⁷ at ~ 700 K, while Ni does not undergo such a phase change. The room temperature stable phase of Co is hcp (hexagonal closed-packed), and the high temperature stable phase is fcc (face-centered cubic). We found that the sputter-deposited polycrystalline Ni film converted to a Ni(100) film with single crystalline features on D(100) and to a Ni(110) film on the D(110) substrate, and that the sputter-deposited Co film also converted to Co(100) on D(100) and to Co(110) on D(110). **Figures 3.9a-b** show XRD patterns of 500-nm thick Ni and Co films on a D(100) substrate before (i.e., at room temperature), during (i.e., at 1000 °C), and after (i.e., returned to room temperature) heat treatment at 1000 °C (see details in the Experimental section), in which the Ni(111) peak present in the pattern of the as-deposited Ni film disappears, but the pattern for the Co film has some small peaks at 1000 °C that are assigned to hcp-Co(100) and hcp-Co(002). **Figures 3.9c-d** show XRD patterns from the Ni-coated D(110) substrate in which the Ni(111) peak was present during the XRD measurement and from the Co-coated D(110) in which some small peaks were also present after the measurement, that are assigned to hcp-Co(100) and hcp-Co(002).

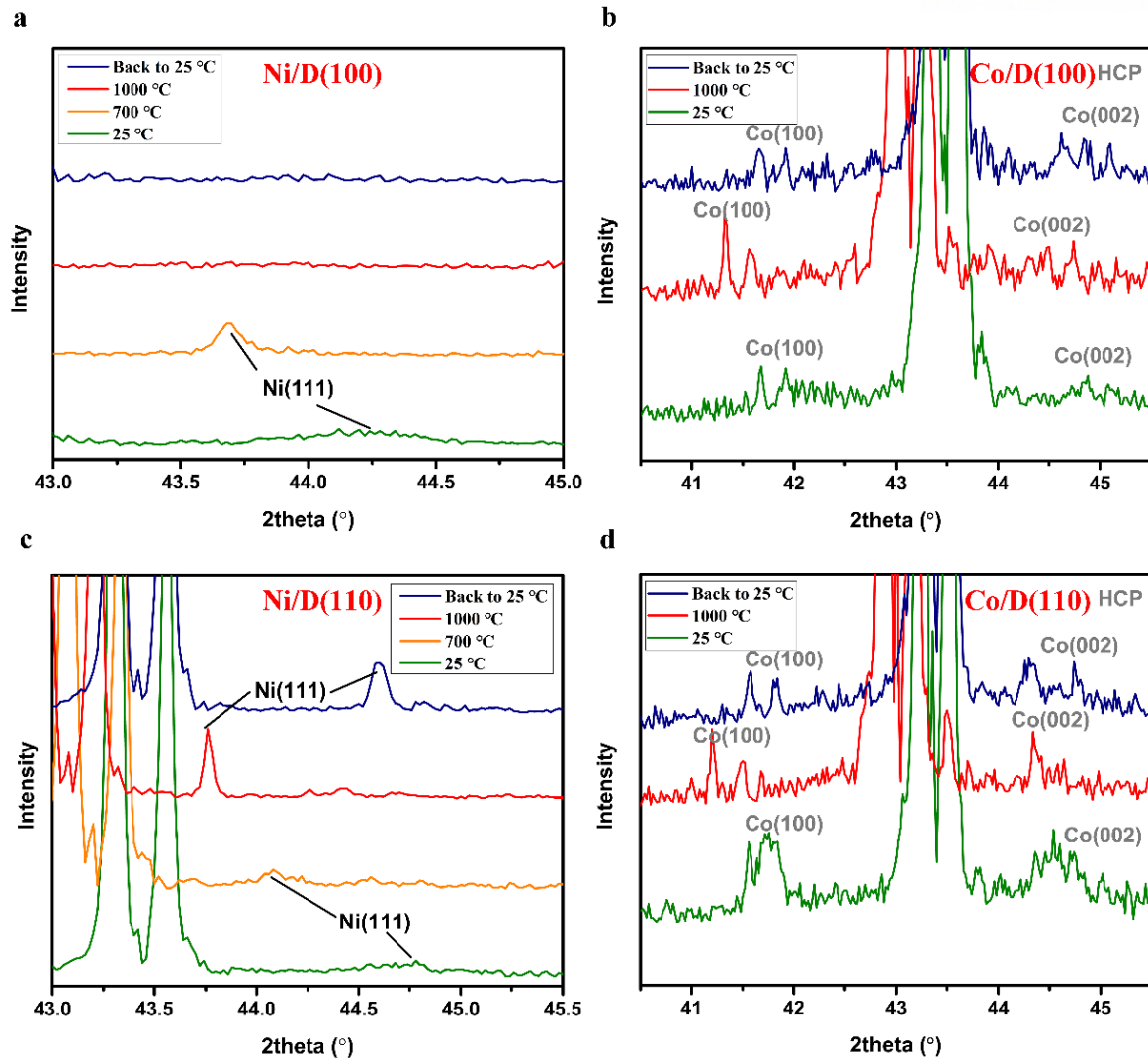


Figure 3.9 XRD patterns of Ni/Co films on (a-b) D(100), and (c-d) D(110) substrates. We note that there is no peak belonging to the Co film between 43 and 44 degrees and the background peaks in this range are due to the carbon paste we used to fix the sample for the variable temperature in-situ XRD measurements.

Considering the difference in the rates of dissolution of diamond in Ni and Co films on D(100) and also D(110) substrates (rate is up to 4.6x higher for Co than Ni for D(100) and 1.7x higher for Co than Ni for D(110)), could the density of grain boundaries and/or the type of grain boundaries cause these, because grain boundaries are reported to be “short circuits” for diffusion of C in fcc²⁸ metals? We suggest that this is perhaps not the case, and that the reason for the higher rate of dissolution in Co versus Ni is perhaps due to different C concentration gradients due to the more efficient removal of C from the Co “free surface”. Because there is no temperature gradient in our isothermal dissolution experiments, the “driving force” (e.g., if we consider single crystal Co and Ni films—simply for the

sake of discussion here) is the concentration gradient of C from the diamond-metal interface to the surface of the metal film. **Table 3.9** show the ratio of the rates of dissolution of diamond in Co versus Ni for D(100) and D(110), respectively. Note that the dissolution rate in Co is up to 4.5x higher than in Ni for D(100) and that the ratio of the rates depends on sample temperature (at 0 °C bath temperature— from a value of 4.6 (sample T was 875 °C) to 3.2 (sample T was 1009 °C), but is fairly constant for D(100) for bath temperatures of 25 °C (ratio is about 2 for all sample temperatures) and 43 °C (ratio is about 3 for all sample temperatures). For D(110) two bath temperatures (25 °C and 43 °C) were studied, and the ratio of rates is fairly constant for both, about 1.5, over all sample temperatures studied. While the differing rates of removal of diamond are of basic science interest, there is also a practical aspect in terms of achieving rapid removal of diamond; if speed is critical, it seems that cobalt could be used rather than nickel.

Table 3.9 Ratios of experimentally measured diamond dissolution rates (Co vs. Ni) for D(100) and D(110) samples (i.e., the ratio of the dissolution rate of Co coated D(1*k*0) to the dissolution rate of Ni coated D(1*k*0), where *k* is equal to either 0 or 1). (The dissolution rates and thus their ratios were calculated based on the dissolution depth measurements).

	T/°C	0 °C	25 °C	43 °C
D(100)	875±1	4.596	2.153	3.001
	917±1	4.185	2.151	3.027
	931±1	3.944	1.930	3.004
	963±1	3.312	1.982	2.828
	978±1	3.441	1.745	3.021
	1009±1	3.225	2.024	3.126
D(110)	917±1	N/A	1.661	1.790
	931±1	N/A	1.501	1.436
	963±1	N/A	1.784	1.749
	978±1	N/A	1.468	1.278
	1009±1	N/A	1.738	1.614

A home-built high vacuum (HV) mobile residual gas analyzer (RGA-mass spec) system was used to analyze the composition of the downstream gases (see details in the Experimental section). The RGA–CVD differential pumping configuration is schematically shown in **Figure 3.10**. **Figure 3.4e** shows the real-time partial pressure response curves of H₂, CO, H₂O and CO₂ gasses/vapors leaked through the metering valve from the CVD reaction chamber into the high vacuum gas analyzer system.

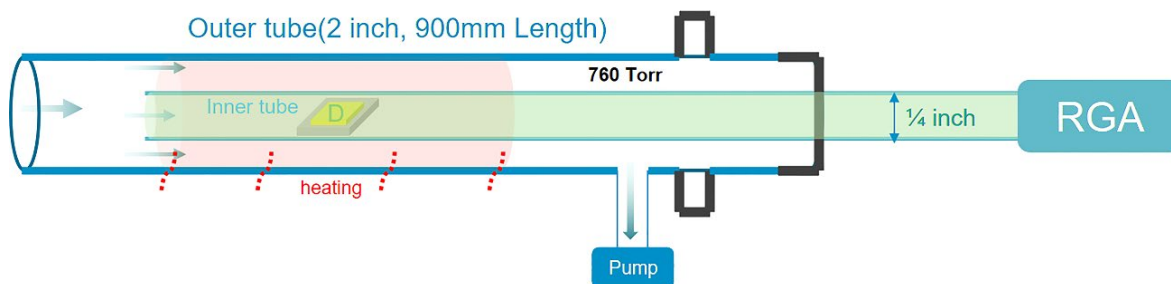


Figure 3.10 Schematic image of the combined CVD-RGA system.

First, we set the experimental conditions to establish a stable background RGA signal. After insertion of the samples into the hot reaction zone, the water vapor first reacts with the metal open surface resulting in an increase in the H₂ partial pressure as the oxide layer is being formed at the metal surface (the metal surface might have a very thin graphite film formed during the heating-up stage, but the amount if present would be essentially negligible; if present it would be quickly removed by the water vapor). Once the surface metal oxide layer is formed, the CO signal starts to increase. Thus, we establish a situation where the diamond is dissolving into the metal film and the C which is diffused through the metal film is removed by the water vapor. As time progresses, the H₂ and H₂O partial pressure got saturated, but CO partial pressure continued increasing because of the ‘*delay*’ time needed to form the oxide layer at the metal surface. As H₂O + C yields H₂ + CO, the time integrals (areas under the corresponding curves) of the H₂ and CO plots are close to equal. The CO₂ signal appeared later and saturated at a certain level which might be attributed to the water shift reaction (H₂O + CO → H₂ + CO₂)²⁹. The background signal with no metal coated diamond samples present in the hot zone is shown in **Figure 3.11**.

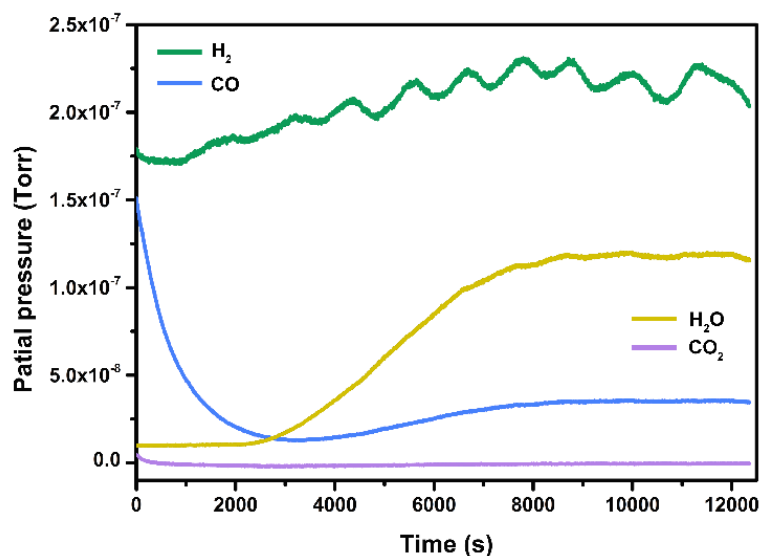


Figure 3.11 Response of the residual gas analyzer (RGA) to the gases/vapors leaked from the reaction chamber into the RGA chamber. The reaction chamber conditions: 1050 °C furnace temperature, 43 °C bubbler temperature, 760±1 Torr pressure. At ~2200 s, Ar(g) was switched to flow through the water bubbler (water vapor started to flow into the reaction chamber).

The process of the dissolution of diamond in Ni or Co films in the presence of water vapor involves 3 primary steps: (i) C-C bond breaking followed by the diffusion of C atoms into Ni or Co films at the metal/diamond interface, (ii) C diffusion through the 500-nm thick metal film, and (iii) the reaction of C atoms with a thin layer of metal oxide on the metal surface to form CO(g), as schematically shown in **Figure 3.4f**. The observed *constant rate* (**Figure 3.12**) of dissolution of diamond for a given water vapor partial pressure and a given diamond sample temperature suggests that the concentration gradient of C in the Ni or Co remains constant once it is established.

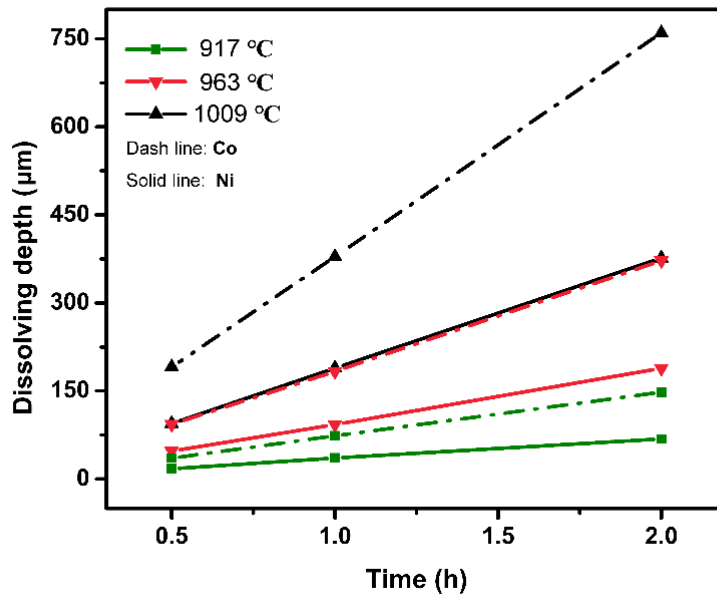


Figure 3.12 Diamond dissolution depths (depths to which 500-nm thick Ni/Co films “sank” into the D(100) due to dissolution of diamond) as a function of time at different sample temperatures (the bubbler temperature was 25 °C). Dashed and solid lines correspond to 500-nm thick Co on D(100) and 500-nm thick Ni on D(100) samples, respectively.

Besides, we found that water vapor completely oxidizes the Ni or Co film at a sample temperature of 850 °C or below and that this entirely inhibits the dissolution of diamond, apparently due to the metal oxide/diamond interface. In our study we did not observe any dissolution of the diamond/metal samples for temperatures at or below 850 °C.

We also studied lower sample temperatures with no water vapor present in the quartz tube furnace. **Figure 3.13** shows the Raman spectra measured at the Ni film surfaces of the Ni-D(100) samples which were heat treated for 3 hours at 600±1, 650±1 and 700±1 °C. The emergence of the G bands in the spectra of the samples heat treated at 650±1 °C and 700±1 °C (note that no characteristic graphene/graphite signatures were detected for the 600±1 °C sample) indicates that graphene/graphite formation at the open metal surface occurs at temperatures ≥650 °C. Further remarks on this topic for samples heat treated in the cold-wall system are given below.

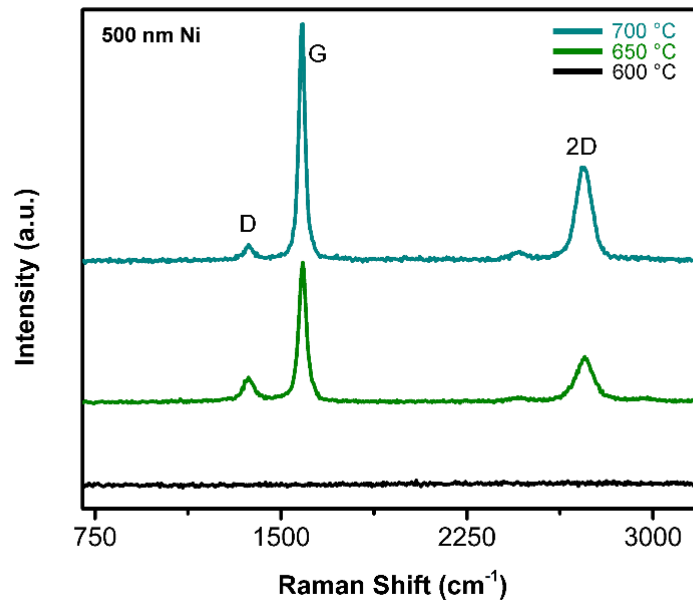


Figure 3.13 Raman spectra measured at the open Ni surfaces of the 500-nm thick Ni/D(100) samples heat treated at 600 °C, 650 °C, and 700 °C.

3.2.2 Cold wall system (RSR-M) experiments

To further study the mechanism of diamond dissolution at the M-D interfaces and removal of carbon at the open metal surfaces, we used a home-built cold wall system because it can be very rapidly heated to 1000 °C and from that temperature we can quench the samples to room temperature in 8 seconds. A spectropyrrometer was used to measure the sample temperature and its emissivity as a function of time (See details in the Experimental section). As shown in **Figure 3.14a**, the changes in the emissivity (blue data points) from about 0.4 to 0.75 and in the free Ni surface temperature (red data points) from about 1010 °C to 950 °C are caused by the formation of graphite on the open Ni surface³⁰. Then as we repeated the same process for the same sample (see **Figure 3.14b**), the emissivity and the temperature remained almost unchanged at about 950 °C. This is because a stable graphite/nickel/diamond structure was formed within 10 secs in the 1st round of heat treatment at about 1000 °C.

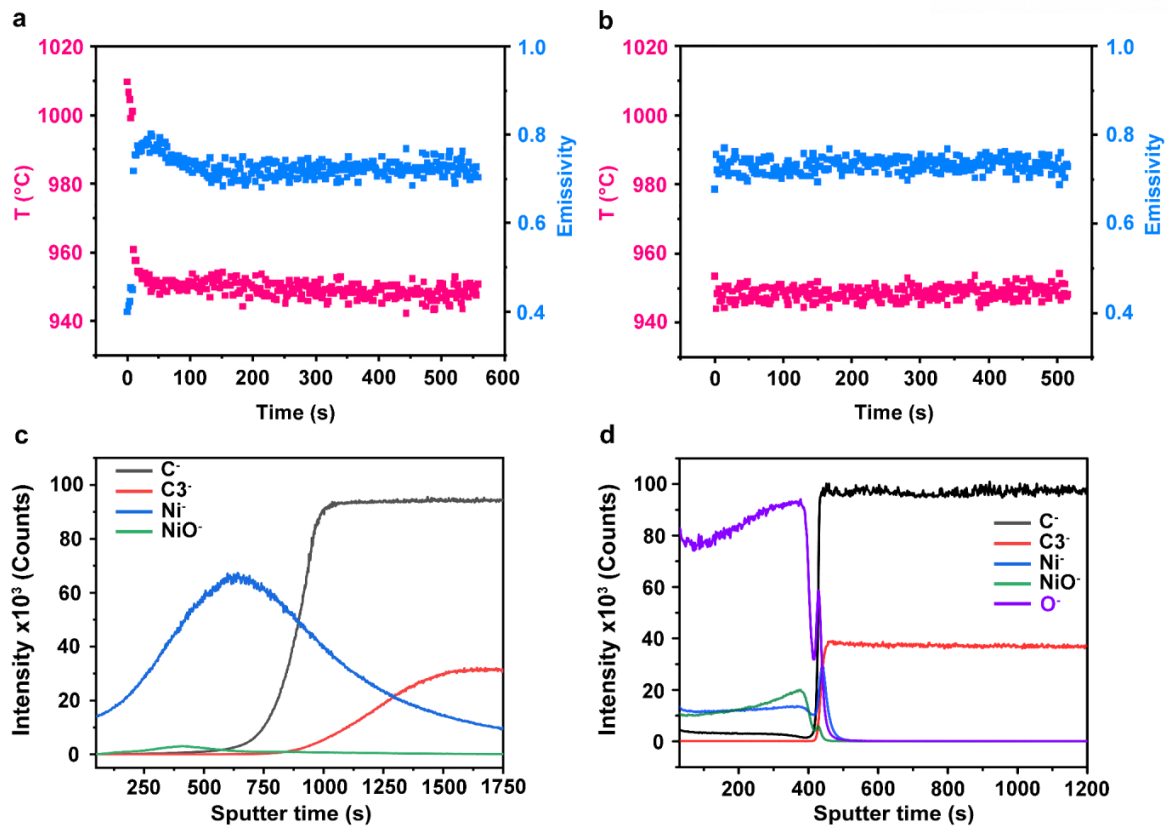


Figure 3.14 (a-b) Spectropyrometer measurements of the emissivity of 500-nm thick Ni coated D(100) sample in the cold wall system and (c-d) time of flight-secondary ion mass spectrometry (ToF-SIMS) depth profiles measured for the Ni /D(100) sample with water vapor present for the conditions used in the continuous diamond dissolution experiments (c) and in the experiments with a fully oxidized metal layer (d).

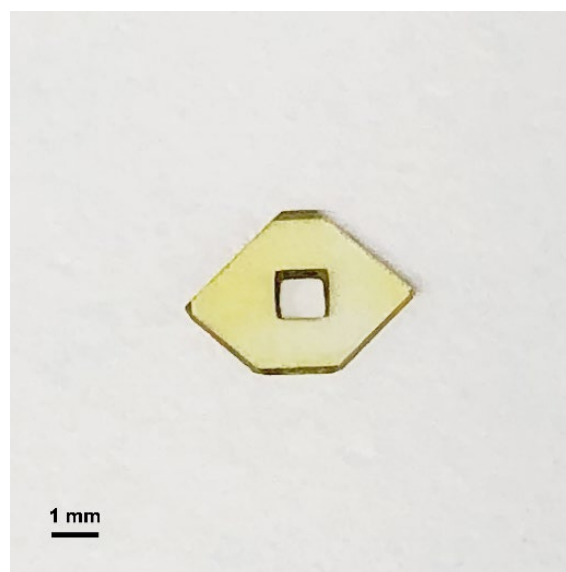


Figure 3.15 An optical microscope (OM) image of a pierced D(100) plate obtained after the dissolution experiment (3 hours at 1050 ± 1 °C, 770 ± 5 Torr pressure, under continuous flow (1000 sccm Ar(g)) of water vapor (bubbler temperature, 25 °C).

Heat treatment at 1050 ± 1 °C in the presence of water vapor (25 °C bubbler temperature) for 3 hours resulted in the complete dissolution of the diamond covered with the Ni film (the Ni film pierced through the 0.3 mm thick diamond). An optical microscope image of the pierced diamond plate is shown in **Figure 3.15**.

Figures 3.14a-b show the results of the spectropyrrometer measurements of the emissivity of the 500-nm thick Ni coated D(100) sample. The time of flight-secondary ion mass spectrometry (ToF-SIMS) depth profiles shown in **Figures 3.14c-d** were obtained for the samples that had been heated from room temperature to 1000 ± 1 °C in 5 mins under continuous flow of 1000 sccm Ar at 770 ± 5 Torr; **Figure 3.14c** shows the depth profiles of the sample heat treated for 10 mins at 1000 ± 1 °C with a continuous flow of water vapor (25 °C bubbler temperature) using Ar (1000 sccm) as a carrier gas; the depth profile measurements of the sample heat treated for 3 hours at 1000 ± 1 °C and 63 °C water bubbler temperature are shown in **Figure 3.14d**.

Depth distribution of C in the metal (Ni, Co) film with and without water vapor. A series of fast heating and fast cooling (quenching) experiments on the 500-nm thick Ni coated D(100) samples with and without water vapor were performed. **Figure 3.14c** shows the ToF-SIMS depth profiles of C, Ni, and NiO for the sample exposed to water vapor. This nickel oxide layer (region) was present at the (sub)surface. It took ~3 seconds to cool from 1000 ± 1 °C to below 500 °C. We chose the fastest possible cooling rate to try to quench the sample and to “freeze” the C distribution inside the metal film. Under these conditions and based on the depth profiles shown in **Figure 3.14c**, the surface region (to the depth of ~50 nm) is oxygen-deficient possibly due to the formation of CO(g) at the metal surface. The ToF-SIMS data also suggest that O is not present at the metal-diamond interface region, indicating that there is pure Ni at the interface. Considering the C^- and C_3^- plots, we suggest that a concentration gradient of dissolved C atoms was formed in the Ni film. **Figure 3.16** shows a ToF-SIMS depth profile of the C distribution for a Co film coated sample exposed to water vapor at the same conditions as the Ni sample. In that sample a concentration gradient of dissolved carbon was also found. **Figure 3.17a** shows the ToF-SIMS data of a Ni-coated diamond sample that was heat treated at 1000 ± 1 °C for 10 mins *without* water vapor in which the minimum intensity of the C^- signal was about $6E+4$ counts (for a sputter time of ~2000 s). Note that no obvious C^- signal was detected in the pristine Ni-coated diamond sample (**Figure 3.17b**). Neither was there any transition from NiO to metallic Ni observed for the sample which had been heat treated with no water present in the chamber.

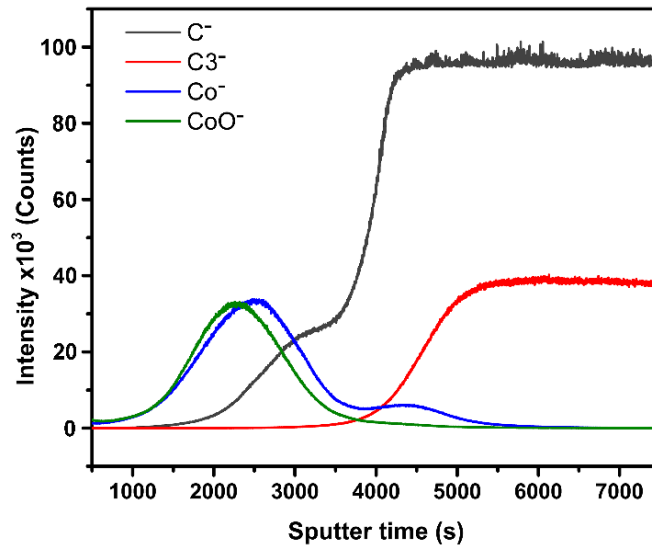


Figure 3.16 Time of flight-secondary ion mass spectrometry (ToF-SIMS) depth profiles of a 500-nm thick Co/D(100) sample after heat treatment at 1000 ± 1 °C for 10 mins with water vapor present in the reaction chamber.

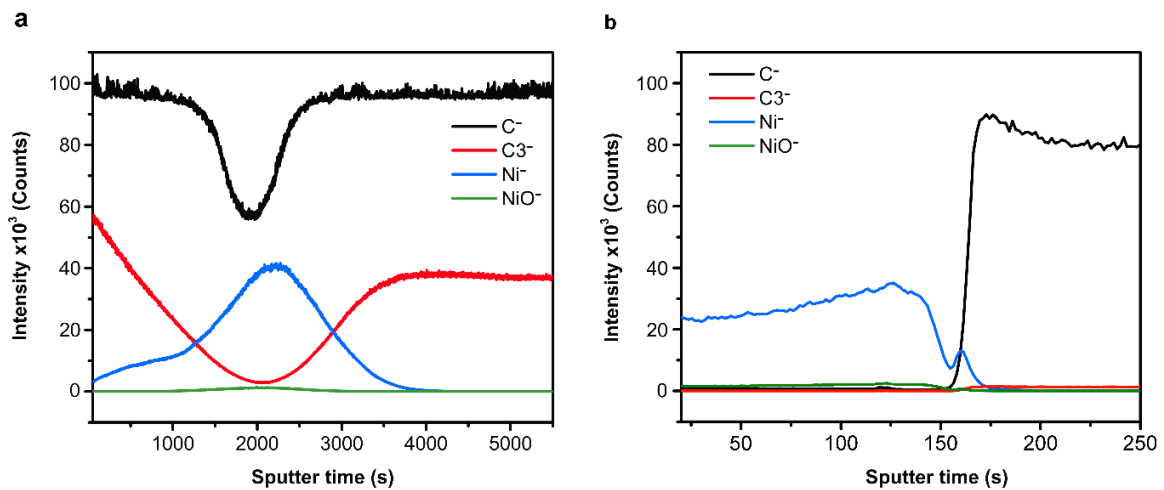


Figure 3.17 Time of flight-secondary ion mass spectrometry (ToF-SIMS) depth profiles of (a) a 500-nm thick Ni/D(100) sample after heat treatment at 1000 ± 1 °C for 10mins without water vapor in the reaction chamber; (b) a pristine 500-nm thick Ni/D(100) sample.

The ToF-SIMS data for a fully oxidized sample are shown in **Figure 3.14d**. O^- and NiO^- signals remained high throughout the Ni film and the C^- and $C3^-$ signals were essentially undetectable, indicating that diamond does not dissolve in the NiO film. **Figure 3.18** shows the SEM images of the

bare diamond surface after removing the NiO film. These images show that on the diamond surface a small amount of carbon was dissolved in the not fully oxidized Ni film at the beginning of the exposure to the water vapor. Yet, even after a 3-hour-long experiment (500 sccm Ar(g); bubbler temperature of 63 °C and a sample temperature of 1000 ± 1 °C), no considerable amount of diamond was dissolved. There was almost no difference in diamond mass before and after this experiment (42.02 mg before and 42.01 mg after) because the Ni film oxidized fairly quickly all the way to the Ni/D interface. In short, too high a concentration of water vapor quickly converts the Ni film to an oxidized one which completely inhibits dissolution of the diamond.

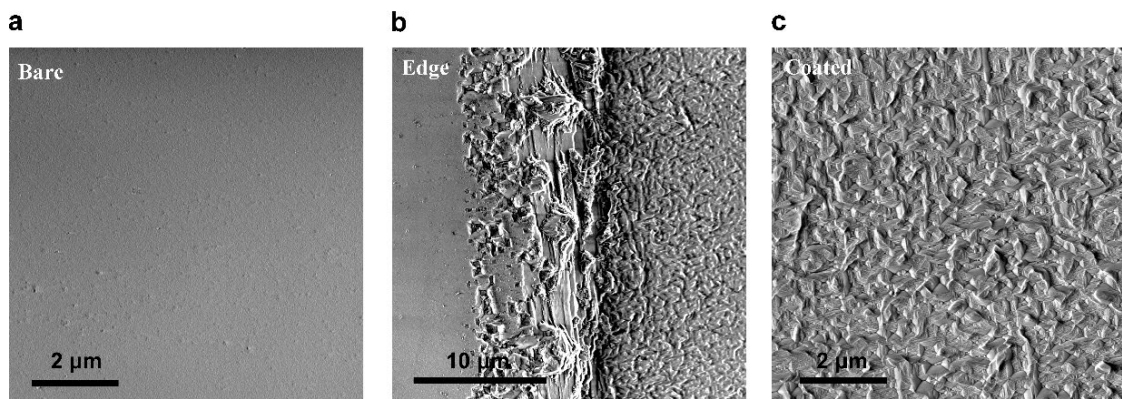


Figure 3.18 SEM images of the diamond surface taken (a) in the bare region (uncoated by Ni), (b) at the edge of the Ni-coated region, and (c) within the Ni-coated region after removing the NiO layer.

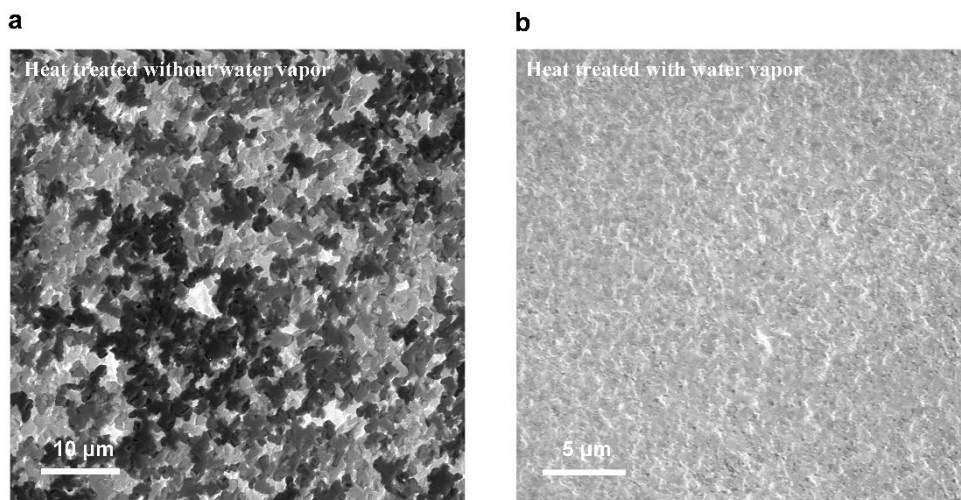


Figure 3.19 SEM images of (a) graphite film formed on the Pt surface after 1000 ± 1 °C heat treatment for 3 hours (770 ± 5 Torr) without water vapor present in the cold wall system reaction chamber; (b) Pt surface after exposure to a continuous flow of Ar(g) and 1000 sccm of water vapor (bubbler temperature, 25 °C) at 1000 ± 1 °C. No graphite was observed.

500-nm thick Pt films sputtered onto the D(100) surface were studied and the results suggest a critical role of an oxide layer on such a sub-surface of the metal film in the process of diamond dissolution, because we observed that the dissolution rates were significantly smaller for the Pt/D(100) samples than for the Ni/D(100) and Co/D(100) samples under the same conditions (a temperature of 1000 ± 1 °C, and similar partial pressures of water vapor in the RSR-M system in different experimental runs), even though the solubility and diffusion rates of C in Pt³¹ are both close to those in Ni³² and Co²⁵. The main difference between Pt and Co/Ni is that a “thick” oxide layer was not formed on or near the Pt surface³³ but was formed for Co and Ni (**Figure 3.19**). The SEM images show that without water vapor a graphitic film formed on the top surface of Pt film which we found could also be removed by water vapor. In a separate 3-hour experiment, a 500-nm thick Pt film was deposited by sputtering on a D(100) sample and the resulting sample was heated at 1000 ± 1 °C in the presence of water vapor (bubbler temperature of 25 °C). No obvious dissolution of the diamond was found. This might be due to the absence of an oxide layer. We note that whether in the quartz tube furnace or the cold wall system, the graphite film could be etched away by water vapor at temperatures in the range studied, as reported by others³⁴, while bare D(100) and D(110) did not etch when exposed to water vapor at around 1000 °C in any of our experiments.

3.2.3 XRD characterization

Synchrotron-based X-ray Diffraction (XRD). We acquired XRD patterns in grazing-incidence mode (GIXD) for one pristine Ni/D(100) sample and two Ni/D(100) samples heated in the quartz tube furnace (See details in the Experimental section). The first was heated at 1000 °C for 1 h without water vapor present, and the second was exposed to a continuous flow of water vapor while heated at 1009 ± 1 °C for 10 mins. The XRD data of the pristine 500-nm thick Ni film on the D(100) surface is shown in **Figure 3.20a**. **Figure 3.20b** shows the GIXD pattern for the sample heated at 1000 °C with no water vapor present, which indicates that there is an increase in the grain (crystalline) size of the Ni film³⁵ based on the spotty diffractions and the decreased peak widths compared with **Figure 3.20a**. The emergence of (002) and (004) graphite diffraction peaks is due to the formation of graphite films³⁵. The diffraction peaks for NiO crystals were identified (**Figure 3.20c**) for the Ni/D(100) sample that was exposed to a continuous flow of water vapor (bubbler temperature 25 °C) at 1009 ± 1 °C (**Figure 3.20c**). Close inspection of **Figure 3.20c** shows that the Ni(200) reflection is mainly found in the “normal direction (q_z -direction)” with significantly reduced angular distribution, which indicates that this crystalline Ni film was predominately oriented to the [100] direction.

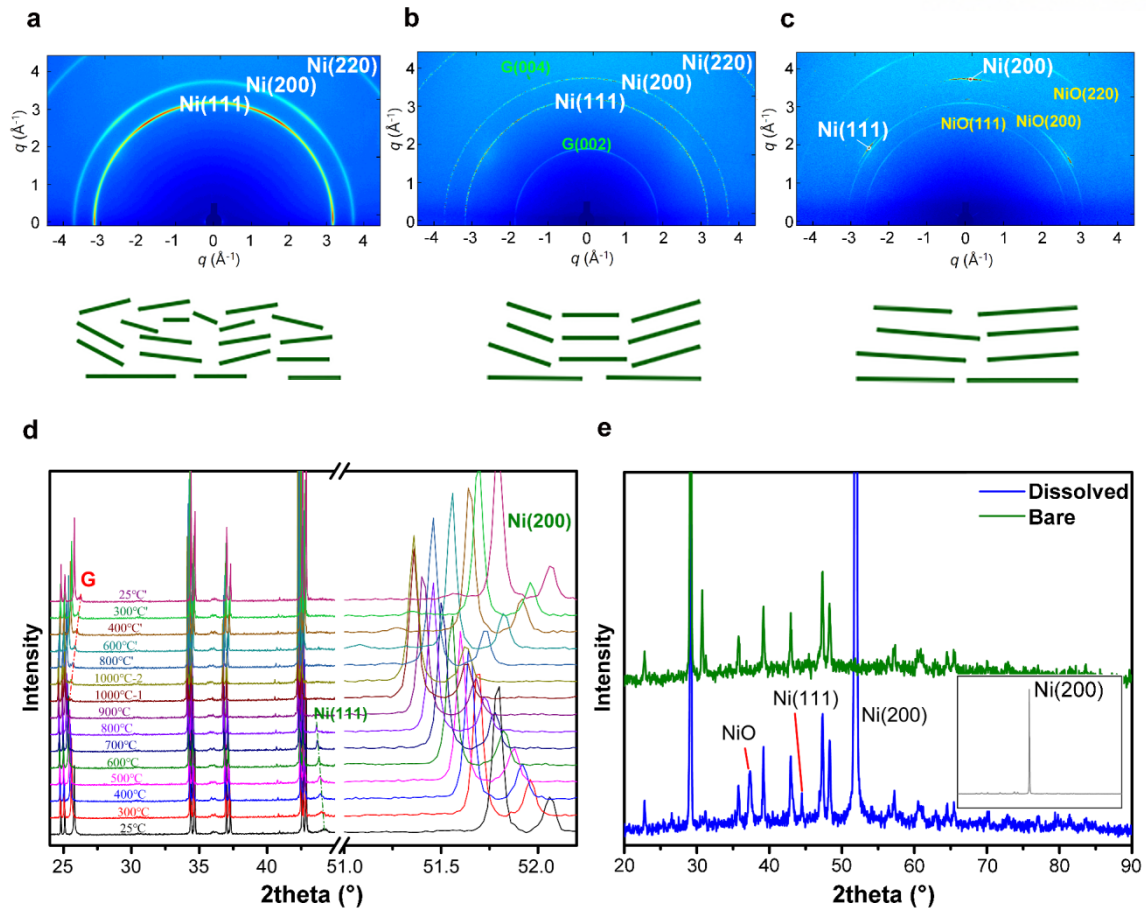


Figure 3.20 Synchrotron-based GIXD patterns of (a) an as-deposited (pristine) Ni film on the D(100) surface, (b) Ni film after heating at 1009 ± 1 °C for 1 h without water vapor and (c) Ni oxide/Ni film on the D(100) surface obtained after heating at 1009 ± 1 °C for 10 min with water vapor (bubbler temperature 25 °C). (d) *In-situ* XRD study of a 500-nm thick Ni film on the D(100) surface. (e) Powder XRD (P-XRD) patterns of bare single crystal diamond with a (100) surface (upper curve) and nickel coated diamond heated at 1009 ± 1 °C for 10 min with water vapor present (bubbler temperature 25 °C) contributing to the dissolution of diamond into the Ni film (lower curve).

Ni/Co-D(100) variable temperature *in-situ* XRD. The results of variable temperature *in-situ* XRD measurements conducted under a helium atmosphere at about 75 Torr with no water vapor present (see details in the Experimental section) are shown in **Figure 3.20d** for the Ni/D(100) sample. It can be seen that a nickel carbide³⁶ (Ni_3C) phase was apparently not present in the Ni/D system during the entire heating and cooling process. Ni_3C is reported to decompose at about 350 °C³⁷ into Ni and graphite. The XRD patterns show that a graphitic film with the (002) orientation was formed at 1000 °C, and that the Ni(111) peak disappeared at 900 °C during the heating stage, but the Ni(200) peak was still observed during the whole measurement process due to its epitaxial relation with the diamond substrate. This

result shows that the preferred orientation of Ni crystals is evolved over 900 °C, as the conventional reflection-mode XRD measurement only provides out-of-plane information of the sample. **Figure 3.20e** shows a P-XRD pattern of the Ni film for Ni/D(100) after a diamond dissolution experiment with water vapor present in the quartz tube furnace, and also a pattern of the bare single crystal diamond 100 substrate used in our study. We found that after heating at 1009 ± 1 °C, the deposited polycrystalline Ni film on D(100) substrate converted primarily to a Ni(100) film (inset of **Figure 3.20e**). Besides, the variable temperature *in-situ* XRD measurement for a 500-nm thick Co film on the D(100) surface are shown in **Figure 3.21a**. This film was converted to FCC-Co(100) during the heat treatment. No peaks corresponding to the cobalt carbide (Co_3C) phase were found in the XRD pattern of the Co-coated D(100) sample heat treated without water vapor. Heat treatment of a polycrystalline Co film on the D(100) surface at ~ 1000 °C in the absence of water vapor resulted in a Co(100) film with single crystalline features after returning the sample to room temperature.

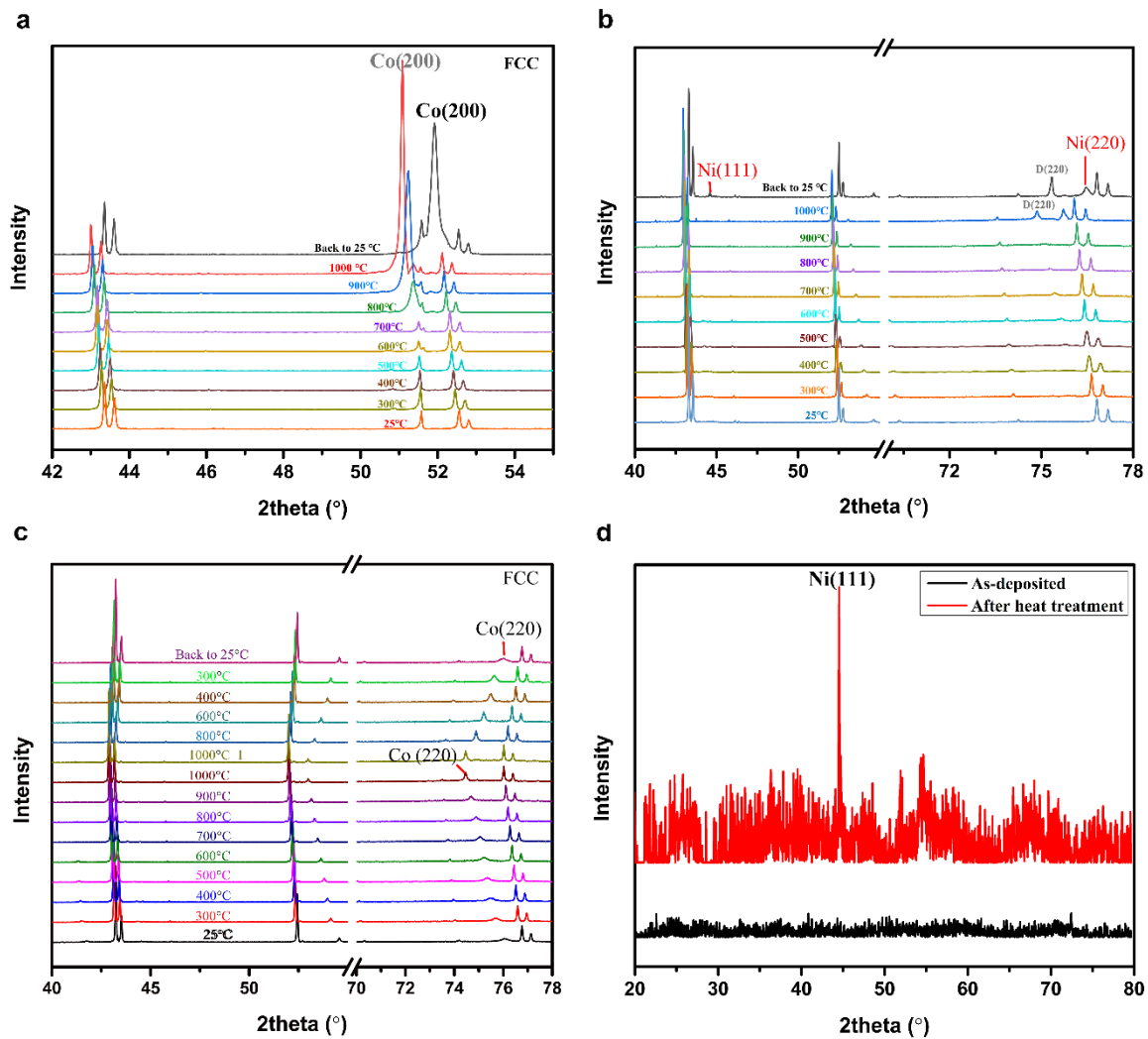


Figure 3.21 Variable temperature *in-situ* XRD analyses of (a) 500-nm thick Co film on the D(100) surface, (b) 500-nm thick Ni film and (c) Co film on the D(110) surface. (d) P-XRD measurements of 500-nm thick Ni film on the D(111) surface. Note that the peak intensity is weak since the 1 mm x 1 mm area of the Ni film region on the D(111) surface is small.

Ni/Co-D(110) variable temperature *in-situ* XRD. The same characterization on D(110) substrates are shown in **Figures 3.21b-c**, and the XRD patterns suggest that the Ni and Co films were converted to fcc films with single crystalline features and a (110) surface after heating and cooling to room temperature. For a 500-nm thick Ni film coated on D(111) substrate heated at 1009 °C for 1 hour in the absence of water vapor in the quartz tube furnace the film was converted to a Ni(111) film with single crystalline features according to the XRD data shown in **Figure 3.21d**.

It is not possible to introduce water vapor into our variable temperature *in-situ* XRD instrument, and so we did P-XRD measurements on the samples (Ni/Co on D(100), D(110)) after the dissolution experiments. **Figure 3.22** shows the XRD patterns for these samples, in which we found that the fcc-M(200) peak is the main peak for the D(100) samples and fcc-M(220) is the main peak for the D(110) samples, for both Ni and Co.

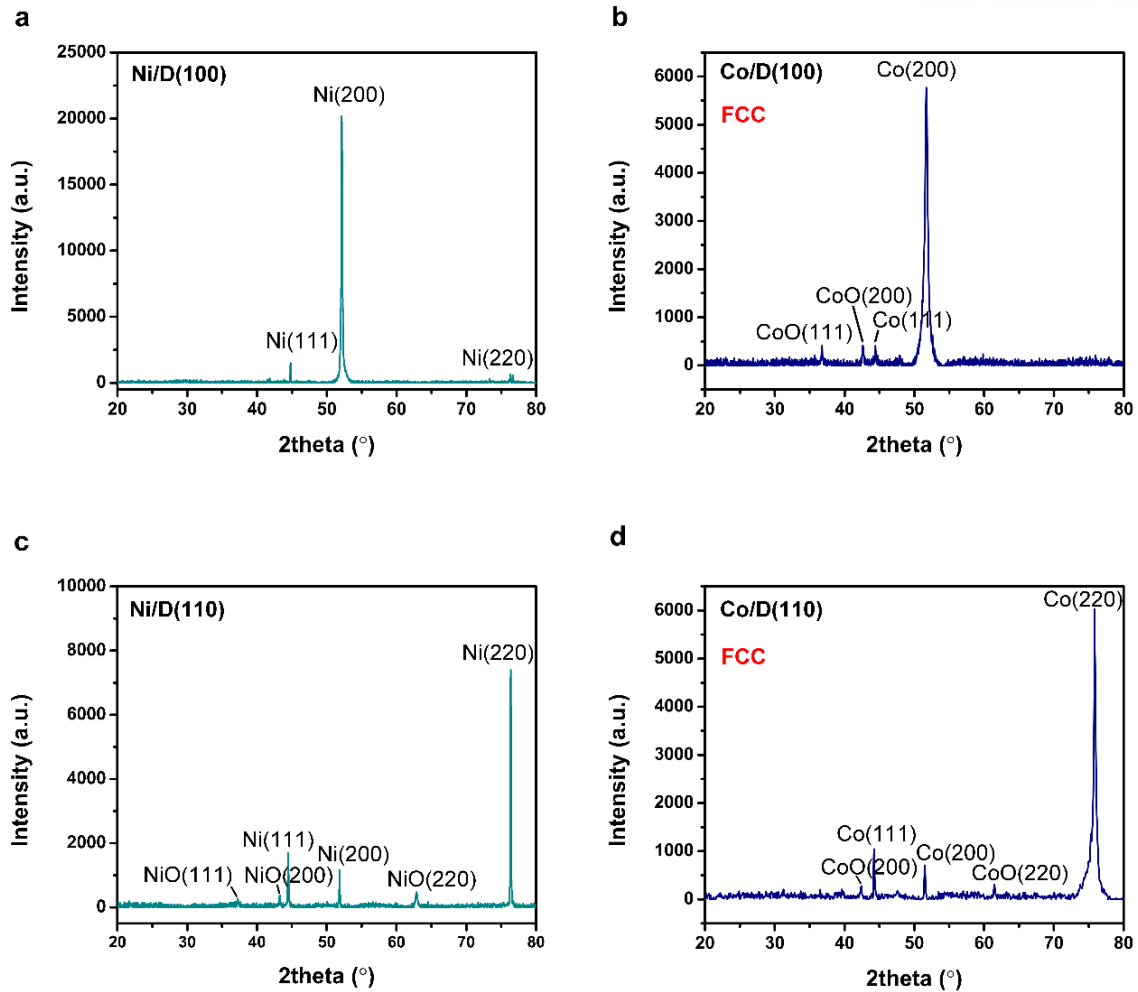


Figure 3.22 P-XRD analysis of 500-nm thick Ni/Co film on (a-b) D(100) substrates and (c-d) D(110) substrates after dissolution experiments. We suggest that only fcc-Co exists (not hcp) in the Co/D(100) and Co/D(110) samples because the XRD pattern for Co/D(100) (b) is comparable to the fcc-Ni/D(100) XRD pattern (a), and the XRD pattern for Co/D(110) (d) is comparable to the fcc-Ni/D(110) XRD pattern (c), and also that the CoO peaks shown in (b), (d) are in agreement with the fcc-CoO phases but not the hcp-CoO phases. In other words, and possibly due to the influence of the diamond substrates, the fcc-Co film does *not* convert to hcp after cooling to room temperature.

The results described above mean that the Ni and Co films likely have an epitaxial interface with the single crystal diamond substrates with 100 and 110 orientations and that the as deposited films are converted to films with single crystalline features with the same surface orientation as the diamond. For Ni films deposited on 111 single crystal diamond plates that we have briefly studied, the Ni film is

apparently converted to a film with 111 orientation and with single crystalline features, perhaps epitaxial to the diamond. We have not yet tested Co.

3.2.4 Theoretical modeling of reaction pathways and potential energy barriers.

We have done a variety of density functional theory (DFT) calculations relevant to these thin metal films deposited on diamond and heated in the presence or absence of water vapor. The potential energy barriers of (i) the oxidation reaction at the open metal surfaces and (ii) of the carbon “dissolving” at the metal-diamond interfaces, were calculated at ~ 1273 K and are shown in **Figure 3.23** (See details in the Experimental section). We used $Fm\bar{3}m$ Ni(100) [Ni(110)] or Co(100) [Co(110)] configurations on the D(100)[D(110)] surfaces in our modeling because the experiments suggested that the films are either completely or mostly epitaxial to the single crystal diamond substrates.

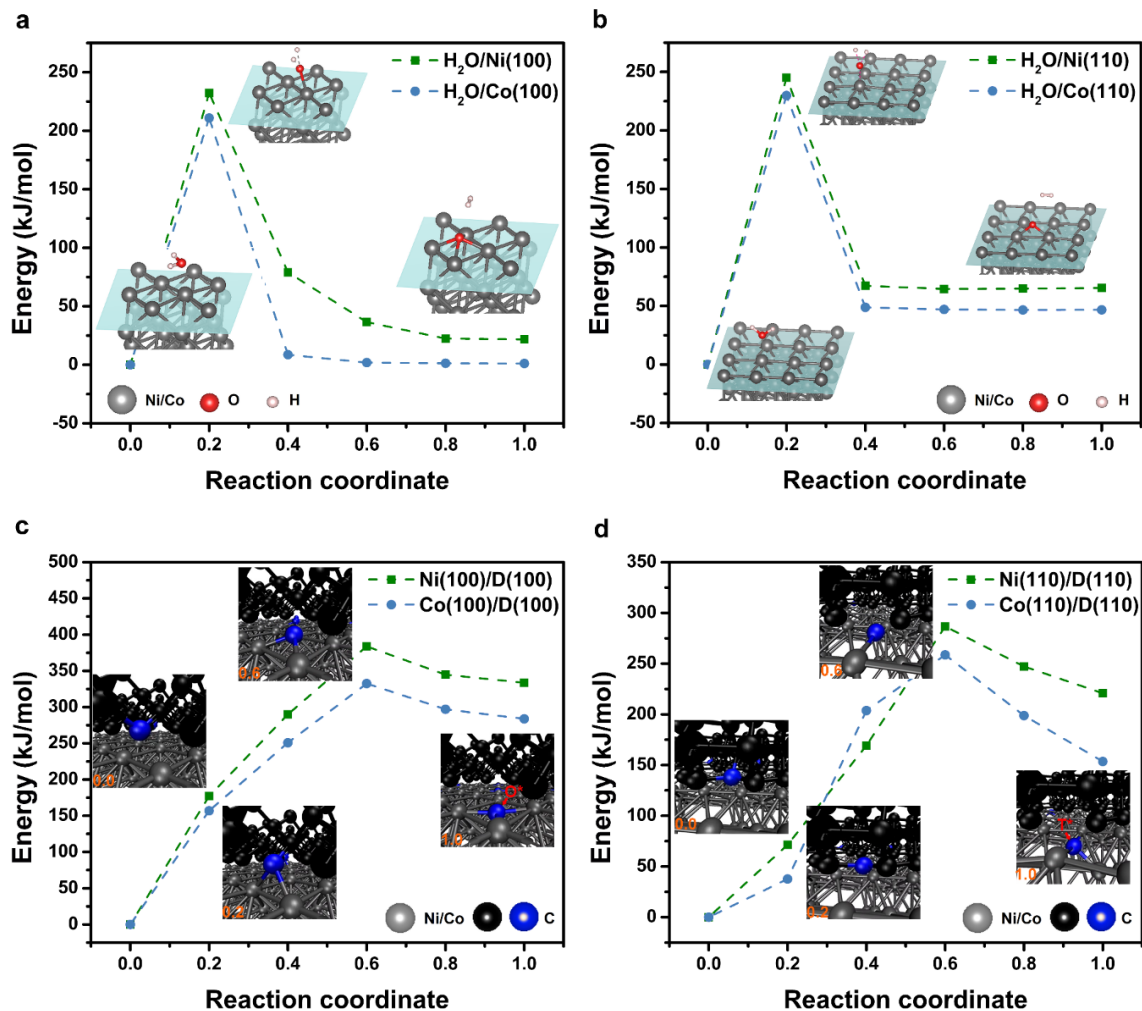


Figure 3.23 (a-b) Potential energy curves calculated for (a) a H₂O molecule reacting with Ni(100) (green) or Co(100) (blue), and (b) for C-C bond breaking at the Ni(100)/D(100) (green) or

Co(100)/D(100) (blue) interfaces. The corresponding atomic structures of the initial, intermediate, and final configurations are shown as insets. (c-d) Potential energy curves calculated for a C atom diffusing from (c) the Ni(100)/D(100) interface (green) through the octahedral site (O*) or (d) the Co(110)/D(110) interface (blue) through the tetrahedral site (T*). The corresponding atomic structures of the initial, intermediate, and final configurations are shown as insets.

Surface reactions (Regime I). **Figure 3.23a** shows the potential energy curves calculated for the surface reaction of a H₂O molecule at the Ni(100) and Co(100) surfaces (See details of the DFT modeling in **Figure 3.24**). A H₂O molecule adsorbs with a binding energy of -0.745 eV on Ni(100) and -0.270 eV on Co(100) and then dissociates into a hydrogen molecule and a chemisorbed oxygen atom. The calculated ΔH^\ddagger for this dissociation is 232 kJ/mol on the Ni(100) surface and 211 kJ/mol on the Co(100) surface. Our experimental values with water bubbler temperatures in parentheses on D(100) substrates are: Ni: 236±6 kJ/mol (0 °C), 240±5 kJ/mol (25 °C); Co: 201±5 kJ/mol (0 °C), 228±4 kJ/mol (25 °C), for Regime I. The C atoms that diffuse through the metal layer react with the surface –Ni-O species to form –Ni-C-O, which decomposes to release CO into the gas phase. The potential energy curves describing the formation of the –Ni-C-O configuration on the Ni(100) surface and decomposition to release CO into the gas phase are given in **Figure 3.25**. The same simulations for the formation of –Co-C-O and decomposition to release CO into the gas phase are shown in **Figure 3.26**. For both, the energy barriers are primarily lower than the formation barrier of –Ni-O (232 kJ/mol) and –Co-O species (211 kJ/mol) on each fcc-M(100) surface.

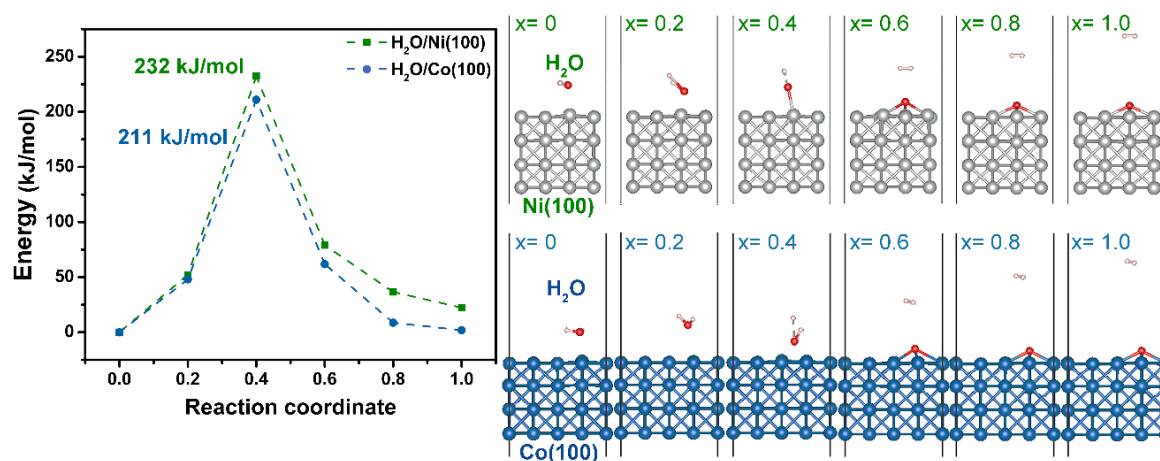


Figure 3.24 (left) Potential energy curves for a H₂O molecule reacting with the Ni(100) or Co(100) surfaces; (right) atomic structures of the initial physisorbed molecule (x= 0.0), the transition state (x= 0.4) and other intermediate configurations.

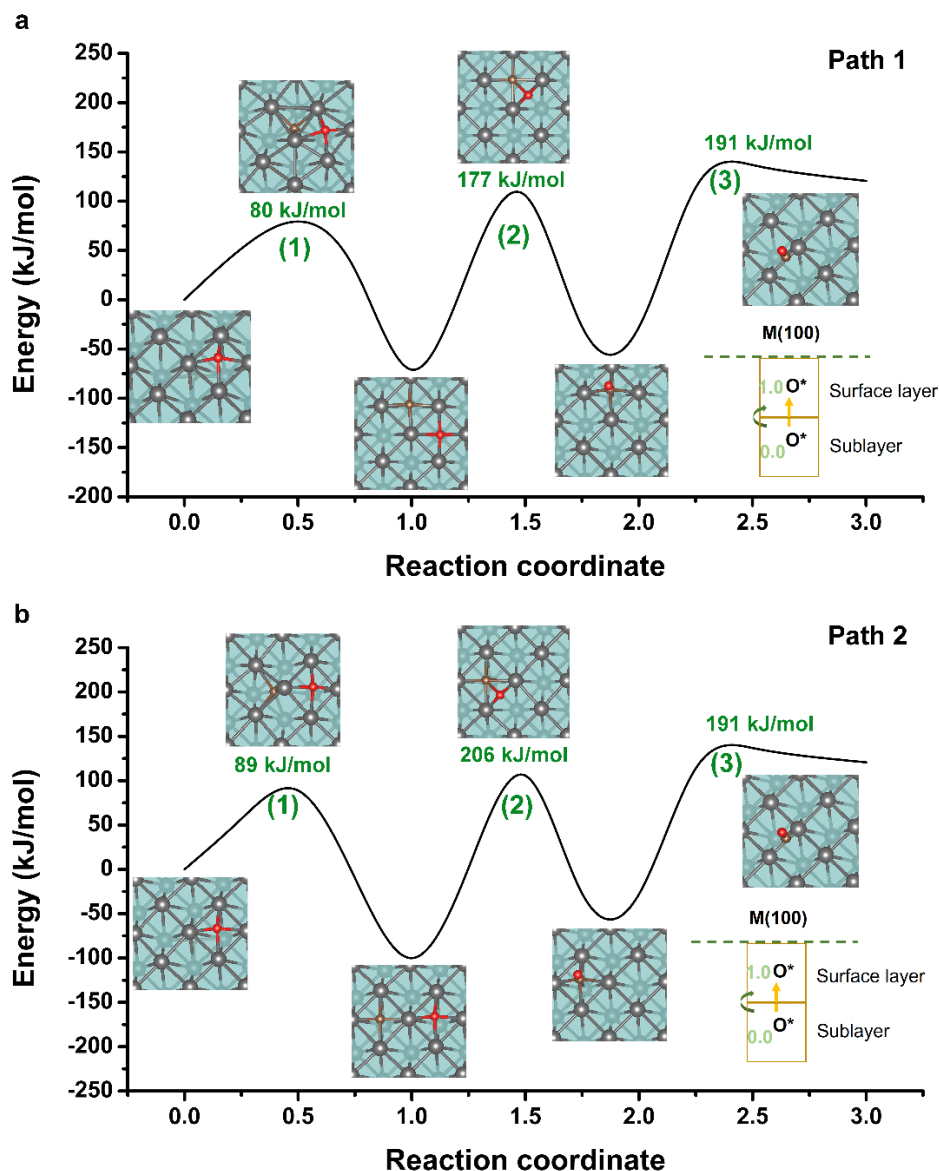


Figure 3.25 Potential energy curve for the surface reaction on Ni(100). (a) Potential energy curve for C atom migration from an octahedral (O^*) site at the subsurface to an O^* site at the surface, as shown in the inserted schematic image, which shows the reaction process from $x=0.0$ to 1.0 (1). The O atom migrates from the original O^* site to the O^* site that the C atom had occupied yielding formation of -Ni-C-O (2), followed by release of one CO into the atmosphere (3). (b) Potential energy curve for C atom migration from an O^* site at the subsurface to an O^* site at the surface, as shown in the inserted schematic diagram, which shows the reaction process from $x=0.0$ to 1.0 (1). The O atom migrates from the original O^* site to an O^* site that the C atom had occupied forming -Ni-C-O (2), followed by release of one CO into the atmosphere (3). Note that there are two possible paths for the migration of the O

atom at the metal surface because there are two inequivalent half-octahedral sites that the C atom occupied relative to the position of the O atom at the surface. We calculated the two paths and provide the potential energy curve for both. The energy barriers at each step for these two paths are lower than the energy barrier of the surface reaction between a Ni atom and a H₂O molecule.

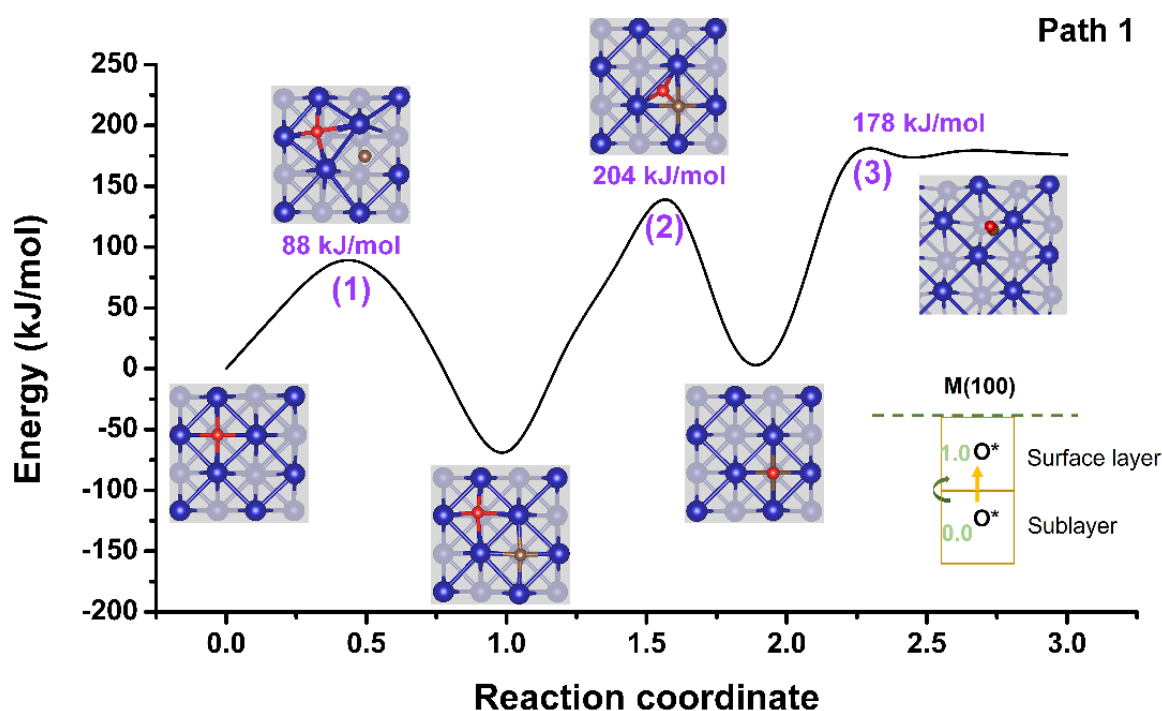


Figure 3.26 Potential energy curve for the surface reaction on Co(100). Potential energy curve for one C atom migration from an octahedral site (O*) at the subsurface to an O* site at the surface, as shown in the inserted schematic, which shows the reaction process from $x=0.0$ to 1.0 (1). The oxygen atom migrates from the original O* site to the O* site that the C atom had occupied and forms the -Co-C-O state (2), and the -Co-C-O state decomposes and releases a CO(g) molecule into the atmosphere (3). The path calculated is the same as that calculated in **Figure 3.25a**, which has a lower energy barrier in steps (1) and (2) compared with the energy barrier for steps (1) and (2) in **Figure 3.25b**. The energy barriers at each step for this path are lower than the energy barrier of the surface reaction between a Co atom and a H₂O molecule.

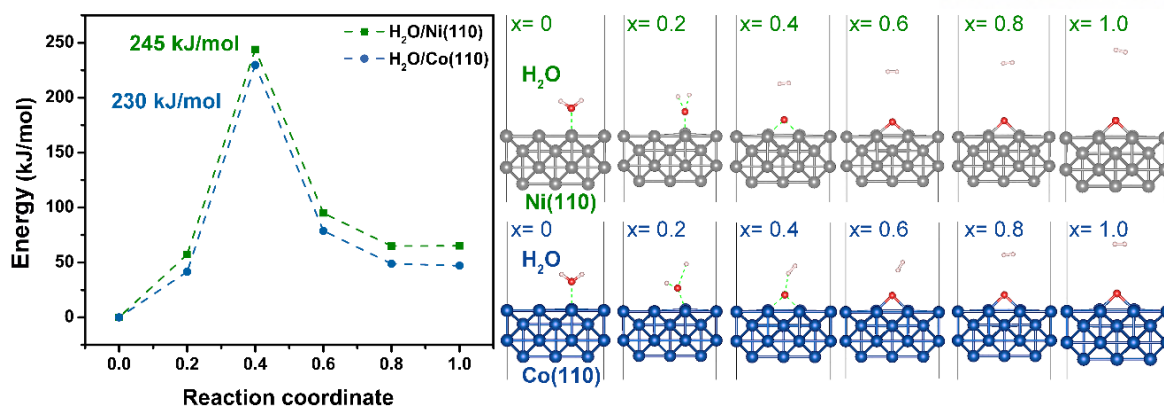


Figure 3.27 (left) Potential energy curves for a H₂O molecule reacting with the Ni(110) or Co(110) surface; (right) atomic structures of the initial physisorbed ($x=0.0$) state, the transition state ($x=0.4$) and other intermediate configurations.

The same simulation was conducted for the Ni(110) and Co(110) surfaces (see details of the DFT modeling in **Figure 3.27**), as shown in **Figure 3.23b**. A H₂O molecule adsorbs with a binding energy of -0.405 eV on the Ni(110) and -0.391 eV on the Co(110) surfaces. The calculated ΔH^\ddagger for its dissociation is 245 kJ/mol on the Ni(110) surface and 230 kJ/mol on the Co(110) surface. Our experimental values (water bubbler temperatures in parentheses) on D(110) substrates: Ni: 214 ± 4 kJ/mol (25 °C); Co: 221 ± 4 kJ/mol (25 °C) for Regime I. The energy barrier values describing the formation of $-M-O$ species, the formation of $-M-C-O$ state on the M(110) surface and the decomposition to release CO into the gas phase are provided in **Figure 3.28**. According to our modeling, the energy barriers for the formation of $-Ni-O$ species on Ni(110) and $-Co-O$ species on Co(110) in Regime I are 245 kJ/mol and 230 kJ/mol, respectively. These compare reasonably well with the experimental values. **Table 3.10** shows the energy barriers at each step for the M(100) and M(110) cases.

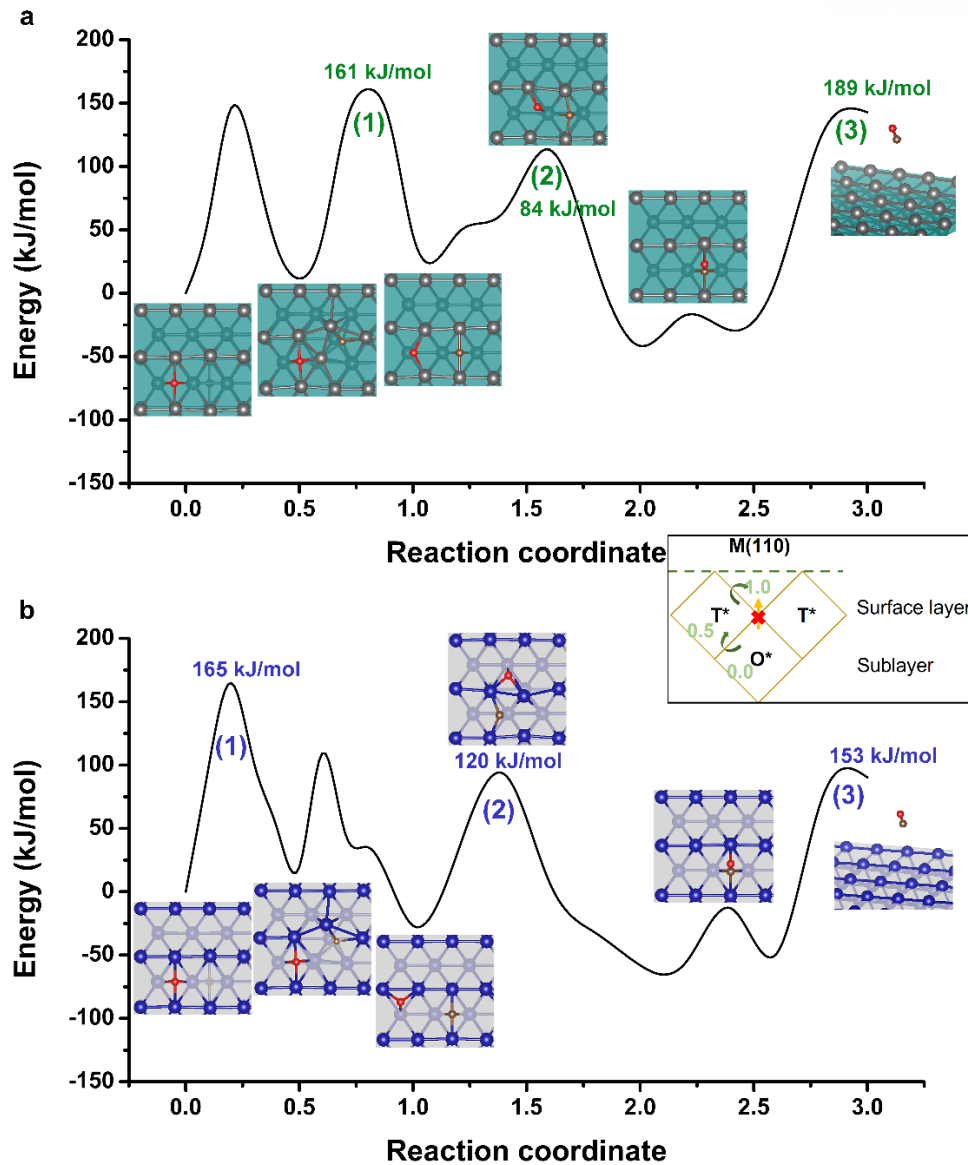


Figure 3.28 Potential energy curve for the surface reaction on (a) Ni(110) and (b) Co(110). One C atom jumps from an octahedral (O*) site at the subsurface to a tetrahedral (T*) site, then to the surface, as shown in the inserted schematic; from $x=0.0$ to 1.0 (1), the O atom migrates from the original O* site to the T* site that the C atom occupied and forms -M-C-O (2), and the -M-C-O then releases a CO molecule into the atmosphere (3). Thus: From $x=0.0$ to 1.0 the indicated C atom moves to the surface, from $x=1.0$ to 2.0 a surface O atom and that same surface C atom migrate and react, and from $x=2.0$ to 3.0 CO desorbs. The appearance of a C atom on the M(110) surface thus occurs in two steps, as shown in the inserted schematic: from $x=0.0$ to 0.5, a C atom in the sublayer moves to a T* site just below the open surface, and from $x=0.5$ to 1.0, this C atom moves from the T* site to the open surface. For Ni(110), this diffusion from subsurface to the surface has the highest energy barrier (161 kJ/mol)

when the C atom migrates to the open surface. For Co(110) the highest energy barrier (165 kJ/mol) is for the C atom passing through the T* site.

Table 3.10 Energy barrier values describing the formation of –Ni-C-O or -Co-C-O states on Ni/Co(100) and Ni/Co(110) surfaces and the decomposition to release CO into the gas phase.

Model	$\text{H}_2\text{O}_{(\text{g})} + * \rightarrow \text{O}^* + \text{H}_{2(\text{g})}$	C segregation	$\text{C}^* + \text{O}^* \rightarrow * \text{CO}$	$* \text{CO} \rightarrow * + \text{CO}_{(\text{g})}$
Ni (100)	232	80, 89	177, 206	191
Co(100)	211	88	204	178
Ni(110)	245	161	84	189
Co(110)	230	165	120	153

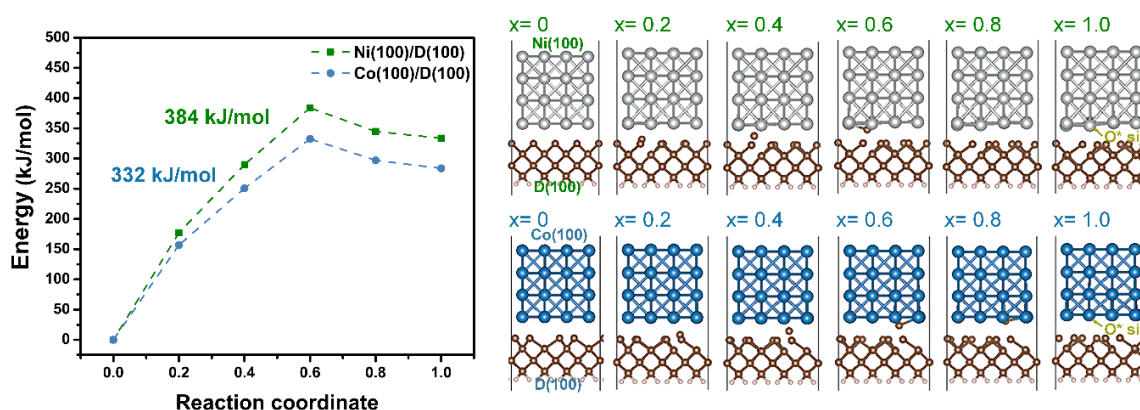


Figure 3.29 (left) Potential energy curves for C atom diffusion at the Ni(100)/D(100) (green curve) and Co(100)/D(100) (blue curve) interfaces; (right) atomic structures of the initial ($x= 0.0$), intermediate, and final ($x= 1.0$) configurations.

Interface reactions (Regime II). With respect to the M-D(100) interface, the binding energy (-2.90 eV/C atom for Ni(100)-D(100) and -3.27 eV/C atom for Co(100)-D(100)) stabilizes the sp^3 -bonded C atoms at the D(100) surface located at bridge positions relative to the atomic arrangement of the metal surfaces (Ni(100) or Co(100)). The increases in energy up to the transition state are caused by (i) lateral movement that breaks one C-C bond, and then (ii) migration perpendicular to the surface with breaking of another C-C bond. These two C atoms then move to the octahedral interfacial sites in the fcc metal structure (See **Figure 3.29** for details). The potential energy curves of carbon atom diffusion at the Ni(100) or Co(100)/ D(100) interface through the octahedral sites are shown in **Figure 3.23c**. The ΔH^\ddagger

for this process was calculated to be 384 kJ/mol for the Ni(100)-D(100) interface and 332 kJ/mol for the Co(100)-D(100) interface. These values can be compared with the experimental values of 351 ± 7 kJ/mol (Ni/D(100)) and 353 ± 5 kJ/mol (Co/D(100)) (water bubbler temperature 43 °C (Regime II)) discussed above.

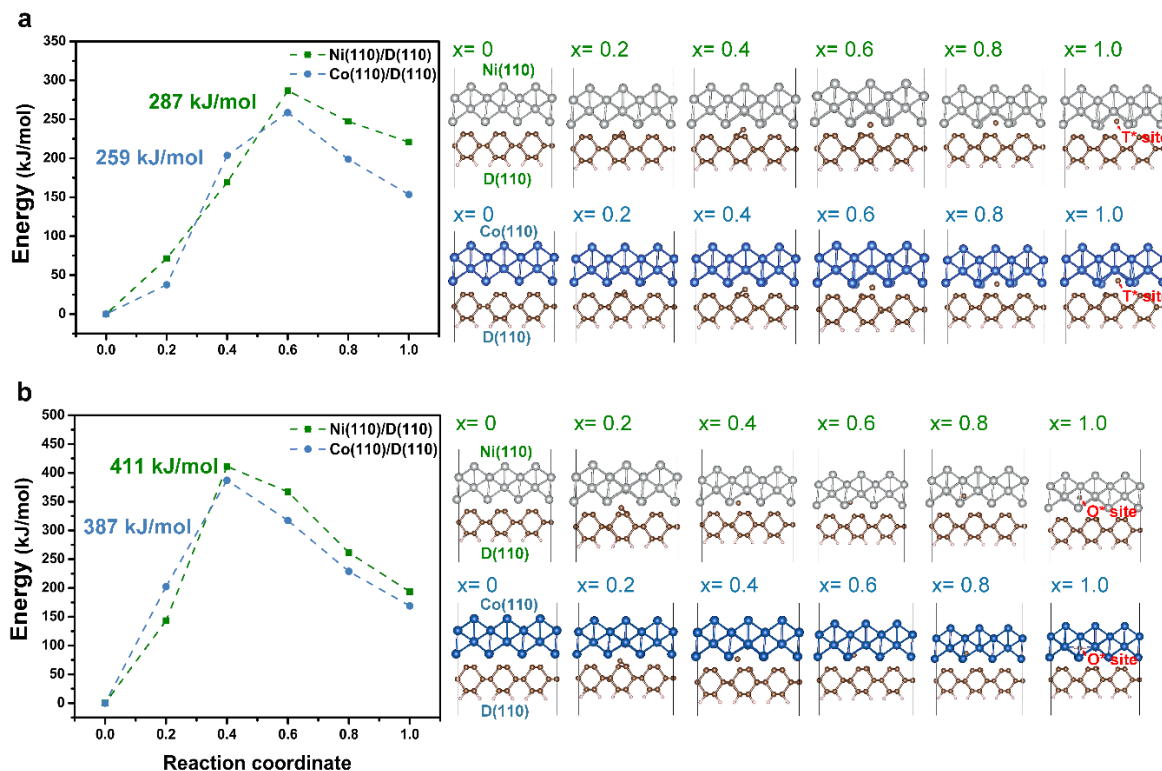


Figure 3.30 (left) Potential energy curves for C atom diffusion at the Ni(110)/D(110) (green curve) and Co(110)/D(110) (blue curve) interfaces through the (a) *tetrahedral* and (b) *octahedral* interfacial sites; (right) atomic structures of the initial ($x=0.0$), intermediate ($x=0.2, 0.4, 0.6$, and 0.8), and final ($x=1.0$) configurations.

For the M-D(110) interface, In the diamond dissolution process the permeation of C through the metal film starts with the dissociation of the C-C bonds at the metal-diamond interface. The C-C bonds at the M-D(110) interface preferentially release C atoms into the *half-tetrahedral* interfacial sites of the fcc metal structures (See **Figure 3.30a** for details) instead of the octahedral sites (**Figure 3.30b**). The potential energy curves for carbon atom diffusion at the Ni(110) or Co(110)/ D(110) interface are shown in **Figure 3.22d**. The ΔH^\ddagger for this process was calculated to be 287 kJ/mol for the Ni(110)-D(110) interface and 259 kJ/mol for the Co(110)-D(110) interface. These values can be compared with the respective experimental values of 270 ± 5 kJ/mol (Ni/D(110)) and 266 ± 3 kJ/mol (Co/D(110)) (water bubbler temperature 43 °C (Regime II)), discussed above.

The calculated activation barriers for carbon diffusion in bulk Ni (175 kJ/mol) or Co (153 kJ/mol) (Figure 3.31) are much lower than the rate limiting activation enthalpy of the surface (Regime I), and the interface (Regime II) processes; these calculated values are in a good agreement with the reported experimental values of 137 kJ/mol (873–1673 K) for Ni and 154 kJ/mol (976 K-1673 K) for Co.^{23,24}

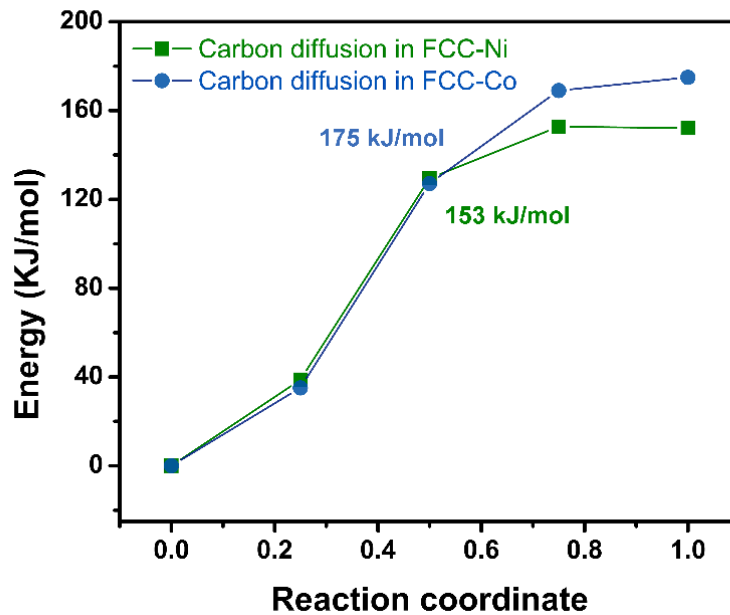


Figure 3.31 Potential energy curves of carbon diffusion barriers in fcc-Ni and fcc-Co. The C atom diffuses from an octahedral site to a tetrahedral site, then back to the octahedral site ($O^* \rightarrow T^* \rightarrow O^*$). We show the C atom diffusion energy barrier from the O^* site to T^* site only, due to symmetry.

Considering the FCC Co and Ni films in our study, there are 4 octahedral interstitial sites per Ni, and per Co atom. 12 nearest neighbor octahedral sites are there for a given octahedral site. In a 500 nm thick 2 x 2 cm Ni/Co film we prepared by the sputter deposition, there are roughly $1.72E17$ octahedral sites for Ni film and $1.67E17$ octahedral sites for Co film. On the other hand, in ideal conditions, based on the highest rates of dissolution of Ni, and separately Co, a typical jump times for a C atom to make from one octahedral site to another one, to allow that C atom that came from the D/M interface, to traverse through the film, and thus to be eliminated as CO and/or CO₂ at the top of the film, are $1.5E-6$ s and $4.9E-7$ s for Ni, Co films, respectively (we only considered the unoccupied octahedral site case).

3.3 Conclusion

We have studied the dissolution of single crystal diamond (100) and diamond (110) in 500-nm thick Ni and Co films with water vapor present and absent in the reaction chamber.

Without water vapor thin graphitic films are formed at the metal surface and also at the metal/diamond interface during the heat treatment at temperatures around 1000 °C. Graphitic films were observed to be formed at temperatures as low as about 650 °C for Ni/D(100).

With water vapor present, a two-regime (Regime I and Regime II) mechanism of diamond dissolution was discovered. In Regime I (lower partial pressure of H₂O(g)), the rate limiting step was the removal of the C that diffused through the metal film to the free surface, and in Regime II (higher partial pressure of H₂O(g)) the rate limiting step was dissolution of the diamond at the diamond/metal interface. A concentration gradient of C in the metal films was found by ToF-SIMS depth profiling, with a high concentration at the metal-diamond interface and a low concentration at the free surface. The rate of dissolution of diamond into either Ni or Co films is constant with time for a given vapor pressure of water and at a given temperature. The experimental and theoretical (DFT calculated) values for the activation enthalpies of the relevant reactions at the metal surface, and at the metal-diamond interface, and for the diffusion of C through each metal are in a relatively close agreement.

This work is a comprehensive study of the kinetics of water vapor induced dissolution of single crystal 100 and 110 diamond into nickel and cobalt films. The data and modeling provide inspiration to those in industry who can consider this method of removing diamond as an alternative to polishing with mechanical abrasives. Knowing the kinetics and thus being able to also model the dissolution rates can open new opportunities for “pre-shaping” single crystal diamond in ways that can replace or augment other methods such as RIE, molding and laser patterning in order to achieve micro-fabrication with low-cost, high efficiency and in a highly controllable including for novel 3D structures such as quantum devices,³⁸ MEMS,³⁹ and power devices⁴⁰ and without “plasma damage” that occurs by RIE methods.⁴¹ This study also demonstrates the possibility of tuning the dissolution of diamond via rational control of the thermochemical parameters at the free surface and the metal/diamond interface.

3.4 Experimental section

3.4.1 Materials and chemicals

HPHT Ila-type single crystal diamond plates (Infi advanced materials Co., Ltd., China); 99.99% Ni target and 99.95% Co DC-sputter targets (ITASCO, South Korea); 30% Hydrogen peroxide (H₂O₂) (CAS: No.7722-84-1, Daejung chem, South Korea); 98% Sulfuric acid (H₂SO₄) (CAS: No.7664-93-9, Daejung chem, South Korea); 37% hydrochloric acid (HCl) (CAS: 7647-01-0, Daejung chem, South Korea).

3.4.2 Detailed methods

Variable temperature in-situ XRD: The metal (Ni, Co) film-coated single crystal diamond samples were placed on the heating stage in an XRD system (Smart lab XE, Cu target, 45kV, 200mA), which was encapsulated in a chamber protected by helium gas maintained at ~75 Torr. We note that the sample was fixed on the holder with the high temperature carbon paste, which produced some XRD peaks during our measurements. The heating/cooling rate was ~16 °C/min. The highest temperature we used was close to 1000 °C and was measured with a thermocouple attached to the exterior of a small capsule containing the sample. It is expected that the sample temperature is quite close to the capsule temperature. The XRD patterns were acquired for the angular range 20° - 80° with 0.02° steps.

Residual gas analyzer (RGA) measurements in CVD furnace: To elucidate the surface reaction and to detect its gaseous products, we conducted *in-situ* residual gas analysis using a two-chamber CVD-RGA (residual gas analyzer) experimental setup. Five 500-nm thick nickel coated diamond plates were placed inside the 1/2-inch quartz tube upstream of the hot zone, which was heated to 1050 °C (furnace temperature) for 1 hour and kept at this temperature during the experiment. Once all the conditions (1050 °C temperature of the hot zone, 760±1 Torr pressure, 43 °C temperature of the bubbler, a continuous water vapor flow) used in the diamond dissolution experiments were set and a stable background RGA signal was established, the Ni-coated diamond samples were transferred from the cold zone into the hot zone. The RGA measurements were conducted using a differential pumping technique when the pressure in the reaction chamber was 760±1 Torr while the pressure in the RGA chamber was maintained at ~9E-6 Torr. A metering valve was used to leak gases from the reaction chamber into the RGA chamber. In order to obtain the background signal, we did test CVD-RGA experiments without diamond samples in the hot zone of the 1/2-inch inner tube.

Spectroscopy measurement on the cold wall system: To determine the emissivity of the nickel-coated diamond sample, we conducted spectroscopy measurements. A 500-nm thick Ni film on a D(100) plate was placed on the graphite holder in the cold wall system. The spectroscopy laser spot (2mm diameter) was focused on the Ni film surface. The temperature was increased from room temperature to ~1000 °C in 10 seconds in an argon atmosphere at 770±5 Torr pressure. We collected the signal from the surface during the heat treatment. Heating/cooling were controlled by a programmable temperature controller combined with another pyrometer and a power supply unit.

Synchrotron X-ray diffraction: Synchrotron X-ray diffraction experiments in the grazing incidence mode were performed at the 6D UNIST-PAL beamline of the Pohang Accelerator Laboratory in Korea. The synchrotron radiation from bending magnets was monochromatized to 18.986 keV using a Si(111) double crystal monochromator (DCM), and X-ray diffraction patterns were obtained at an incidence angle of 0.01 to 0.3° for ca. 4 x 4 mm² samples. The sample-to-detector distance was ca. 242.5 mm.

Diffraction patterns were collected with a 2D CCD detector (MX225-HS, Rayonix L.L.C., USA), and diffraction angles were calibrated using LaB₆ NIST standard reference material (SRM 660b, <https://www.nist.gov/publications/certification-standard-reference-material-660b>).

Density-functional theory (DFT) calculations: DFT calculations were done with the Vienna ab initio simulation package (VASP).⁴² The PBE type exchange-correlation functional⁴³ was used as it predicts FCC Ni and Co lattice constants (Ni 3.513 Å, Co 3.514 Å) within ~0.2% error when compared with experiment^{44,45} and the bulk modulus values (Ni 188 GPa, Co 213 GPa) were also in good agreement with the experimental values (Ni 186 GPa, Co 196 GPa).^{45,46} The spin-polarization was considered in whole simulations with a 400 eV cutoff energy. In all slab structures, the vacuum size was greater than 15 Å. The structure optimizations were done until all the residual atomic forces became less than 0.01 eV/Å. To calculate the activation energies and to probe the mechanism of carbon diffusion and role of H₂O and thus the elimination of C at the free metal surface, the climbing image nudged elastic band (CI-NEB)⁴⁷ method was used. The temperature effect in the CI-NEB calculations was considered by choosing the reported high temperature lattice constants, corresponding to 3.58 Å for Ni (T = 1256 K) or 3.63 Å for Co (T = 1394 K), and 3.57 Å for diamond (T = 1273 K).^{44,48,49} The unit cell size for the metal-diamond interfaces was adjusted to the lattice parameters of Ni or Co with a lattice mismatch smaller than 1.5 %. In **Table 3.11**, the supercell size, surface Miller indices, slab thickness, interlayer distance, and K-point sampling of the simulated structures are given. The pressure effect or PV contribution in enthalpy is negligible for the interface or estimated as small as RT ~ 10.6 kJ/mol using T = 1273 K for gas production reactions at the surface.

Table 3.11 The detailed parameters of the simulation model.⁴⁹⁻⁵¹

Reaction	Supercell size	Slab layer number	Interlayer distance (Å)	K-point sampling
Ni(001) – H ₂ O	2x2	4		3x3x1
Ni(001) – D(001)	Ni: 2x2 D: 2x2	Ni: 4 D: 4	1.489	3x3x1
Bulk FCC Ni C diffusion (O-T site)	2x2x2			8x8x8
Co(001) – H ₂ O	2x2	4		3x3x1
Co(001) – D(001)	Co: 2x2 D: 2x2	Co: 4 D: 4	1.480	3x3x1
Bulk FCC Co C diffusion	2x2x2			8x8x8

(O-T site)				
Ni(110) – H ₂ O	3x3	4		2x2x1
Ni(110) – D(110)	Ni: 3x3 D: 3x3	Ni: 4 D: 4	1.379	2x2x1
Co(110) – H ₂ O	3x3	4		2x2x1
Co(110) – D(110)	Co: 3x3 D: 3x3	Co: 4 D: 4	1.428	2x2x1

References

- [1] Aharonovich, I.; Greentree, A. D.; Praver, S., Diamond photonics. *Nat Photonics* **2011**, *5* (7), 397-405.
- [2] Wort, C. J. H.; Balmer, R. S., Diamond as an electronic material. *Mater Today* **2008**, *11* (1-2), 22-28.
- [3] Pleskov, Y. V., Electrochemistry of diamond: A review. *Russ J Electrochem+* **2002**, *38* (12), 1275-1291.
- [4] Werner, M.; Locher, R., Growth and application of undoped and doped diamond films. *Rep Prog Phys* **1998**, *61* (12), 1665-1710.
- [5] Jelezko, F.; Wrachtrup, J., Single defect centres in diamond: A review. *Phys Status Solidi A* **2006**, *203* (13), 3207-3225.
- [6] Nebel, C. E.; Rezek, B.; Shin, D.; Uetsuka, H.; Yang, N., Diamond for bio-sensor applications. *J Phys D Appl Phys* **2007**, *40* (20), 6443-6466.
- [7] Balmer, R. S.; Brandon, J. R.; Clewes, S. L.; Dhillon, H. K.; Dodson, J. M.; Friel, I.; Inglis, P. N.; Madgwick, T. D.; Markham, M. L.; Mollart, T. P.; Perkins, N.; Scarsbrook, G. A.; Twitchen, D. J.; Whitehead, A. J.; Wilman, J. J.; Woollard, S. M., Chemical vapour deposition synthetic diamond: materials, technology and applications. *J Phys-Condens Mat* **2009**, *21* (36).
- [8] Kianinia, M.; Aharonovich, I., Diamond photonics is scaling up. *Nat Photonics* **2020**, *14* (10), 599-600.
- [9] Hicks, M. L.; Pakpour-Tabrizi, A. C.; Jackman, R. B., Diamond Etching Beyond 10 μm with Near-Zero Micromasking. *Sci Rep-Uk* **2019**, *9*.
- [10] Castelletto, S.; Rosa, L.; Blackledge, J.; Al Abri, M. Z.; Boretti, A., Advances in diamond nanofabrication for ultrasensitive devices. *Microsyst Nanoeng* **2017**, *3*.
- [11] Yan, J. W.; Imoto, Y., Nanoscale surface patterning of diamond utilizing carbon diffusion reaction with a microstructured titanium mold. *Cirp Ann-Manuf Techn* **2018**, *67* (1), 181-184.
- [12] Kononenko, T. V.; Kononenko, V. V.; Konov, V. I.; Pimenov, S. M.; Garnov, S. V.; Tishchenko, A. V.; Prokhorov, A. M.; Khomich, A. V., Formation of antireflective surface structures on diamond films by laser patterning. *Appl Phys a-Mater* **1999**, *68* (1), 99-102.
- [13] Hwang, D. S.; Saito, T.; Fujimori, N., New etching process for device fabrication using diamond. *Diam Relat Mater* **2004**, *13* (11-12), 2207-2210.
- [14] Ando, Y.; Nishibayashi, Y.; Kobashi, K.; Hirao, T.; Oura, K., Smooth and high-rate reactive ion etching of diamond. *Diam Relat Mater* **2002**, *11* (3-6), 824-827.
- [15] Kawabata, Y.; Taniguchi, J.; Miyamoto, I., XPS studies on damage evaluation of single-crystal diamond chips processed with ion beam etching and reactive ion beam assisted chemical etching. *Diam Relat Mater* **2004**, *13* (1), 93-98.
- [16] Kato, Y.; Kawashima, H.; Makino, T.; Ogura, M.; Traore, A.; Ozawa, N.; Yamasaki, S., Estimation of Inductively Coupled Plasma Etching Damage of Boron-Doped Diamond Using X-Ray Photoelectron Spectroscopy. *Phys Status Solidi A* **2017**, *214* (11).
- [17] Kunuku, S.; Sankaran, K. J.; Tsai, C. Y.; Chang, W. H.; Tai, N. H.; Leou, K. C.; Lin, I. N., Investigations on Diamond Nanostructuring of Different Morphologies by the Reactive-Ion Etching Process and Their Potential Applications. *Acs Appl Mater Inter* **2013**, *5* (15), 7439-7449.
- [18] Nagai, M.; Nakanishi, K.; Takahashi, H.; Kato, H.; Makino, T.; Yamasaki, S.; Matsumoto, T.; Inokuma, T.; Tokuda, N., Anisotropic diamond etching through thermochemical reaction between Ni and diamond in high-temperature water vapour. *Sci Rep-Uk* **2018**, *8*.
- [19] Nagai, M.; Nakamura, Y.; Yamada, T.; Tabakoya, T.; Matsumoto, T.; Inokuma, T.; Nebel, C. E.; Makino, T.; Yamasaki, S.; Tokuda, N., Formation of U-shaped diamond

- trenches with vertical {111} sidewalls by anisotropic etching of diamond (110) surfaces. *Diam Relat Mater* **2020**, 103.
- [20] Ferrari, A. C.; Meyer, J. C.; Scardaci, V.; Casiraghi, C.; Lazzeri, M.; Mauri, F.; Piscanec, S.; Jiang, D.; Novoselov, K. S.; Roth, S.; Geim, A. K., Raman spectrum of graphene and graphene layers. *Phys Rev Lett* **2006**, 97 (18).
- [21] Chatterjee, S.; Kim, N. Y.; Pugno, N. M.; Biswal, M.; Cunnig, B. V.; Goo, M.; Jin, S.; Lee, S. H.; Lee, Z.; Ruoff, R. S., Synthesis of Highly Oriented Graphite Films with a Low Wrinkle Density and Near-Millimeter-Scale Lateral Grains. *Chem Mater* **2020**, 32 (7), 3134-3143.
- [22] Beck, P.; Pommerol, A.; Schmitt, B.; Brissaud, O., Kinetics of water adsorption on minerals and the breathing of the Martian regolith. *J Geophys Res-Planet* **2010**, 115.
- [23] Haar, L.; Gallagher, J. S.; Kell, G. S., NBS/NRC Steam Tables; Hemisphere Publishing Corp. New York, 1984.
- [24] Brandes, E. A.; Brook, G. B. *Smithells Metals Reference Book. 7th ed.*; Butterworth-Heinemann, 1992; 13, p23.
- [25] Iijima, Y.; Makuta, F.; Agarwala, R. P.; Hirano, K., Diffusion of Carbon in Cobalt. *Mater T Jim* **1989**, 30 (12), 984-990.
- [26] Dahal, A.; Batzill, M., Graphene-nickel interfaces: a review. *Nanoscale* **2014**, 6 (5), 2548-2562.
- [27] Bauer, R.; Jagle, E. A.; Baumann, W.; Mittemeijer, E. J., Kinetics of the allotropic hcp-fcc phase transformation in cobalt. *Philos Mag* **2011**, 91 (3), 437-457.
- [28] Korchuganov, A. V.; Tyumentsev, A. N.; Zolnikov, K. P.; Litovchenko, I. Y.; Kryzhevich, D. S.; Gutmanas, E.; Li, S. X.; Wang, Z. G.; Psakhie, S. G., Nucleation of dislocations and twins in fcc nanocrystals: Dynamics of structural transformations. *J Mater Sci Technol* **2019**, 35 (1), 201-206.
- [29] Smith, R. J. B.; Loganathan, M.; Shantha, M. S., A Review of the Water Gas Shift Reaction Kinetics. *Int J Chem React Eng* **2010**, 8.
- [30] Vertman, A. A.; Grigorovich, V. K.; Nedumov, N. A.; Samarin, A. M., An investigation into the cobalt-carbon and nickel-carbon systems. *Dokl. Akad. Nauk SSSR* **1965**, 162:6, 1304-1305.
- [31] Watson, E. B., Diffusion and Solubility of C in Pt. *Am Mineral* **1987**, 72 (5-6), 487-490.
- [32] Lander, J. J.; Kern, H. E.; Beach, A. L., Solubility and Diffusion Coefficient of Carbon in Nickel - Reaction Rates of Nickel-Carbon Alloys with Barium Oxide. *J Appl Phys* **1952**, 23 (12), 1305-1309.
- [33] Luo, H.; Park, S.; Chan, H. Y. H.; Weaver, M. J., Surface oxidation of platinum-group transition metals in ambient gaseous environments: Role of electrochemical versus chemical pathways. *J Phys Chem B* **2000**, 104 (34), 8250-8258.
- [34] Luo, D.; Yang, F.; Wang, X.; Sun, H.; Gao, D. L.; Li, R. M.; Yang, J.; Li, Y., Anisotropic Etching of Graphite Flakes with Water Vapor to Produce Armchair-Edged Graphene. *Small* **2014**, 10 (14), 2809-2814.
- [35] Cunnig, B. V.; Wang, B.; Shin, T. J.; Ruoff, R. S., Structure-directing effect of single crystal graphene film on polymer carbonization and graphitization. *Mater Horiz* **2019**, 6 (4), 796-801.
- [36] Zhang, Y. J.; Zhu, Y.; Cao, Y.; Li, D.; Zhang, Z. D.; Wang, K. J.; Ding, F.; Wang, X. L.; Meng, D.; Fan, L. H.; Wu, J., Size and morphology-controlled synthesis of Ni₃C nanoparticles in a TEG solution and their magnetic properties. *Rsc Adv* **2016**, 6 (85), 81989-81994.
- [37] Bayer, B. C.; Bosworth, D. A.; Michaelis, F. B.; Blume, R.; Habler, G.; Abart, R.; Weatherup, R. S.; Kidambi, P. R.; Baumberg, J. J.; Knop-Gericke, A.; Schloegl, R.; Baetz, C.; Barber, Z. H.; Meyer, J. C.; Hofmann, S., In Situ Observations of Phase Transitions in Metastable Nickel (Carbide)/Carbon Nanocomposites. *J Phys Chem C* **2016**, 120 (39), 22571-22584.

- [38] Ruf, M.; IJspeert, M.; van Dam, S.; de Jong, N.; van den Berg, H.; Evers, G.; Hanson, R., Optically Coherent Nitrogen-Vacancy Centers in Micrometer-Thin Etched Diamond Membranes. *Nano Lett* **2019**, *19* (6), 3987-3992.
- [39] Kara, V.; Sohn, Y. I.; Atikian, H.; Yakhot, V.; Loncar, M.; Ekinci, K. L., Nanofluidics of Single-Crystal Diamond Nanomechanical Resonators. *Nano Lett* **2015**, *15* (12), 8070-8076.
- [40] Field, D. E.; Cuenca, J. A.; Smith, M.; Fairclough, S. M.; Massabuau, F. C. P.; Pomeroy, J. W.; Williams, O.; Oliver, R. A.; Thayne, I.; Kuball, M., Crystalline Interlayers for Reducing the Effective Thermal Boundary Resistance in GaN-on-Diamond. *ACS Appl Mater Inter* **2020**, *12* (48), 54138-54145.
- [41] Cui, S. Y.; Greenspon, A. S.; Ohno, K.; Myers, B. A.; Jayich, A. C. B.; Awschalom, D. D.; Hu, E. L., Reduced Plasma-Induced Damage to Near-Surface Nitrogen-Vacancy Centers in Diamond. *Nano Lett* **2015**, *15* (5), 2887-2891.
- [42] Kresse, G.; Furthmuller, J., Efficient iterative schemes for ab initio total-energy calculations using a plane-wave basis set. *Phys Rev B* **1996**, *54* (16), 11169-11186.
- [43] Perdew, J. P.; Burke, K.; Ernzerhof, M., Generalized gradient approximation made simple. *Phys Rev Lett* **1996**, *77* (18), 3865-3868.
- [44] Suh, I.K.; Ohta, H.; Waseda, Y., High-temperature thermal expansion of six metallic elements measured by dilatation method and X-ray diffraction. *Journal of Materials Science*, **1988**, *23*, 757-760.
- [45] Armentrout, M. M.; Kavner, A., A new high pressure and temperature equation of state of fcc cobalt. *J Appl Phys* **2015**, *118* (19).
- [46] Kittel, C. *Introduction to Solid State Physics*, 8th ed.; John Wiley & Sons, Inc.: New York, 2005; p52.
- [47] Henkelman, G.; Uberuaga, B. P.; Jonsson, H., A climbing image nudged elastic band method for finding saddle points and minimum energy paths. *J Chem Phys* **2000**, *113* (22), 9901-9904.
- [48] L. Marick, Variation of Resistance and Structure of Cobalt with Temperature and a Discussion of Its Photoelectric Emission. *Phys Rev* **1936**, *49*, 831.
- [49] Straumanis, M. E.; Aka, E. Z., Precision Determination of Lattice Parameter, Coefficient of Thermal Expansion and Atomic Weight of Carbon in Diamond. *J Am Chem Soc* **1951**, *73* (12), 5643-5646.
- [50] Wyckoff, R.W.G., *Crystal Structures*, John Wiley, New York, **1963**, 7-83.
- [51] Jorgensen, J. E.; Smith, R. I., On the compression mechanism of FeF₃. *Acta Crystallogr B* **2006**, *62*, 987-992.

IV Vapor-liquid-solid (VLS) growth of graphene ribbons on Cu foil and its kinetics study

4.1 Introduction

Graphene nanoribbon is a potential candidate for electronic devices due to its excellent mechanical, thermal, and electronic properties. In general, monolayer graphene film is a zero-bandgap material and one of the ways to introduce a band gap in graphene is by making it in the form of ribbons with tens of nanometers width.¹ Graphene ribbons (GRs) have been obtained by directly cutting a graphene film. This can be done by several methods, like laser cutting, lithographic processing or patterned etching.²⁻⁴ Unzipping single-wall carbon nanotubes (SWCNT) into GRs has been reported.^{5,6} The growth of a graphene ribbon on a SiC substrate following the sublimation of Si has been reported.⁷ GRs have been obtained on molten copper by combining conventional CVD growth of graphene with concurrent hydrogen etching;⁸ the GRs are formed through a competition between standard vapor-solid (VS) graphene growth and etching.

We separately reported the *discovery* of GRs growth on polycrystalline Cu foils catalyzed by “contamination” nanoparticles from a CVD system,⁹ and here we report and describe our detailed study of ‘bottom-up’ growth of tapered GRs by what is likely a vapor-liquid-solid (VLS) mechanism, which builds on the discovery described in reference 9.

A focus here is on use of single crystal copper foils, primarily Cu(111) but also Cu(100) and Cu(110) and we find that single crystal GRs grow with epitaxy on each of these surface types; commercial silica particles with nominal diameter of about 20 nm are dispersed on the single crystal Cu foil substrates, and during exposure to C₂H₄, hydrogen (H₂) and argon (Ar) gas, their chemical composition changes prior to and/or during GR growth. We elucidate the chemical composition of the resulting nanoparticles that catalyze the longitudinal (VLS) growth of tapered GRs, how the ‘taper angle’ of the tapered GRs is controlled entirely by the absolute temperature, and why the GRs are aligned along only the <110> crystallographic direction on Cu(111), Cu(110), and Cu(100) foils. At growth temperatures below 900 °C, the taper angle is zero (the GRs are constant width along their length) but tapered GRs with non-zero taper angle grow above 900 °C. We thus describe how particle-mediated growth can be used for the preparation of graphene ribbons on Cu substrates (with most of our study focusing on Cu(111) foil) of controlled shape—from uniform width to “tapered” ribbons with taper angles as large as 35 degrees, and down to zero.

In terms of VLS growth, a wide range of one dimensional (1D) semiconductor nanowires catalyzed by a nanoparticle have been extensively reported;^{10,11} indeed, the first study of VLS growth as reported

by Wagner and Ellis was of relatively large “wires” of silicon from large Au particles that melted on Si substrates due to formation of the Au-Si eutectic.¹² For nanowires, typically, gaseous precursors decompose on the surface of a nanoparticle and the active species diffuse either through the particle (“bulk” diffusion), or “around” the particle (surface diffusion), such that at the liquid-solid interface, a nanowire grows. If the catalyst particle is not molten at the growth temperature, the growth is typically referred to as vapor-solid-solid (VSS) growth. In VLS growth, selecting a suitable catalytic particle and controlling growth conditions can in some cases allow to vary the morphology of the nanoobjects including their size and shape.¹³

The VLS growth of primarily uniform-width MoS₂ nanoribbons by forming Na–Mo–O droplets on NaCl and MoS₂ substrates at high temperature¹⁴ and tapered MoS₂ nanoribbons grown on SiO₂/Si substrate by using Ni particles¹⁵ have been reported, and other than the GRs described in reference 9 and here, are the only 2D material ribbons to have been grown by VLS that we are aware of.

Because metal particles often used for VLS growth, such as Ni,¹⁶ Fe,¹⁷ Co,¹⁸ and Au,¹⁹ would quickly diffuse into the Cu foil substrate during the heating-up stage, metal particles are likely not suitable for GR growth on Cu. We grew GRs from silica particles dispersed on a Cu foil that formed a relatively stable Cu-Si-O alloy under the growth condition (Si nanoparticles, and also Ni, NiO, and Cu₅Si nanoparticles, were also tried but each type was “consumed” by the Cu substrate and did not catalytically grow GRs). Spectroscopic and microscopic characterization showed that GRs formed on the Cu substrate originated from ‘silica’ particles (but their composition evolves and is not simply SiO_x). The crystalline quality of the ribbons was similar to that of the graphene islands that nucleate and grow on the same single crystal Cu surface (without the participation of silica particles) under the same conditions. The growth mechanism was investigated in detail by kinetic studies and high-resolution microscopy. By changing the growth temperature, the ribbon morphology from a tapered shape (grown at > 900 °C) to rectangular (grown at < 900 °C). Finally, we measured the electrical properties of the as-grown GRs by fabricating GR back-gated field effect transistors (“GR-FETs”).

4.2 Results and discussion

4.2.1 Morphology and characterization of graphene ribbons

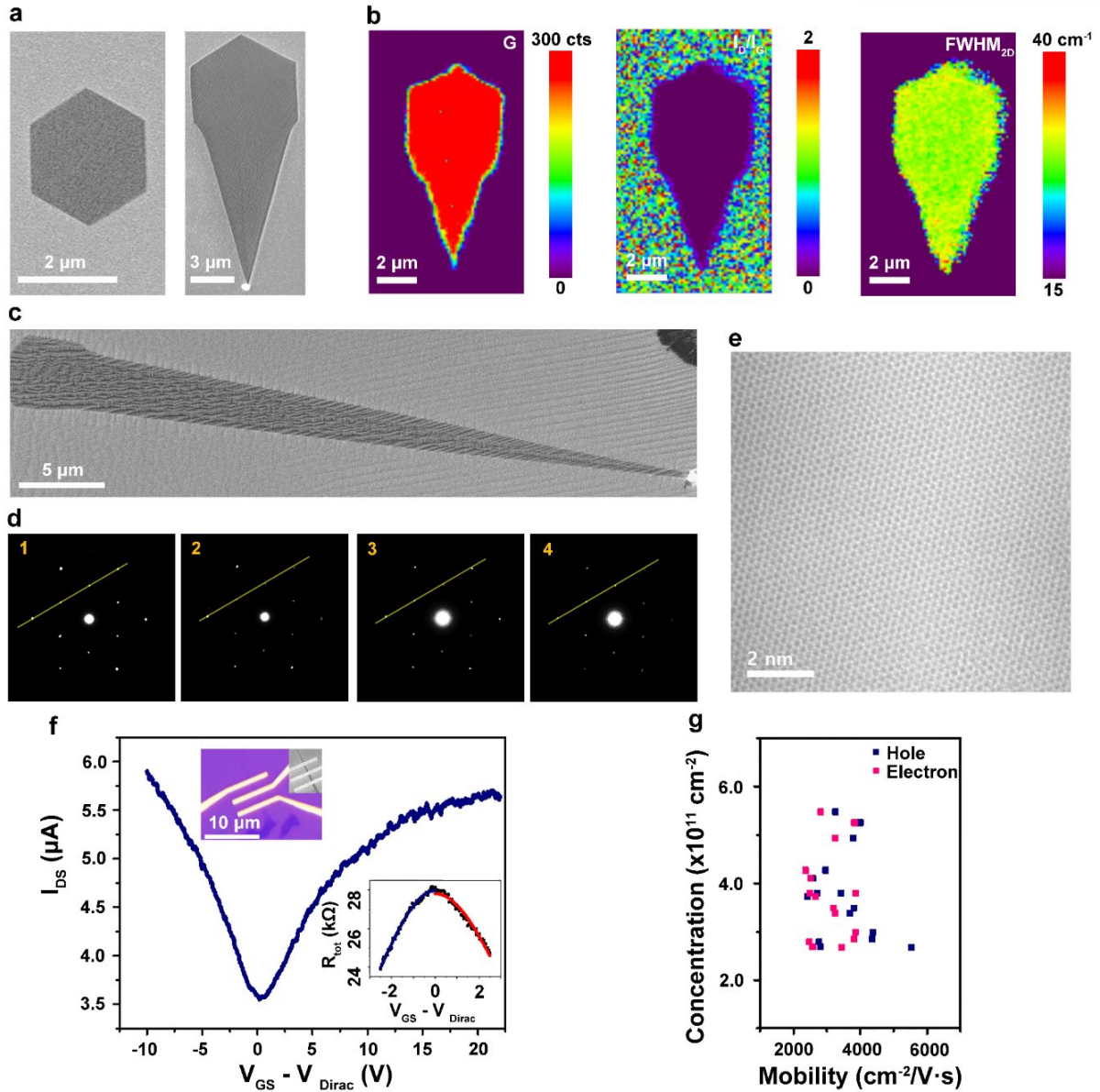


Figure 4.1 (a) SEM images of a hexagonal graphene island and a graphene ribbon with a silica particle at its tip. (b) Raman maps of a GR showing G band intensity, I_D/I_G ratio, and FWHM of 2D band. (c) A $\sim 35\mu\text{m}$ -length monolayer GR grown on Cu(111) foil substrate. (d) SAED patterns at 4 different positions on the ribbon. (e) HRTEM atomic image of graphene lattice. (f) $I_{\text{DS}} \sim V_{\text{GS}} - V_{\text{Dirac}}$ transportation curve of one GR-FET, (inserts: OM and SEM images of GR-FETs, and curve showing the total resistance vs. back-gate voltage ($R_{\text{tot}} \sim V_{\text{GS}} - V_{\text{Dirac}}$) of the GR-FET). (g) Data on carrier mobility vs. intrinsic carrier density measured at 300 K.

Graphene ribbons (GRs) were grown by atmospheric pressure CVD from silica particles previously dispersed on a Cu(111) surface. **Figure 4.1a** shows scanning electron microscope (SEM) images of a

hexagonal graphene island and a GR with a silica particle at the tip. The epitaxial growth of graphene on a Cu(111) foil gives rise to hexagonal monolayer graphene islands.²⁰ In our experiments, we find that in the presence of silica particles, GRs that remained connected to a silica particle are formed. The presence of a silica particle at the tip of a GR was observed by atomic force microscope (AFM) (**Figure 4.2**). Raman mapping of the G band ($\sim 1580 \text{ cm}^{-1}$) indicated that the GR was uniform and the low I_D/I_G ratio (~ 0.1) (**Figure 4.1b**) showed that the GR had good quality with none or few defects. The uniform full width at half-maximum (FWHM $\sim 30 \text{ cm}^{-1}$) value of the 2D band ($\sim 2680 \text{ cm}^{-1}$) is characteristic of a uniform monolayer of graphene over the whole area of the ribbon.²¹ In regions of the same Cu foil where no silica particles were present, monolayer hexagonal graphene islands were grown under the same growth conditions, as shown in **Figure 4.3** (for details on growth conditions please see **Figure 4.4**). Since monolayer GRs and hexagonal graphene islands are formed under the same experimental conditions, are epitaxial to the Cu(111) substrate, and their Raman spectra are similar with low D band peak intensity (**Figure 4.5**), we suggest that the GR had the same ‘quality’ as the hexagonal graphene island. By using a time of exposure to C_2H_4 , H_2 , and Ar of 50 mins at 950°C needle-shaped GRs over $30 \mu\text{m}$ in length (**Figure 4.1c**) were obtained. It is now well known that hexagonal graphene islands on Cu(111) are typically single crystals grown from a single nucleus.²² We carried out high-resolution transmission electron microscope (HRTEM) imaging on the GRs to elucidate its structure. **Figure 4.1d** shows that selected area electron diffraction (SAED) patterns obtained at 4 different positions (**Figure 4.6**) along a single ribbon are essentially identical (6 ribbons were randomly chosen and studied by TEM: all 6 were found to be single crystal over their whole sample area). For needle-like GRs, we also imaged the GR at the point where it started to taper. A single SAED pattern consisting of 6 spots (**Figure 4.7**) and the HRTEM atomic image (**Figure 4.1e**) of a graphene lattice without any lattice defects indicate that the GR at this point is a single crystal. Thus, our needle-like GRs are typically single crystals.

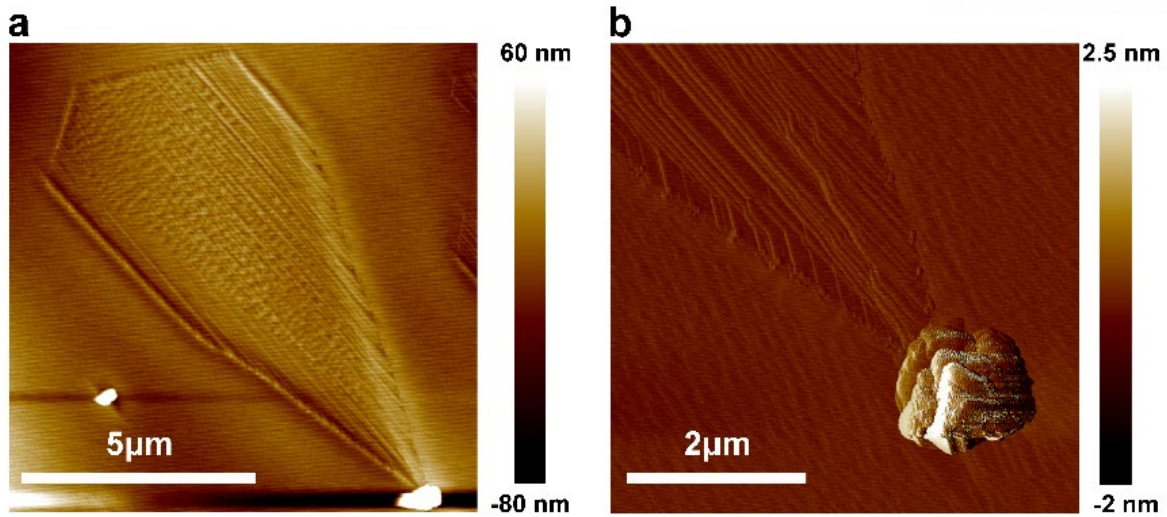


Figure 4.2 (a) AFM height image of a graphene ribbon (GR) and the catalytic particle. (b) AFM amplitude error image of a particle contacted to a tapered GR.

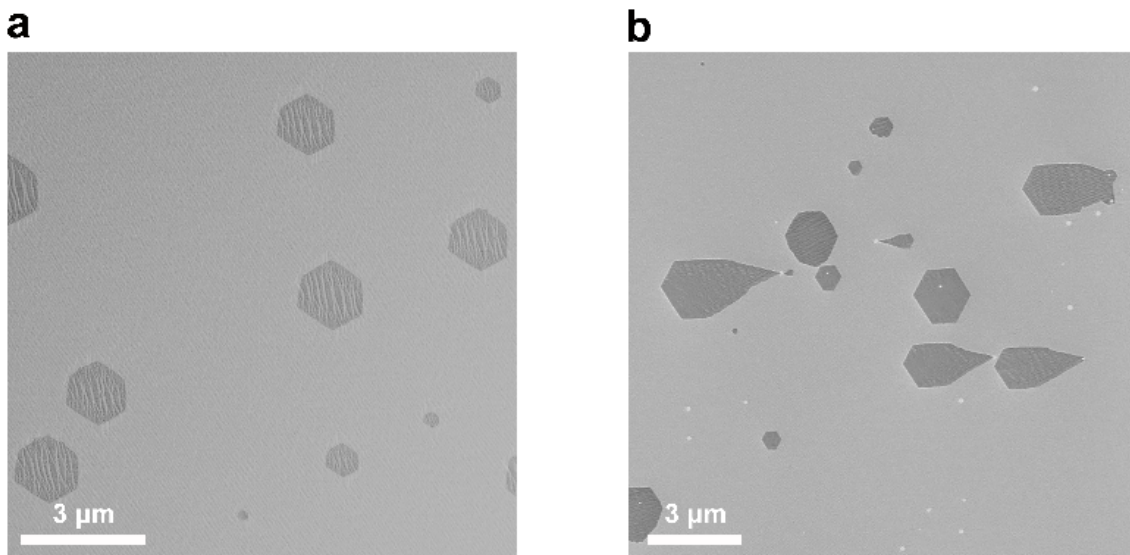


Figure 4.3 (a-b) SEM images of (a) graphene islands and (b) graphene ribbons (GRs) on a bare Cu(111) foil or a Cu(111) foil coated with silica particles. This shows that that in the presence of the silica particles, graphene islands and GRs grow under the same CVD conditions and co-exist.

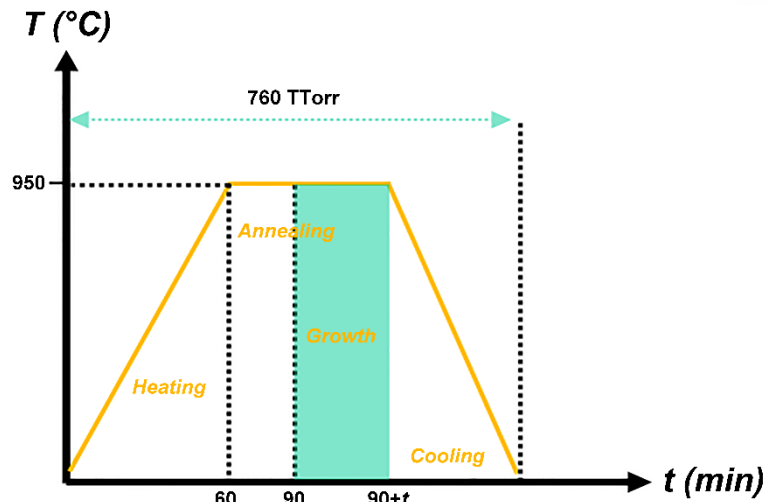


Figure 4.4 Temperature-time profile for the growth of graphene island/ribbon. In general, the growth conditions for monolayer graphene islands and GRs were found to be the same, and that without silica particles no ribbons were formed and only graphene islands were grown.

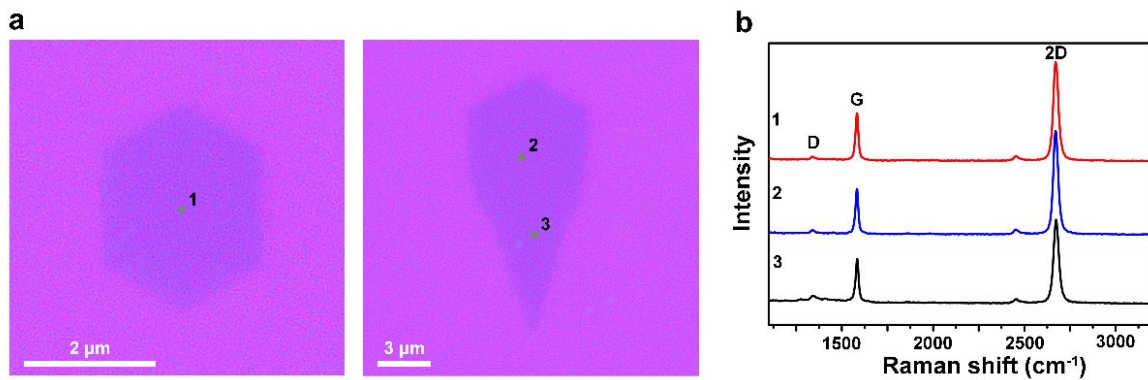


Figure 4.5 (a) Optical images (OM) of a hexagonal monolayer graphene island and a monolayer GR transferred on 300nm-SiO₂/Si wafer. (b) Raman spectra of graphene island and of GR (The selected positions are shown in a and labeled as 1, 2, 3). Raman spectra show low D band peak intensity for graphene island and GR.

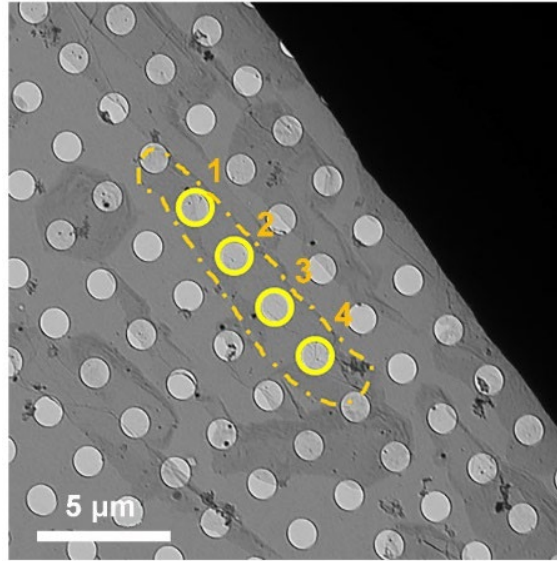


Figure 4.6 TEM image of GR transferred onto a TEM grid.

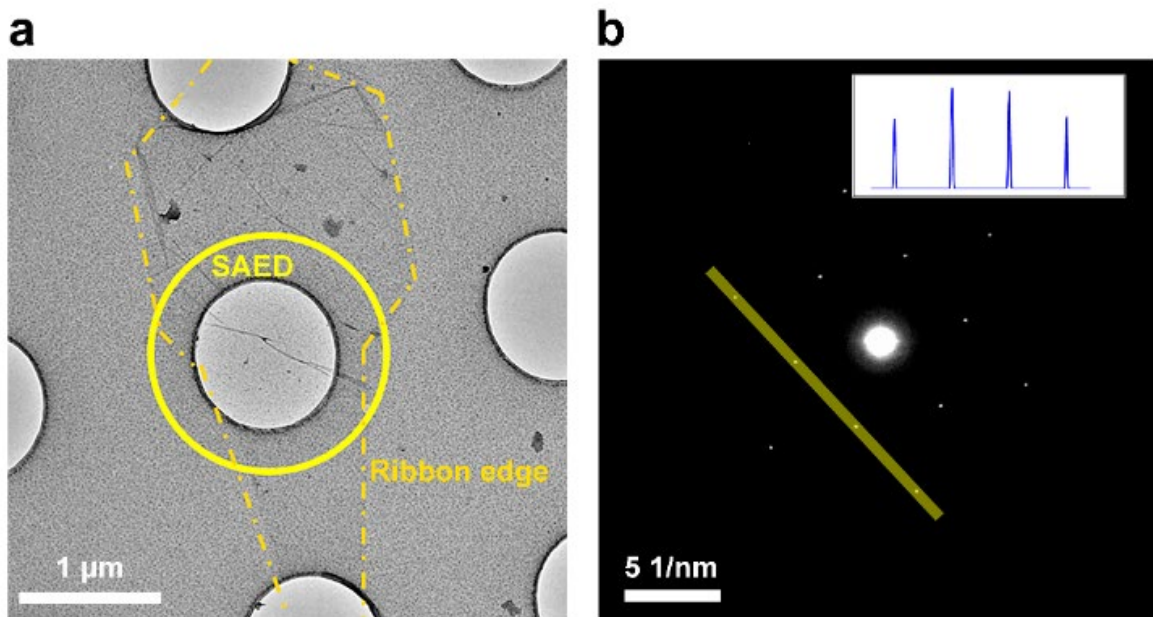


Figure 4.7 (a) SEM image of a GR from a sample transferred onto a TEM grid. (b) SAED pattern of a GR. The TEM study found that the GR at the elongated region is single crystal without grain boundaries.

We fabricated back-gated graphene ribbon field effect transistors (“GR-FETs”) to measure the electrical properties at 300 K and 10 K of single crystal monolayer GRs (see details in Experimental section) that had a taper angle close to zero (primarily constant width). At 300 K, the $I_{DS} \sim V_{GS} - V_{Dirac}$ curve and total resistance vs. back gate voltage ($R_{tot} \sim V_{GS} - V_{Dirac}$) curve for a GR-FET with a $500 \text{ nm} \times 2 \text{ } \mu\text{m}$ ($W \times L$) channel are shown in **Figure 4.1f**. Using the nonlinear fitting method based on the constant

mobility model,²³ the hole and electron carrier mobilities, and the intrinsic carrier density were calculated to be $\sim 3,700 \text{ cm}^2 \cdot \text{V}^{-1} \cdot \text{s}^{-1}$, $3,300 \text{ cm}^2 \cdot \text{V}^{-1} \cdot \text{s}^{-1}$ and $3.38 \times 10^{11} \text{ cm}^{-2}$ at 300 K, respectively. We also tested GR-FETs fabricated from GRs of different widths in the range $\sim 300 \text{ nm}$ to 800 nm and the data are shown in Figure S9. $I_{\text{DS}} \sim V_{\text{GS}} - V_{\text{Dirac}}$ curves showed similar $I_{\text{on}}/I_{\text{off}}$ ratio (~ 2.06), indicating good uniformity of these non-tapered GRs.²⁴ **Figure 4.1g** presents intrinsic carrier concentration vs. hole/electron carrier mobility of 15 individual GFETs at 300 K. The average hole and electron carrier mobilities, and intrinsic carrier density were $\sim 3,500 \text{ cm}^2 \cdot \text{V}^{-1} \cdot \text{s}^{-1}$, $\sim 3,100 \text{ cm}^2 \cdot \text{V}^{-1} \cdot \text{s}^{-1}$ and $\sim 3.75 \times 10^{11} \text{ cm}^{-2}$ (the corresponding values for all 15 GFETs are shown in **Table 4.1**). The average hole and electron carrier mobilities, and the intrinsic carrier density at 10 K were $\sim 4,300 \text{ cm}^2 \cdot \text{V}^{-1} \cdot \text{s}^{-1}$, $\sim 4,000 \text{ cm}^2 \cdot \text{V}^{-1} \cdot \text{s}^{-1}$ and $\sim 3.22 \times 10^{11} \text{ cm}^{-2}$ for 8 individual GFETs (the values for the 8 GR-FETs are shown in **Table 4.2**). The average values are comparable with the values that have been previously reported²⁵⁻²⁸ for graphene ribbons prepared by CVD growth (not VLS growth).

Table 4.1 Carrier mobility and intrinsic carrier density of 15 GR-FETs at 300 K. (Two significant figures are shown for the average mobility values at the bottom of the table.)

Number	Hole mobility ($\text{cm}^2/\text{V}^{-1}\text{s}^{-1}$)	Electron mobility ($\text{cm}^2/\text{V}^{-1}\text{s}^{-1}$)	Intrinsic carrier density (cm^{-2})
#1	3,784	3,244	4.94E+11
#2	4,000	3,828	5.26E+11
#3	3,418	3,865	3.80E+11
#4	4,356	3,805	2.85E+11
#5	4,383	3,854	2.99E+11
#6	3,253	2,819	5.48E+11
#7	2,415	2,663	3.73E+11
#8	2,967	2,362	4.27E+11
#9	2,799	2,575	2.69E+11
#10	3,690	3,261	3.38E+11
#11	2,769	2,474	2.79E+11
#12	3,807	3,205	3.49E+11
#13	5,539	3,445	2.67E+11
#14	2,711	2,481	3.80E+11
#15	2,577	2,510	4.10E+11
Average value	3.5E3	3.1E3	~3.75E+11

Table 4.2 Carrier mobility and intrinsic carrier density of 8 GR-FETs at 10 K. (Two significant figures are shown for the average mobility values at the bottom of the table.)

Number	Hole mobility ($\text{cm}^2/\text{V}^{-1}\text{s}^{-1}$)	Electron mobility ($\text{cm}^2/\text{V}^{-1}\text{s}^{-1}$)	Intrinsic carrier density (cm^{-2})
#1	4,429	4,221	3.21E+11
#2	5,029	4,752	2.79E+11
#3	4,144	3,857	3.36E+11
#4	3,890	3,529	3.45E+11
#5	4,978	4,537	3.18E+11
#6	4,311	4,015	3.11E+11
#7	3,870	3,533	3.23E+11
#8	4,075	3,820	3.42E+11
Average value	4.3E3	4.0E3	3.22E+11

4.2.2 Growth behavior of graphene ribbons

In conventional CVD growth of graphene islands/film on a Cu foil, carbon sources like methane (CH_4) usually diluted with H_2 and Ar are used.²⁹ The Cu foil acts both as a growth substrate and catalyst to promote the decomposition of the gaseous carbon precursor for growth of graphene islands/films. Typically, the growth temperature is in the range of 1000 to 1080 °C and pressure can be from relatively low values up to atmospheric pressure or 760 Torr. For ribbon growth, we seeded commercial silica particles on Cu(111) foil. First, a series of experiments were done where the position of a selected particle connected to a GR was monitored after each of two growth cycles and compared its original position on the substrate (**Figure 4.8**). At the end of a cycle the sample was cooled to room temperature and imaged the sample by SEM, after which the GRs were etched away by hydrogen plasma. This same Cu(111) foil substrate was then reinserted into the CVD growth system for a 2nd cycle of growth. Results from this 2nd cycle of growth showed that the particles again moved on the Cu(111) foil and new ribbons attached to them grew. Thus, the particle's movement appeared to guide the growth of the ribbon.

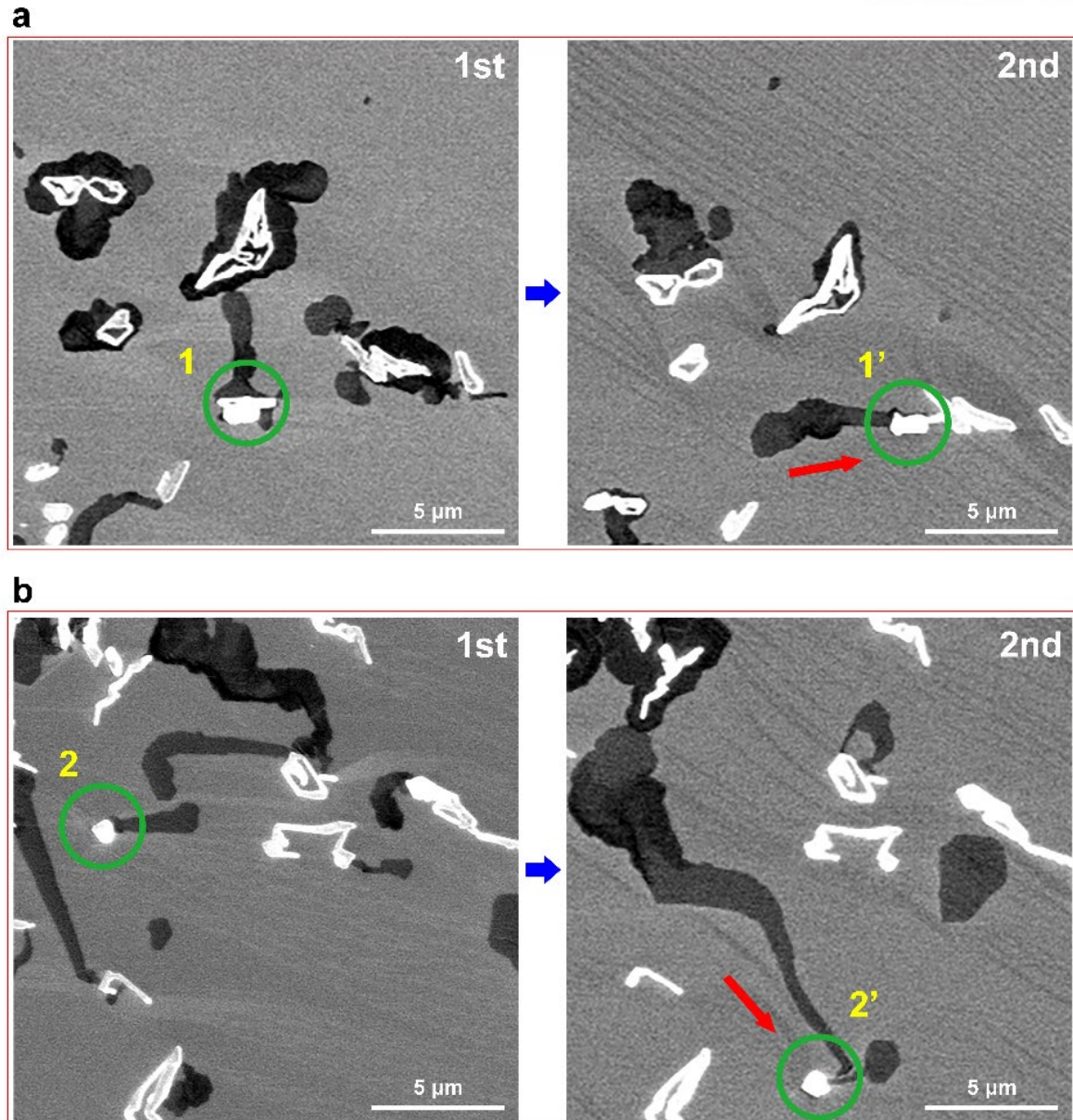


Figure 4.8 SEM images of GRs grown on a Cu(111) foil. To try to study the movement of particles during GR growth we obtained SEM images at different stages (cycle) of growth. As we used a quartz tube CVD system, some silica particles from the tube reactor were deposited on the Cu(111) foil substrate. (We note that this was in the initial stages of our work. We later were able to eliminate all contamination particles in our CVD-7 system in CMCM.) A first growth cycle was done as shown in a-b. We selected two particles: 1# and 2#. We then used a H₂ plasma cleaner (10 SCCM H₂, 120W, 10 mins) to remove the GRs from the Cu(111) foil and carried out the growth a second time using the same Cu foil under the same growth condition. (500 SCCM Ar, 250 SCCM H₂, 0.3 SCCM 1% C₂H₄/Ar, 30 min). We then examined the relative positions of the two particles on the Cu foil. We found that these

same particles moved on the Cu(111) foil surface and the GRs grew along the direction of motion of the particle.

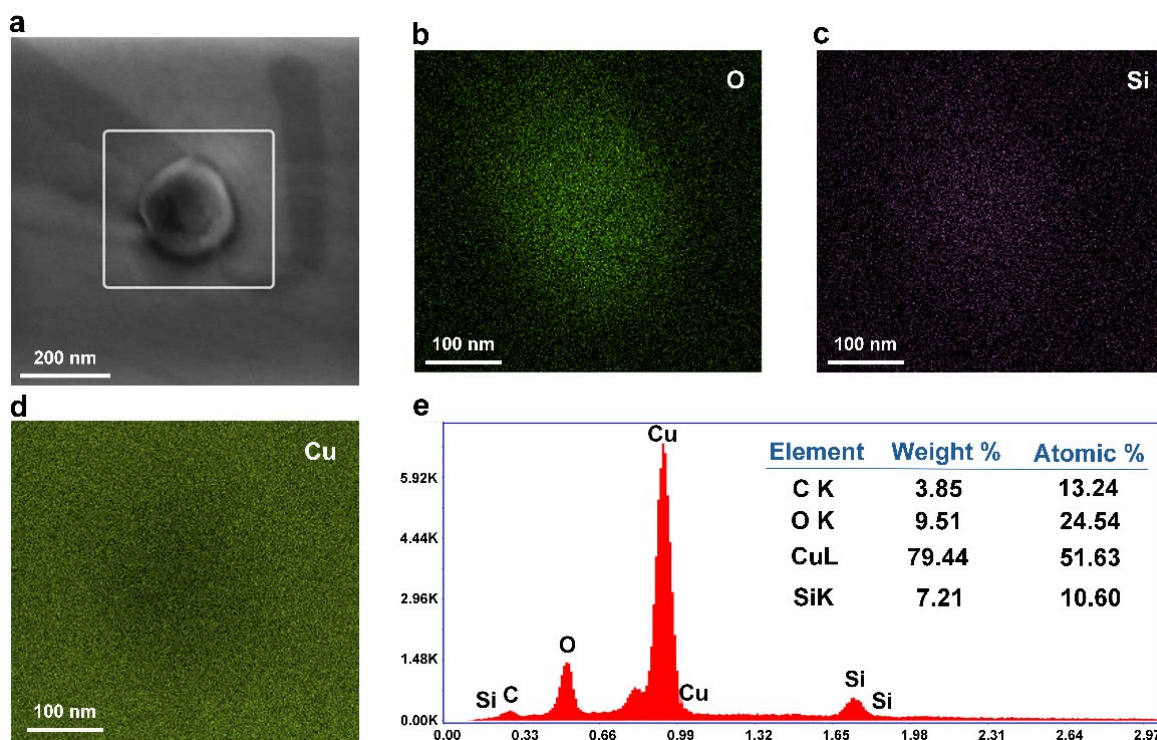


Figure 4.9 (a) SEM image of one particle at the tip of a GR. (b-d) EDS mapping of elemental (b) oxygen, (c) silicon and (d) copper. (e) EDS elemental analysis results of the particle. It is seen that the particles consist of silicon and oxygen, but the presence of copper cannot be ascertained since the analysis was carried out on a Cu substrate. The GR was therefore transferred onto a Au TEM grid for EDS analysis. The results are described in the main text.

To determine if there was any change in chemical composition of the silica particle during GR growth, energy dispersive X-ray spectroscopy (EDS) elemental analysis in a TEM of a particle that was connected to a GR (**Figure 4.9**) was done. To eliminate as much as possible the effect of the Cu substrate, the analysis was carried out after transferring the sample onto a Au TEM grid (**Figure 4.10a**). Si, O, Cu, and C were detected in the particle indicating that the particle chemical composition significantly changed during the growth of the GR. (We note it was not possible to unambiguously assign C as being present “in” the particle, as the particle is attached to the graphene ribbon.)

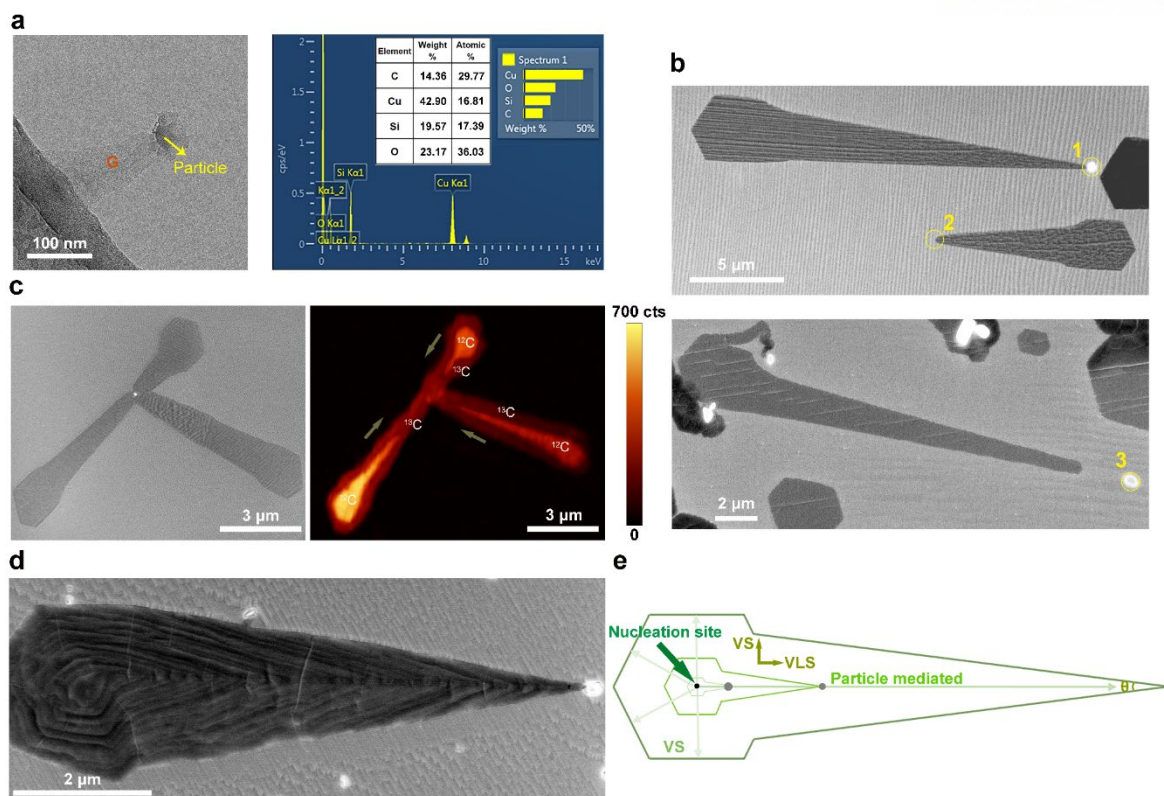


Figure 4.10 (a) EDS elemental analysis of the particle attached to a GR transferred onto a gold (Au) TEM grid. (b) SEM images of GRs connected or not connected to particles. (c) SEM image and Raman map of the G band intensity of isotopic ^{13}C labelled GRs. (d) SEM image of a multilayer GR. (e) Schematic image showing particle mediated and VS growth behaviors.

Some results were obtained for the GR growth in our CVD quartz furnace from which we inferred the disappearance/disconnection of particles during growth; the corresponding SEM images are presented in **Figure 4.10b**. At position #1, a particle was connected to that GR, but at position #2, only that particular GR was present. At position #3, a particle was present but was disconnected from this GR. These results suggest that GRs cannot grow longitudinally without the particles.

To try to understand why the particles sometimes disappeared during growth of a GR, we performed time-of-flight secondary ion mass spectrometry (ToF-SIMS) depth profiling to check the distribution of Si in the Cu foil substrate, as ToF-SIMS is highly sensitive to the element composition at the sample's surface and can be used to analyze the depth profile of each of the elements present. A sample containing many GRs (we chose to focus on a ribbon where the particle had disappeared) was loaded into the ToF-SIMS chamber and maintained in the high vacuum chamber ($5.0\text{E}-8$ mbar) for over 12 h to remove surface contamination. A primary beam (Bi^{3++} , 50 keV, 0.05 pA) was used to get the surface image and a sputter beam (Cs^+ , 500eV, 25 nA) was used to sputter the surface. To acquire depth profiling 3D

images, a $50 \times 50 \mu\text{m}$ area was imaged by non-interlaced mode (1 frame sputter 3 s, pause 1 s, 260 scans in total).

As shown in **Figure 4.11a**, the GR disconnected from the particle and the particle disappeared, presumably through diffusion into the substrate. To evaluate the possible surface diffusion of silicon into the substrate, we carried out silicon element 3D- depth mapping. It is important to note that the amount of silicon is much lower than the amount of Cu. We first sputtered the surface of the ribbon to locate the ribbon from its carbon signal, as shown in **Figures 4.11b-c**. We then continued sputtering to totally remove the graphene while starting the 3D depth profiling at the same time. At the tip region of the GR, we observed a higher silicon signal, as shown in **Figure 4.11d**. In the depth profiling, we also observed silicon signal contrast at the tip region inside the Cu foil as shown in **Figures 4.11e-f**. We suggest that at the growth stage, the ribbon was growing and the silicon in the particle was dissolving into the Cu foil along the growth direction. When the particle completely dissolved into the underlying Cu foil, the particle disappeared and the growth was stopped at the same time. Especially at the tip region, we could distinguish the silicon signal from the background noise as shown in **Figure 4.11d**. We note that the silicon signal contrast along the growth ‘footprint’ could not be observed possibly due to the diffusion of dissolved silicon in the Cu bulk. The dissolved silicon at the tip region had not completely diffused into the bulk of the Cu(111) foil, and the signal contrast could be distinguished from the background noise. Overall, ToF-SIMS results suggest that the particle is likely to have dissolved into the underlying Cu foil during growth.

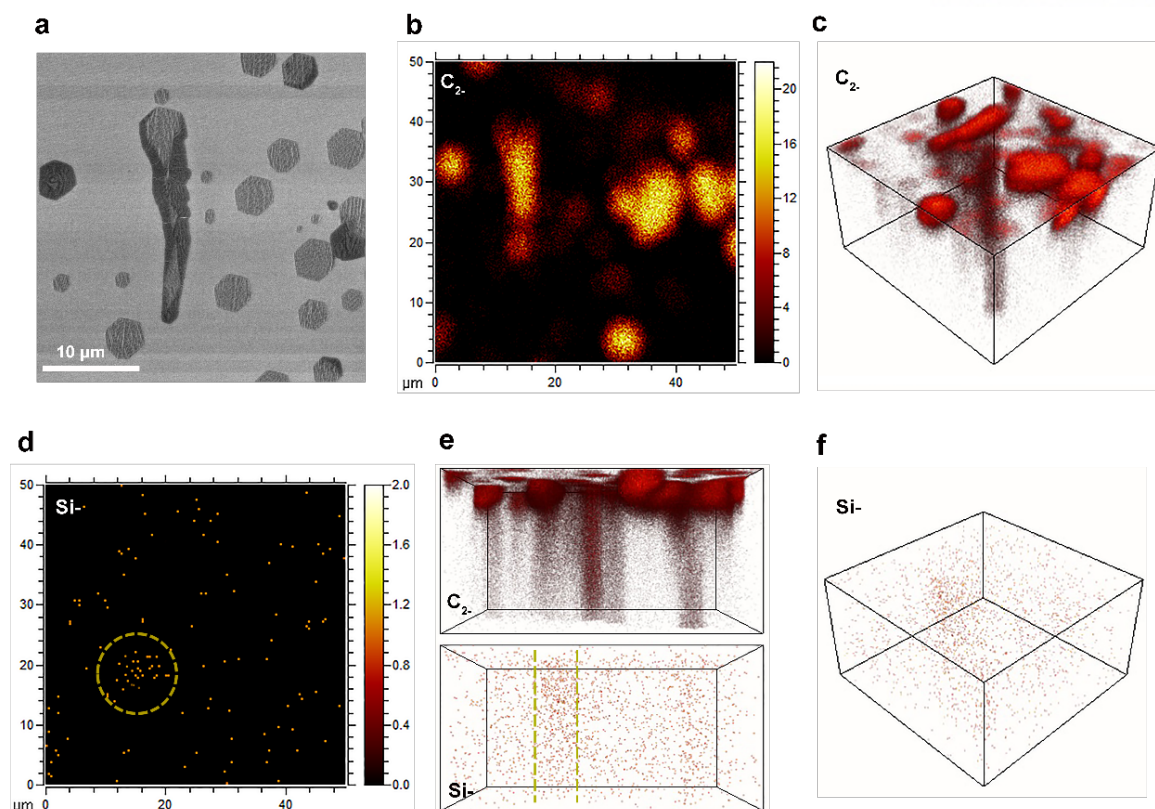


Figure 4.11 (a) SEM image of a GR where the particle dissolved into the underlying Cu. (b) The C_2^- species map at the early sputter stage and its (c) 3D image show the position of the ribbon. (d) Si- species map at the middle sputter stage showing silicon element distribution, (e–f) 3D images of C_2^- and Si- species distributions.

We observed a higher silicon signal in the depth profile at the tip of the GR, which suggested that the particles diffused into the Cu foil, which (eventually) stopped further growth of the GR (**Figure 4.11**). Here, we suggest that the silica particle could react with Cu in H_2 atmosphere according to: $Si_yO_x + xH_2 + xCu = Cu_xSi_y + xH_2O$. At the growth temperature, the eutectic compound (Cu_xSi_y) is unstable and Si thus diffused into the Cu foil. The silica particle (Si_yO_x) was, per this hypothesis, gradually consumed by the Cu substrate during GR growth and sometimes the particle even disappeared. We note here that the melting point of pure silica nanoparticles has been reported to be close to 1600 °C at 760 Torr,³⁰ which is higher than the growth temperatures employed in this study (a typical growth T was 950°C). The Cu-Si binary phase diagram³¹ shows that each of the eutectic compounds Cu_xSi_y (there are several such as: $Cu_{15}Si_4$, Cu_7Si_2 , Cu_3Si) is a molten alloy at temperatures above 825 °C. Thus, at the reaction temperatures we used, the particle responsible for ribbon growth (Si_yO_x) could be in the form of a molten or semi-molten alloy due to its reaction with the underlying Cu foil in the presence of H_2 gas.

In some cases, multiple GRs were contacted by only one particle. An example is shown in **Figure 4.10c** in which three GRs are contacted at one particle. To try to further understand the mechanism of GR formation, we did ^{13}C -labelling experiments. We first introduced 1% normal C_2H_4 in Ar gas for a fixed time period after which it was replaced by ^{13}C for further growth (we note that ^{13}C -labelled C_2H_4 was not readily available compared to ^{13}C). After growth, we transferred the GRs onto a SiO_2/Si substrate and did Raman mapping. **Figure 4.10c** shows the Raman map of the G band intensity where the intensity difference between ^{12}C and ^{13}C regions is clear. The intensity contrast suggests that the 3 different GRs grew independently from 3 particles at the early stage of growth, for a certain time. The particles then contacted each other at the tips of these 3 GRs and coalesced as a result of which only one particle remained at the tip. At this point, the merged particle may or may not continue to grow a ribbon; **Figure 4.12** illustrates both these scenarios. These results show that GR growth might follow a vapor-liquid-solid (VLS) growth mechanism, in which growth occurs after the deposition of carbon species on or into a molten particle or a liquid drop. It is noteworthy that the particles attached to GRs were typically (but not always) “essentially spherical” when cooled back to room temperature and observed by SEM and TEM. In contrast, the as-received particles are not spherical and we suggest this change in shape supports the VLS model—that is, that the particles were likely molten during growth of the GRs (**Figure 4.13**).

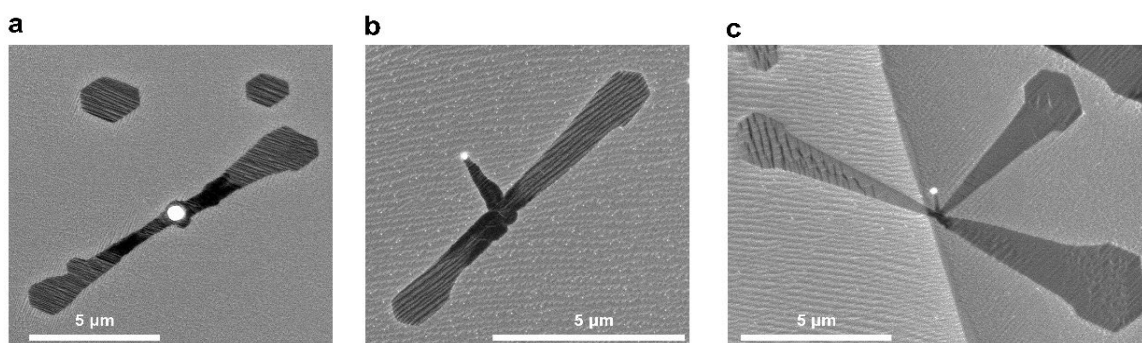


Figure 4.12 Since the particle was likely a molten/semi molten alloy at the growth temperature, the particles merged, which sometimes (a) stopped growth, or continued (b-c) to grow a GR.

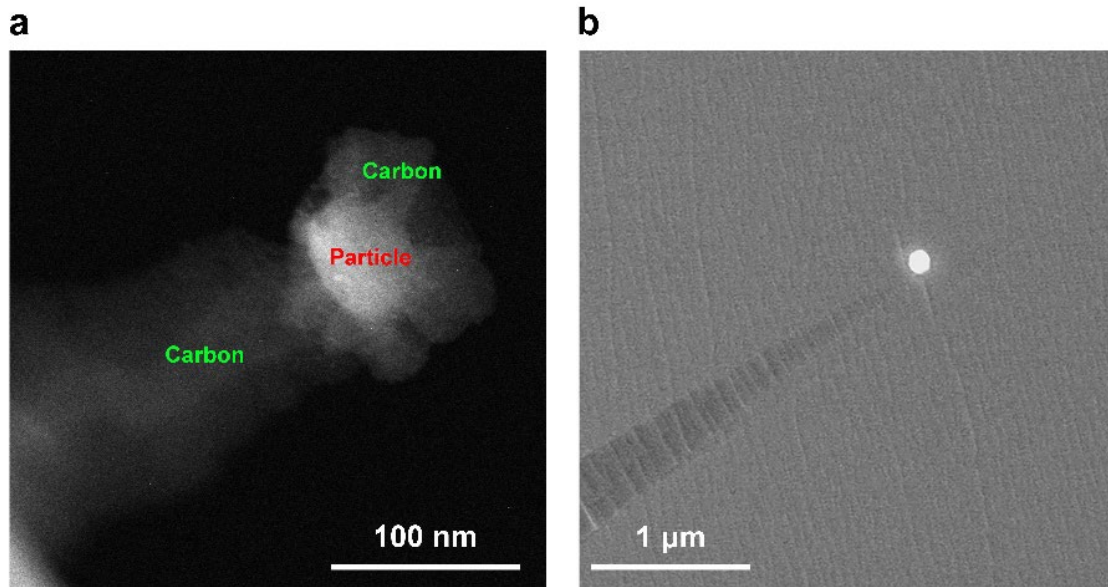


Figure 4.13 (a) TEM and (b) SEM images of a particle connected to a GR were typically nearly-spherical; we note that not all of particles guiding the growth of GRs are “so spherical”. The morphology changes (compared to irregular shape of the as-received commercial silica particles) suggests that the particles were molten during growth of the GRs.

Most as-grown GRs were needle-shaped regardless of whether they were single layer or multilayered. **Figure 4.10d** shows a multilayer GR grown on Cu foil. The thickness was not uniform over the whole area of the ribbon. AFM height images of monolayer vs multilayer graphene ribbons on Cu foils (**Figure 4.14**) showed that in a multilayer GR, the height at the center region was greater than at the edges.

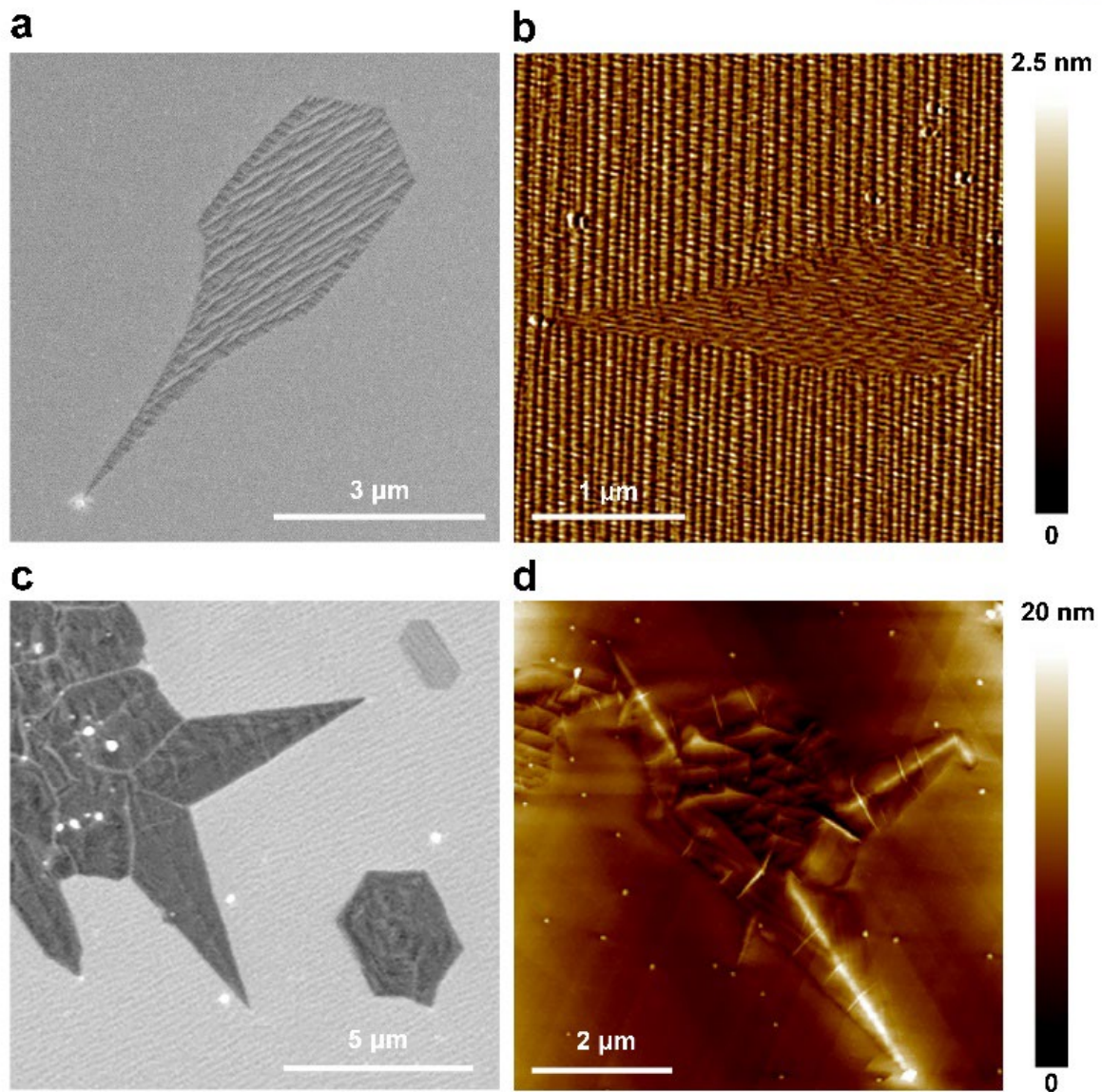


Figure 4.14 (a) SEM and (b) AFM images of a monolayer GR. (c) SEM and (d) AFM images of a multilayer GR. (c–d) show that the height of this multilayer GR at the center is higher than at the edge.

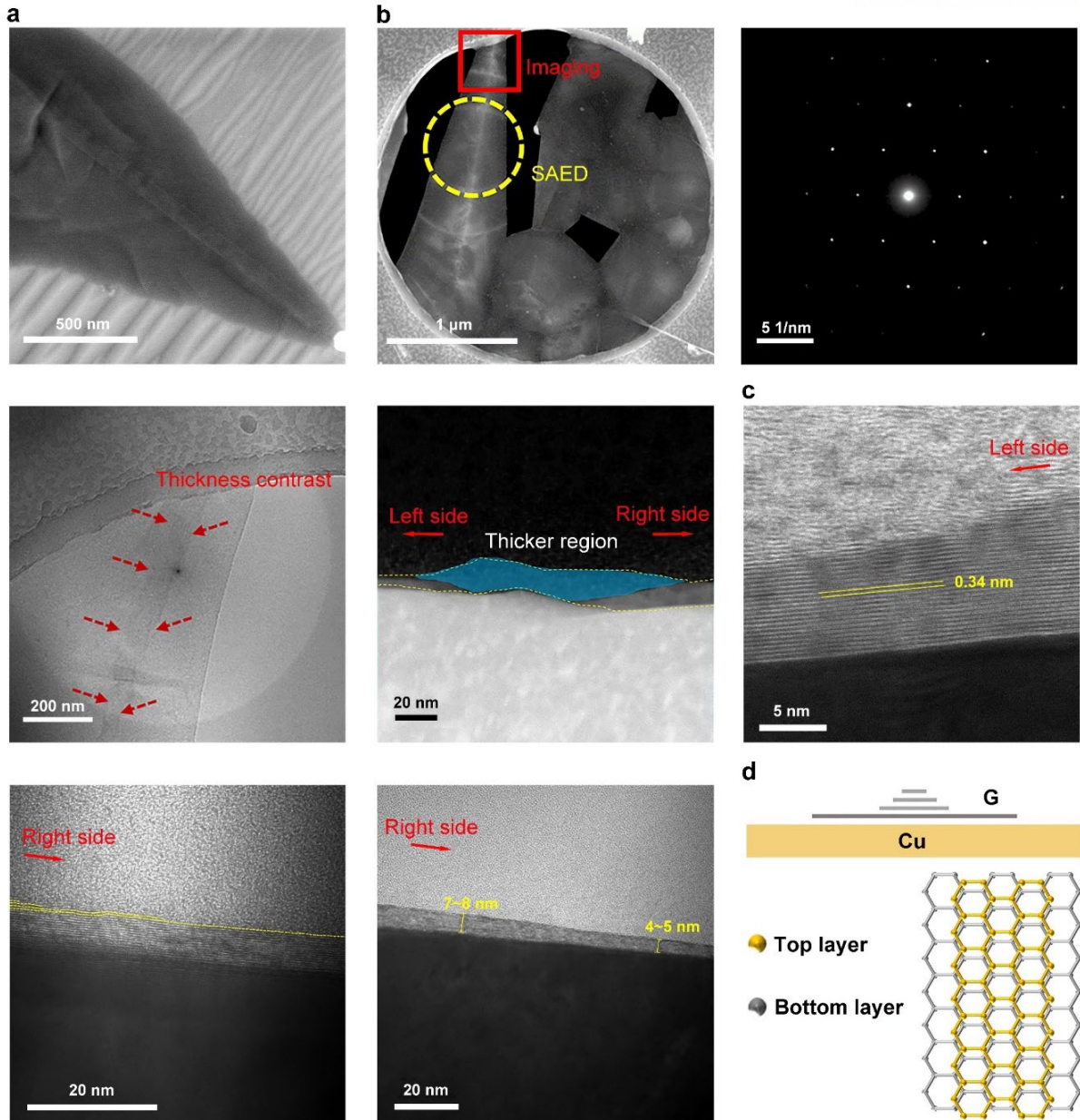


Figure 4.15 (a) High-magnification SEM image of a GR. The darkness contrast at the center region is shown. (b) SAED pattern of multilayer GR at the contrast region, indicating that the multilayer GR is a single crystal even though its thickness is not uniform. (c) Cross-sectional TEM image of the GR at the central region. We see that the central region is the thickest and the thickness gradually decreases along the normal to the growth direction. Also, we know that adlayers were grown on the top of the graphene layer, different from the conventional CVD growth of multilayer graphene (islands).³² (d) Schematic image of a multilayer GR showing the growth sequence of adlayers. Cross-sectional TEM images show that the thickness is maximum at the center of a multilayer GR gradually decreased on both sides normal to the ribbon direction. One possible reason for this is that the particle moved in the vicinity of the

center during the growth. As the ribbon grows, carbon adatoms coming from the particle would have to migrate longer distances to attach to the graphene edges. We suggest they do not contribute to edge growth and that, also, the thickness of the adlayers is reduced along the direction normal to the long axis of the GR.

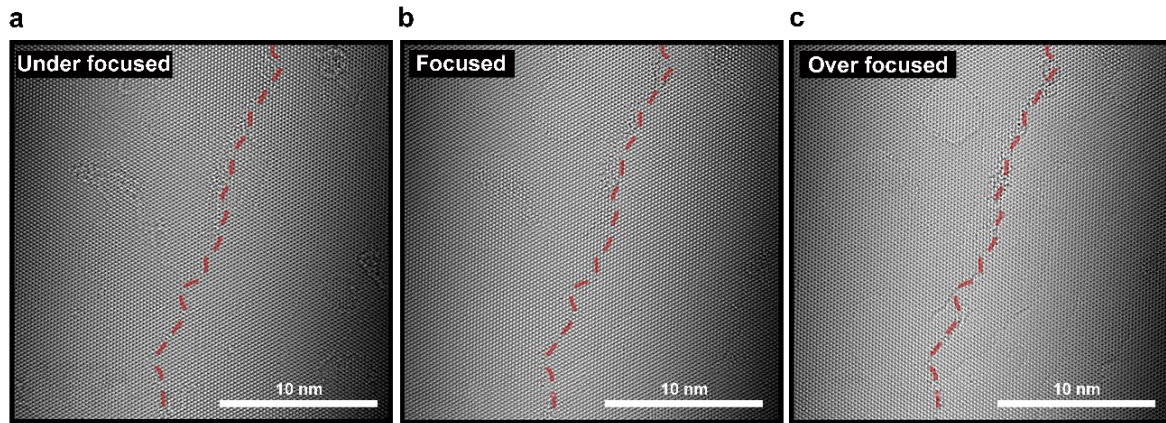


Figure 4.16 HRTEM images of the GR at the contrast region shown in the **Figure 4.15b** at (a) under-focused, (b) focused and (c) over- focused conditions. This proves that the darkness contrast of multilayer GR at the center is due to the layer number difference.

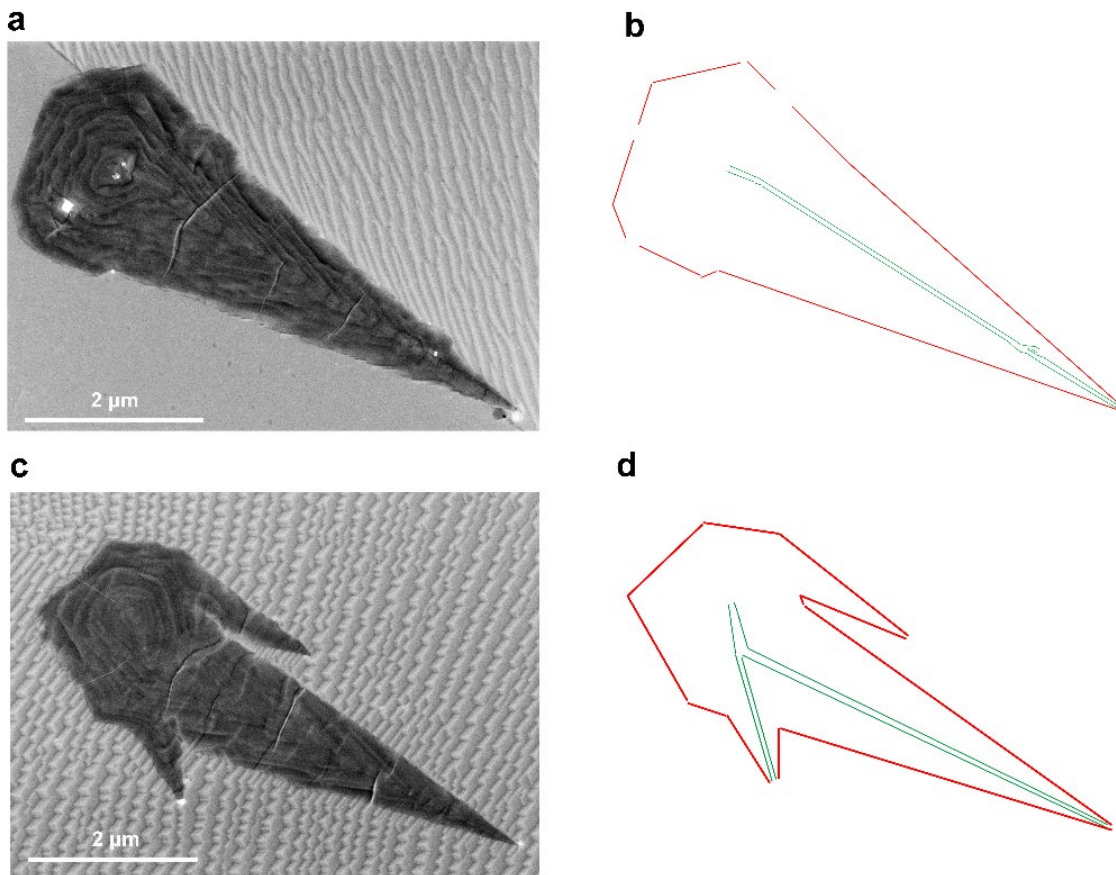


Figure 4.17 (a) SEM image of a multilayer GR with one particle connected to it. (b) The green line in the schematic shows the “contrast region” in the ribbon. (c) SEM image of multilayer GRs connected to two particles. The two particles were formed through the division of a single particle during the growth process. (d) Diagram of the “contrast region” in the ribbon, highlighted by the green line.

This trend was also found from cross-sectional TEM of a multilayer GR (**Figures 4.15-4.16**) which showed that adlayers were grown on top of a graphene layer to form a wedding cake-type structure, opposite to what is usually observed in conventional CVD growth of multilayer graphene island or films having adlayers (‘inverse wedding cake structure’).³² This growth behavior suggests that the carbon adatoms that come from the particle led to the longitudinal growth of adlayers, that can then grow laterally at their edges by VS growth. **Figure 4.17** shows the SEM image of a multilayer GR. The center of the multilayer graphene ribbon is thicker as indicated by the increased contrast. Since the GR adlayers likely grew from the particle that provided carbon adatoms, the increased thickness at the center is an indication of the path of the particle’s movement during growth. The contrast in **Figure 4.10d** also clearly shows the path of the particle during growth. We conclude that the GR nucleated at the particle’s initial position, after which the longitudinal growth was governed by the movement of the particle on the substrate.

Figure 4.10c suggests that the GR became wider after $^{13}\text{CH}_4$ gas was introduced (also shown in **Figure 4.18** for another GR). This indicates that there could be two parallel processes that contribute to GR growth: the lengthening of the ribbon is due to particle-mediated growth (VLS growth) and the deposition of carbon adatoms at the Cu(111) surface adjacent to the sides of the ribbon that cause the ribbon to increase in width. This latter process is “vapor-solid” (VS) growth. A schematic of the overall growth process is presented in **Figure 4.10e** and summarized as follows: the nucleation of the GR occurs at the particle, which we assume, should be at the initial position of the particle. As the ribbon grows longer, the particle is found to move on the substrate. Simultaneously, the two edges also add C atoms due to catalysis of $^{13}\text{CH}_4$ on the adjacent Cu(111) surface (this can happen only above a certain growth T, see below). The VS growth time thus is the longest at the ribbon end that is farthest from the particle and hence the width is largest at this far end and smallest at the particle. The two parallel processes (VLS growth at the tip and VS growth along the sides) therefore determine the morphology (taper angle) of the ribbon. We will describe this in greater detail later.

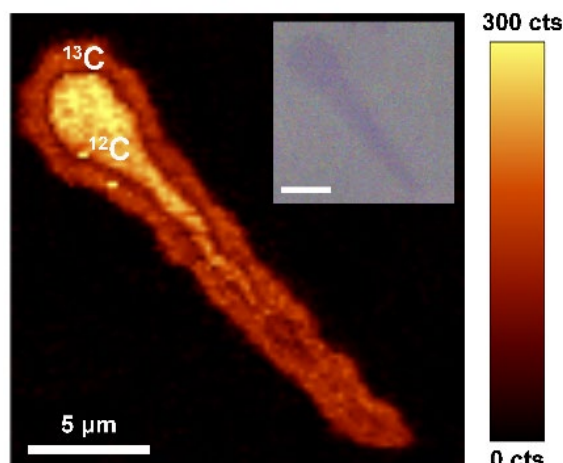


Figure 4.18 Raman map of the G band intensity of a ^{13}C -labelled monolayer GR. The intensity contrast reveals that the GR became wider, and also that particle mediated elongation continued after the ethylene gas was turned off and the $^{13}\text{CH}_4$ gas was then introduced.

4.2.3 Growth of graphene ribbon and its relationship with the Cu foil substrate

To study the relationship between the GR structure and the crystal orientations of the growth substrate, we grew GRs on Cu foils with Cu{101}, Cu{111} and Cu{100} surfaces, which have, respectively, 2-fold, 3-fold and 4-fold symmetry (**Figure 4.19a**). When grown on Cu(101), Cu(-11-1), or Cu(010) certain planes as shown in **Figures 4.19b-d** respectively, GRs invariably grew along the Cu<101> direction regardless of the Cu foil crystal orientations, that is, they showed the 2-fold, 3-fold, and 4-fold symmetry of growth direction on the Cu(101), Cu(-11-1), and Cu(010) planes, respectively. Even when grown on a higher index plane like Cu(1-13) shown in **Figure 4.19e**, the GRs grew along the two Cu<101> directions (at 180 degrees to each other). It is known that epitaxially grown hexagonal graphene islands on Cu foils essentially always align with their zigzag edges parallel to the Cu<110> direction.³³ The preferred orientation of GRs with respect to the crystalline substrate indicates that the growth of GRs on Cu foils is epitaxial. We have marked the growth direction of a GR in **Figure 4.19f**. The SAED pattern suggests that the direction of the long axis of the GR is also parallel to the graphene lattice zigzag directions. Considering the symmetry of the graphene lattice, we suggest two possible growth routes (and we found examples for both of them, see the corresponding SEM images of GRs in **Figures 4.20a-b**): As detailed in **Figures 4.19g-h**, at the nucleation stage the particle could (in principle, that is) either move parallel to the Cu<101> direction or at a (non-zero) angle to them, but in both cases, the growth directions were along the Cu<101> direction and found to be parallel to the graphene lattice zigzag directions. Indeed, the SAED pattern of the edge showed that this GR has the zigzag edge even though the width decreased along the growth direction through atomic steps (**Figure 4.20c**); this is representative of all of the GRs grown.

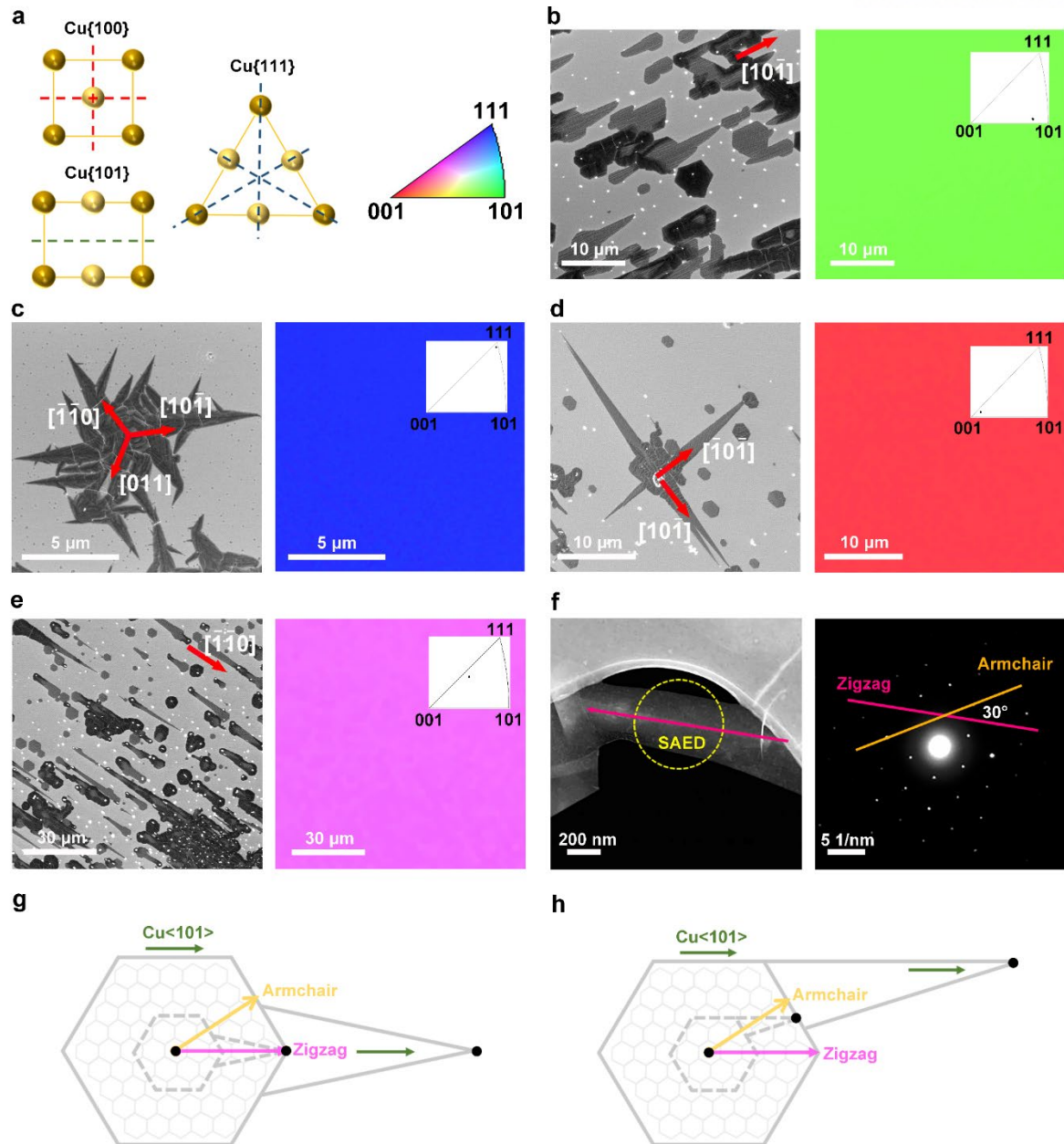


Figure 4.19 (a) Symmetry of different Cu crystal planes. (b-e) SEM images and electron backscatter diffraction (EBSD) maps of GRs grown on (b) Cu(101), (c) Cu(-11-1), (d) Cu(010) and (e) Cu(1-13) planes. (f) High angle annular dark field (HAADF) image and SAED pattern of a GR. (g-h) Schematic images of graphene growth direction with respect to edge type.

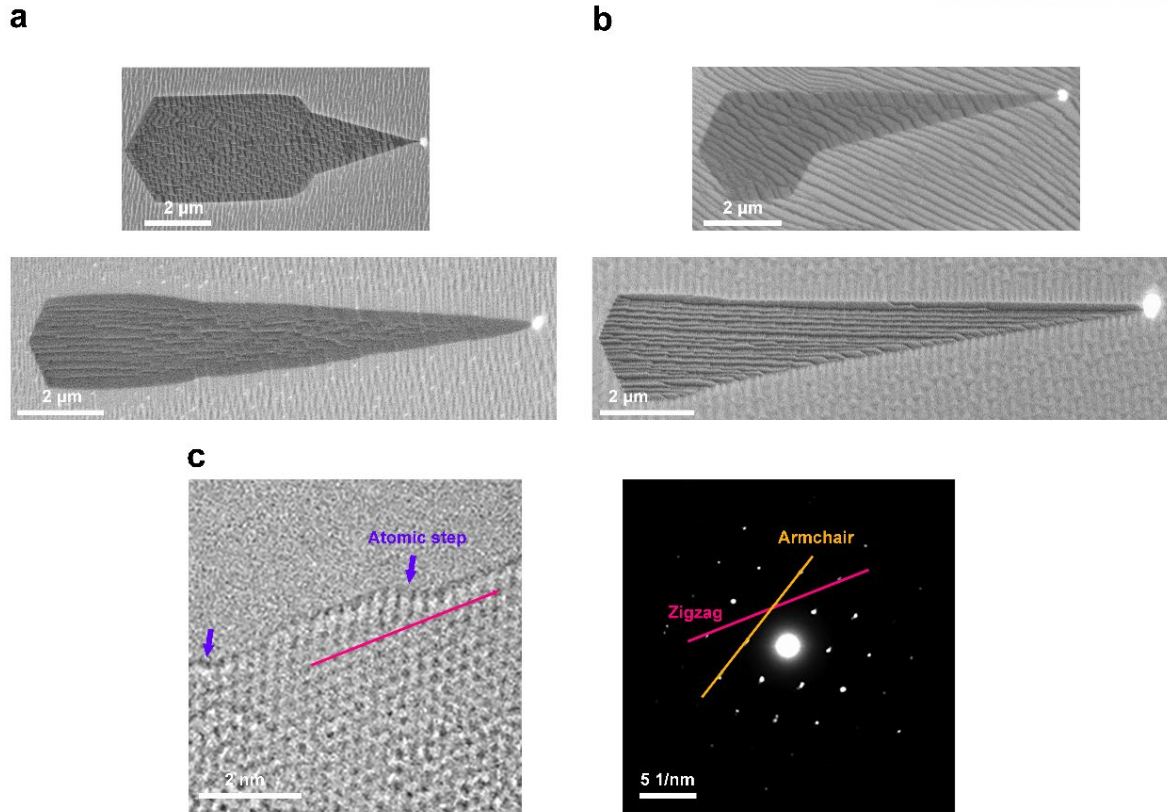


Figure 4.20 (a–b) SEM images of GR growth, showing different start points of the particle. (c) HRTEM atomic image of a GR at the edge region and its SAED pattern. The growth direction of the GR (rose arrow marked in (c)) was strictly along the graphene zigzag direction, as shown in the SAED pattern. It should be noted that there is a small angle between the direction of the ribbon edge and the ribbon growth direction as the GR is needle shaped. The edge of the GR has atomic-scale kinks as shown in (c). This suggests that the needle-shaped ribbon width changes along the growth direction by the formation of atomic-scale kinks. In other words, the GR has zigzag edges with kinks present.

4.2.4 Kinetics analyses of graphene ribbon growth

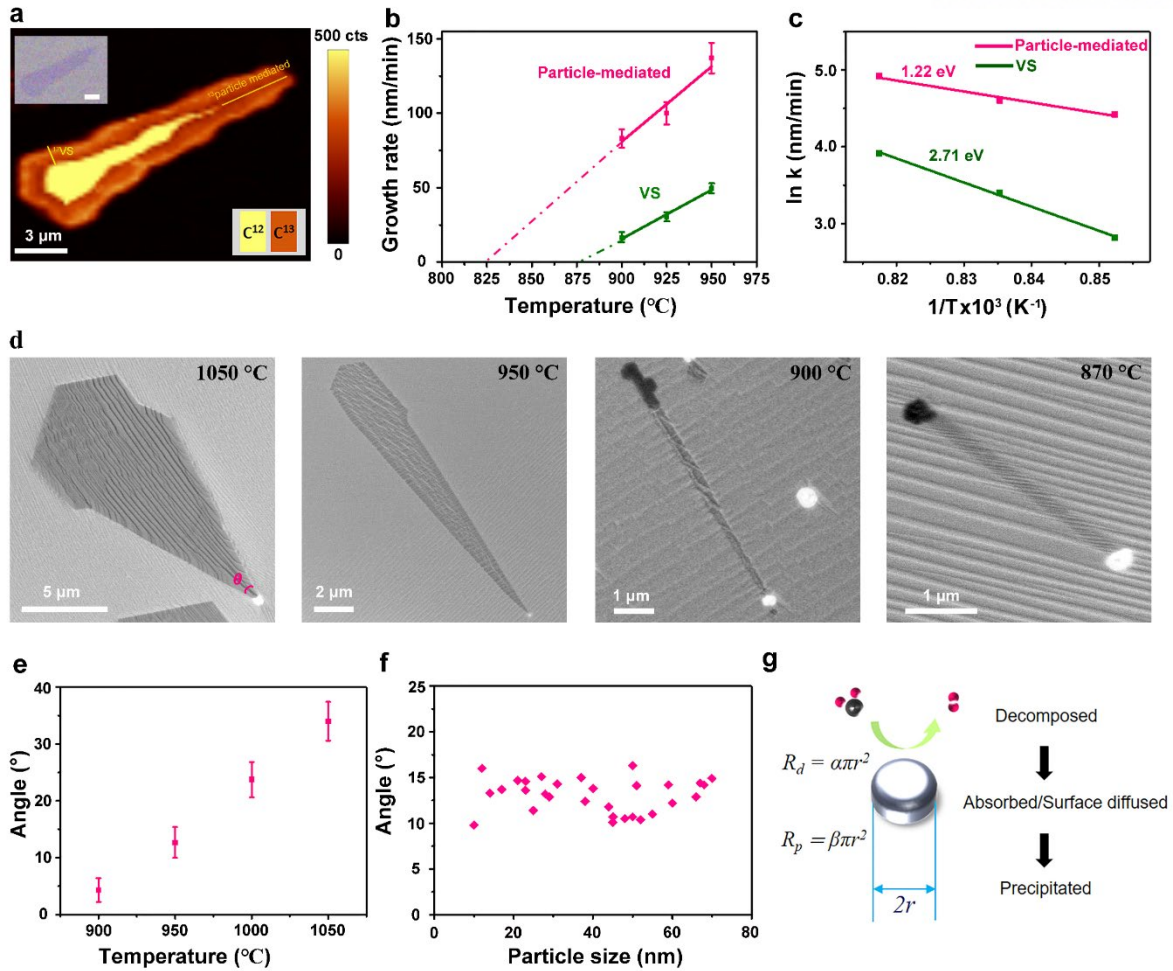


Figure 4.21 (a) Raman G band map of ^{13}C -labelled graphene ribbon grown at 925 °C. (b) The growth rates of *particle-mediated VLS* and *VS* at different growth temperatures. (c) Arrhenius plots for particle mediated growth and VS growth. (d) SEM images of GRs grown at different temperatures. (e) Statistical data of the angle distribution at different growth temperatures. (f) Angle distribution of GRs grown from silica particles of different sizes at 950°C. (g) Schematic image showing surface diffusion mechanism.

To estimate the relative contributions of the two different growth pathways in the growth of a GR, we measured the width and length of the ^{13}C -labelled region of a GR in a Raman G band map, as shown in **Figure 4.21a**. Based on the ratio of length to width (width at the far end—farthest from the particle) of the ^{13}C region for a given growth time period, we extracted the particle-mediated VLS, and VS (that is, edge) growth rates for growth at 925 °C (exposure to ^{13}C was for 40 min). Similarly, we measured the growth rates for each of the two modes at 950 °C (exposure to ^{13}C was for 40 min) and at 900 °C (exposure to ^{13}C was for 30 min). The corresponding Raman G band maps of ^{13}C -labelled GRs are shown in **Figure 4.22**. The particle-mediated VLS and VS growth rates for these three temperatures are

shown in **Table 4.3**. **Figure 4.21b** shows the particle-mediated VLS and VS growth rates for 10 samples obtained at each of the three growth temperatures. The fit values of the activation enthalpies using the Arrhenius equation for particle-mediated VLS and VS-edge growth are 1.22 ± 0.19 eV and 2.71 ± 0.05 eV, respectively (**Figure 4.21c**). Since hexagonal graphene islands are formed in parallel during GR growth, we also did Raman G band mapping for the (concurrently grown) ^{13}C -labelled hexagonal graphene islands; these are shown in **Figure 4.23**. From the width of the ^{13}C -labeled region, we extracted the growth rates of graphene islands at 900 °C, 925 °C, and 950 °C from $^{13}\text{CH}_4$ and these values are listed in **Table 4.4**.

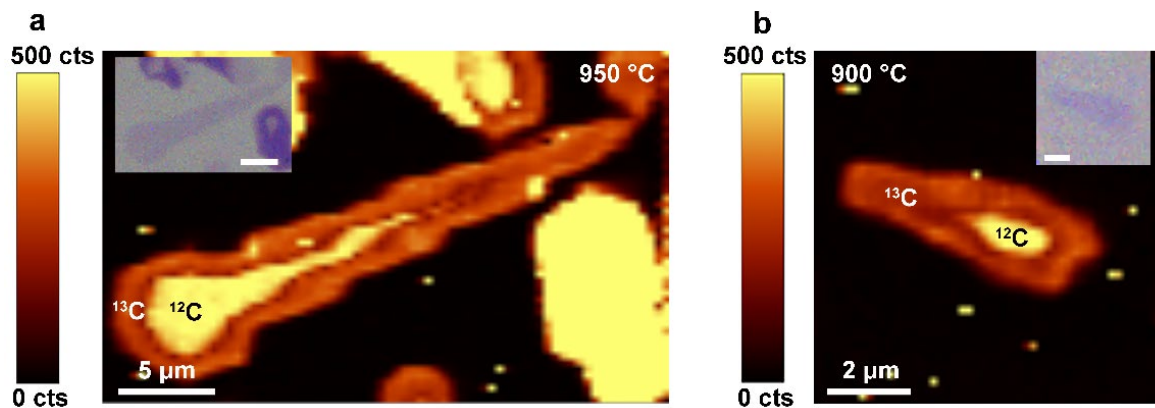


Figure 4.22 Raman G band maps of two different ^{13}C -labelled GRs grown at (a) 950 °C and (b) 900 °C, and then transferred on to 300nm- SiO_2/Si wafer.

Table 4.3 Data from ^{13}C -labelled growths of GRs at different growth temperatures. The fit values of the activation enthalpies using the Arrhenius equation for particle-mediated VLS and VS growth are 1.22 ± 0.19 eV and 2.71 ± 0.05 eV, respectively.

950 °C	Particle-mediated (nm/min)	VS (nm/min)	925 °C	Particle-mediated (nm/min)	VS (nm/min)	900 °C	Particle-mediated (nm/min)	VS (nm/min)
1#	135	45	1#	103	27	1#	86	23
2#	118	43	2#	106	29	2#	68	13
3#	126	52	3#	107	37	3#	86	14
4#	147	52	4#	106	30	4#	88	18
5#	156	55	5#	97	33	5#	84	15
6#	131	49	6#	101	32	6#	78	14
7#	144	52	7#	92	28	7#	91	22
8#	137	49	8#	100	30	8#	87	19
9#	134	48	9#	109	32	9#	85	15
10#	140	51	10#	83	26	10#	80	14
Average	137±3.2	50±1.8	Average	100±2.8	30±1.8	Average	83±2.5	17±1.8

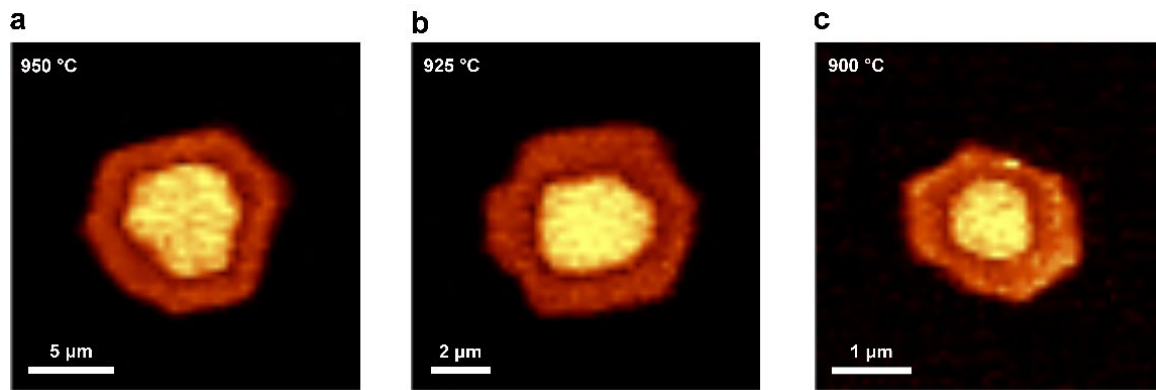


Figure 4.23 (a-c) Raman G band maps of ^{13}C -labelled graphene islands transferred on 300nm-SiO₂/Si wafer grown at 950 °C, 925 °C and 900 °C, respectively. In the absence of silica particles, no GRs were grown. As shown in Figure S4b, graphene islands and GRs coexisted, during ^{13}C -labelled GR growth. Hence, we determined the growth rates of graphene islands and the average growth rates at the different temperatures were same as for the VS growth part of the ribbons. For graphene islands we extracted the activation enthalpy for growth, 2.71 ± 0.06 eV, which matches well with that obtained for the VS portion of growth of the GRs (2.71 ± 0.05 eV).

Table 4.4 Data for five separate ^{13}C -labelled growths of graphene islands at different growth temperatures.

950°C	Growth rate (nm/min)	925°C	Growth rate (nm/min)	900°C	Growth rate (nm/min)
1#	47	1#	29	1#	17
2#	52	2#	26	2#	16
3#	49	3#	33	3#	19
4#	50	4#	30	4#	17
5#	52	5#	31	5#	17
Average	50 ± 1.4	Average	30 ± 1.5	Average	17 ± 1.0

We now turn to a different method of obtaining growth rates that does not rely on C-isotope labeling and Raman mapping. This allows us to find the activation enthalpy from Arrhenius plots, for (i) VLS growth, (ii) GR growth at the sides (i.e., due to VS growth), and (iii) VS growth of graphene islands that as mentioned, appear concurrently with the GRs for certain growth temperatures. (i) **Table 4.5** shows ‘high end’ values for lengths (note that we found many lengths clustered close to the *largest* length value) for the GRs grown *from ethylene*, for growths at 900, 950, and 1000 °C, respectively. From these data we fit an activation enthalpy for VLS growth of 1.74 ± 0.01 eV based on the average of 10 ‘high end values’ at each temperature, and 1.73 ± 0.03 eV based on the largest length at each temperature, which can be compared with 1.22 ± 0.19 eV obtained by examining ^{13}C -labelled GR growth from $^{13}\text{CH}_4$ with Raman mapping as we described above. (ii) The maximum width of tapered GRs (listed in **Table 4.6**) yielded an activation enthalpy of $2.78 \text{ eV} \pm 0.15 \text{ eV}$ for the VS growth at the edges of the GRs. (iii) The maximum “diameter” (vertex to opposing vertex) of the hexagonal islands that grow by the VS mechanism from ethylene at 900, 950, and 1000 °C (see **Table 4.7**) yields 2.85 ± 0.07 eV. The simple method outlined above for obtaining the activation enthalpy without the need for ^{13}C -labeling and Raman mapping should prove very useful in future studies of the kinetics of island or ribbon growth, and for all 2D materials.

Table 4.5 Graphene ribbon lengths for the 10 longest GRs that could be found in SEM images. It shows the length of each the 10 longest GRs at each of 3 different temperatures (900, 950, and 1000 °C), identified from SEM images by evaluating a 1 cm x 1 cm region of the Cu(111) foil that contained *many* GRs. Please note that we also calculated rates of these 10 GRs that were grown on Cu(111) foil under 1% C_2H_4 in Ar(g) *without* ^{13}C -labelling (0.3 SCCM 1% $\text{C}_2\text{H}_4/\text{Ar}$, 300 SCCM H_2 and 500 SCCM Ar, exposed to C_2H_4 for 40 mins at each temperature). It should be noted that even though the growth rate for *all* GRs that are significantly shorter in a given run is not known (the nucleation time at each ribbon

is unknown), we could get the *average growth rate of "high end" values*, and separately, a single *highest growth rate* value at each temperature, from which the activation enthalpy for GR growth was calculated using the Arrhenius equation. Here, we are assuming that the *longest ribbon(s)* (longitudinal growth rate) and the *widest ribbon(s)* (growth at edges of the ribbons by the VS mechanism) nucleated at very close to time zero. The fit value of activation enthalpy for VLS growth is 1.74 ± 0.01 eV for fitting the average of the 10 values, and 1.73 ± 0.03 eV for fitting the largest length only (thus, one length at each temperature). Note that 1.22 ± 0.19 eV obtained for VLS growth from ^{13}C -labelled GR growth involved *continued* growth from $^{13}\text{CH}_4$, not ethylene.

900°C	Length: μm (Growth rate: nm/min)*	950°C	Length: μm (Growth rate: nm/min)	1000°C	Length: μm (Growth rate: nm/min)
1#	5.28 (132)	1#	10.08 (252)	1#	21.50(537)
2#	5.46 (137)	2#	11.27 (282)	2#	23.07(577)
3#	4.69 (117)	3#	10.50(262)	3#	19.81(495)
4#	5.87 (147)	4#	9.80 (245)	4#	18.46(462)
5#	4.21 (105)	5#	12.48 (312)	5#	20.00(500)
6#	5.87 (147)	6#	9.49 (237)	6#	21.46(537)
7#	6.00 (150)	7#	8.89 (222)	7#	18.82(470)
8#	5.00 (125)	8#	8.47 (212)	8#	19.49(487)
9#	5.42 (135)	9#	12.42 (310)	9#	19.80(495)
10#	4.88 (122)	10#	11.67 (292)	10#	20.61(515)
Average	5.27 ± 0.74 (131 ± 3.7)	Average	10.51 ± 1.16 (263 ± 5.8)	Average	20.30 ± 1.15 (508) ± 5.7

*Length divided by 40 mins

Table 4.6 Ribbon maximum width observed in a 1 cm x 1 cm region of Cu(111) foil. It shows the maximum width found for a GR among all GRs examined in SEM images, at each temperature: namely, 7# at 900 °C , 5# at 950 °C and 2# at 1000 °C, that are listed in **Table 4.5** in bold text (the longest are also the widest, as expected). The activation enthalpy of the GR width growth was fit as 2.78 ± 0.15 eV.

Temperature (°C)	Maximum width (μm)	Growth rate* (μm/min)
900	0.914	0.023
950	3.11	0.078
1000	7.87	0.20

*Width divided by 40 min

Table 4.7 Graphene island with maximum diameter. It shows the maximum growth “diameter” (vertex-to-vertex across the hexagon) of the graphene islands at each temperature, from evaluating a 1 cm x 1 cm region with SEM imaging. The activation enthalpy of the graphene island growth is 2.85 ± 0.07 eV.

Temperature (°C)	Maximum diameter (μm)	Highest growth rate (μm/min)
900	0.510	0.013
950	1.75	0.044
1000	4.90	0.12

The ratio of the VS to VLS growth rates is:

$$\frac{v_{vs}}{v_p} = \tan\left(\frac{\theta}{2}\right) \approx \frac{\theta}{2} \quad \text{Eq 4.1}$$

v_{vs} and v_p are the growth rates for VS-edge and particle-mediated VLS growth in Eq 4.1 and θ is the angle of the GR at the tip. In other words, the ratio of growth rates v_{vs}/v_p is $\theta/2$ (using the small angle approximation of $\tan(\theta) = \theta$ in radians). That is, the value of $\tan(\theta)$ is very close to the ratio of the VS-edge and particle-mediated VLS growth rates. At each temperature, the VLS growth rates are higher than the VS growth rates and the different rates (and thus quite different activation enthalpies) means that by varying the growth temperature one can modify the v_{vs}/v_p ratio, or in other words the angle (θ) at the tip end of the GR can be controllably changed by varying just the temperature. **Figure 4.21d** shows GRs grown at different temperatures. When we decreased the growth temperature, the angle (θ) became smaller, and at 870 °C instead of tapering in the form of a needle, the width of the GR was uniform; it is of interest that at 870 °C no graphene islands grew: VS growth is “turned off”. **Figure 4.21e** shows the angle (θ) for 10 GRs grown at each of the 4 indicated temperatures and one sees that θ

is smaller as growth temperature decreases. At growth temperatures below 900 °C, GRs with uniform width can be synthesized; thus VS growth occurs at temperatures above 900 °C for the growth times and conditions used here. SEM images of GRs grown at 860 °C, 930 °C, and 1000 °C, (**Figure 4.24**) further illustrate this control of ribbon morphology (note that a higher areal density of primarily uniform-width GRs was obtained when we increased the flow rate of C₂H₄, up to 0.8 SCCM, please see **Figure 4.25**). At temperatures ≤ 850 °C, no GRs (or graphene islands) were grown on the time scale of our experiments: both VLS and also VS growth are “turned off”. It is likely that at 850 °C, the particle does not form a molten/semi-molten alloy which, as we learn from our experiments, is indispensable for particle-mediated VLS growth. Comparison TEM-EDS studies of pristine silica particles and silica particles after trying to grow GR at 850 °C, shown in **Figure 4.26**, suggest that the composition of the particle did not change (within the limit of experimental error). In other words, the particle did not form an alloy(s) with Cu at 850 °C.

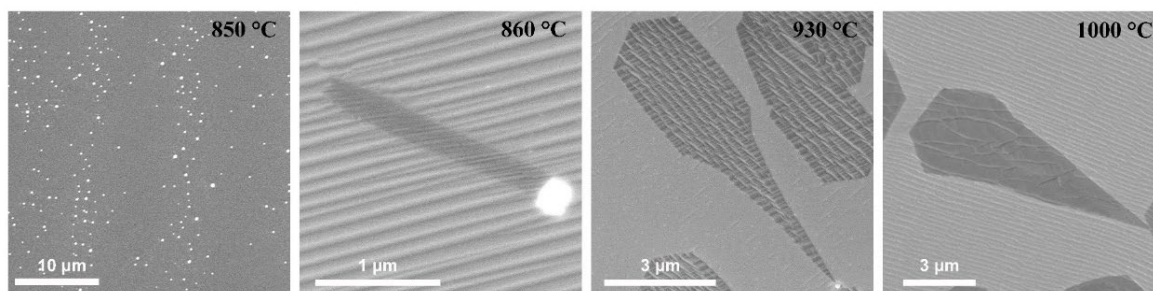


Figure 4.24 Morphology of GRs grown at different temperatures. At 850 °C, no graphene ribbons/islands were grown on the Cu foil. At 860 °C, the angle is close to 0°, showing that VS growth does not occur at this temperature. With only VLS growth, uniform width GRs grow under these conditions.

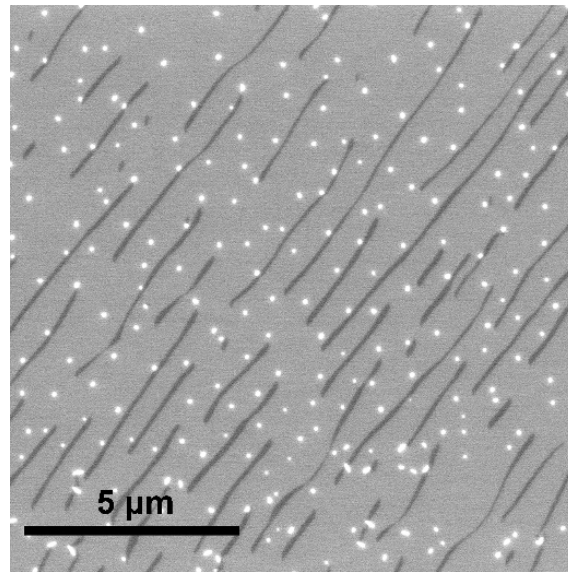
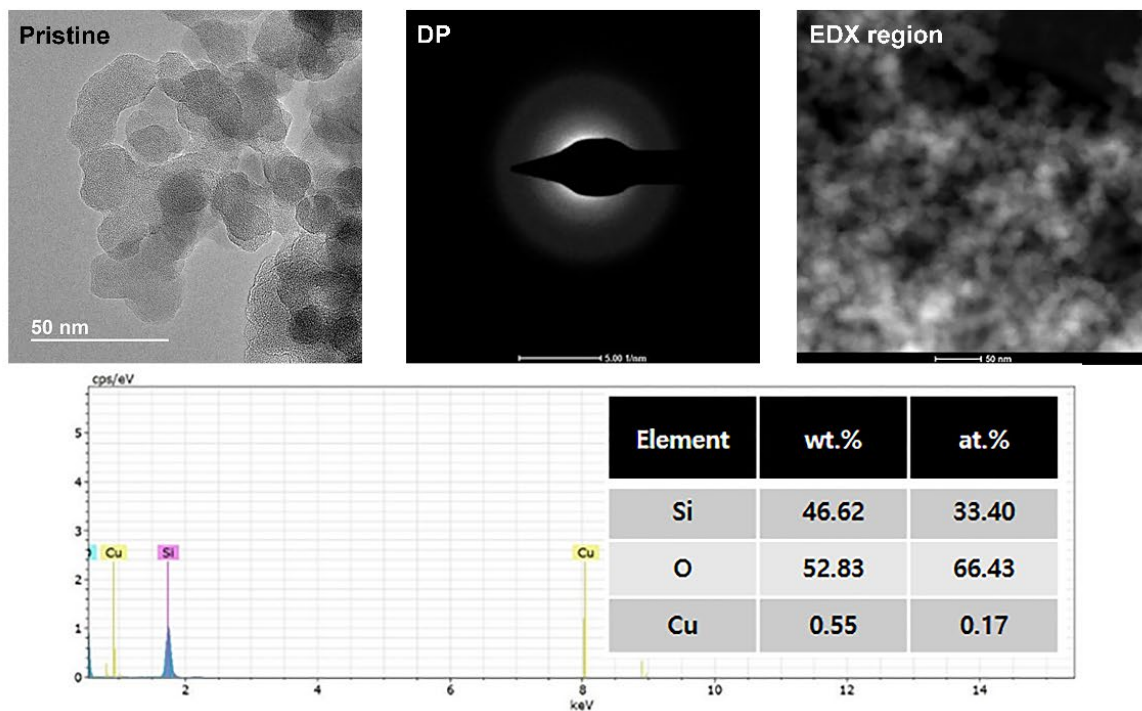


Figure 4.25 SEM image of GRs grown at 880 °C with 0.8 SCCM 1% C₂H₄ diluted in Ar, 500 SCCM Ar, and 250 SCCM H₂ for 1 hour. Note that a higher areal density of GRs is obtained.

a



b

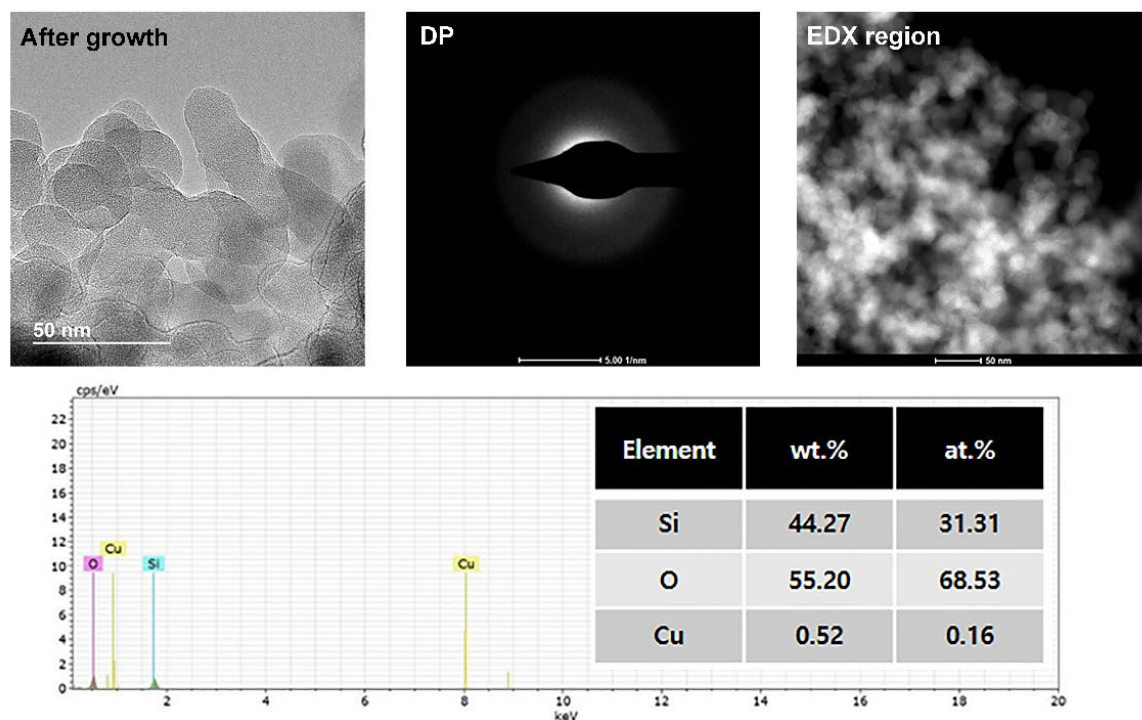


Figure 4.26 TEM and EDS study of (a) pristine silica particle and (b) silica particle after trying to grow GRs at 850 °C. TEM and diffraction patterns suggest that the shape of the silica particle does not change at 850 °C. The composition of the particle (as determined from EDS element analysis) also shows no change. We note here that the Cu line in the spectrum has been artificially introduced *only to verify the presence of Cu if any* and therefore, the corresponding yellow line segments are deliberately introduced

artifacts. The actual result suggests that the Cu signal should be at the level of background noise. In other words, the particle did not form any copper alloy(s) at 850 °C.

Two growth models have been used to explain particle-mediated growth by VLS.³⁴ In one, the particle is first saturated with carbon (or another element) in its bulk (i.e., throughout its interior) which then precipitates. The precipitated carbon is the growing nanostructure—such as a nanotube. In another growth mode the carbon precursor diffuses only at the surface of the particle, which then acts as the carbon source for particle-mediated growth. Note that the growth rate is either *dependent* on the particle size (bulk diffusion), or *independent* of the particle size (surface diffusion).³⁵⁻³⁷ In the case where carbon atoms diffuse through the bulk of the particle, the diffusion rate (R_d) is proportional to the volume (r^3) of the particle ($2r$ is the effective particle diameter). The precipitation rate (R_p) of carbon on the other hand, is proportional to the effective particle area (r^2). The particle-mediated growth rate depends on $R_d / R_p \propto r^3 / r^2 = r$, i.e., the particle diameter. When carbon diffuses only or primarily at the surface of the particle, the diffusion rate (R_d) is proportional to the effective area (r^2) of particle, and the precipitation rate (R_p) of carbon is also proportional to the effective area of particle (r^2) and as a result, the particle-mediated growth rate is independent of the particle size. We mentioned earlier that the angle ($\theta/2$) is determined by the ratio of VS-edge growth to particle-mediated rates. **Figure 4.21f** shows that θ does *not* depend on the particle size for growth at 950 °C. This indicates that the carbon building the GR by VLS diffused at *the surface* of the particle. **Figure 4.21g** shows the schematic of the surface diffusion model in which α and β are constant coefficients. The growth rate was found to be independent of the particle size, which demonstrates that a surface diffusion particle-mediated growth model and not bulk diffusion, is correct.

4.3 Conclusion

High-quality single crystal monolayer/multilayer graphene ribbons (GRs) were grown by first depositing silica nanoparticles on single crystal Cu foil substrates, primarily on Cu(111) foil. SEM/TEM-EDS and ToF-SIMS showed that a Cu-Si-O molten/semi-molten alloy (possibly also containing C, including on its surface) was probably formed that guided the growth of the GRs. We discovered that the growth directions of the GRs are *always* along the Cu<101> direction irrespective of the surface orientation of the substrate (as observed on Cu(111) foils, and heat-treated Cu foils with large grains; the large grains had (101), (100), and (1-13) surface orientation). The ‘wedding cake structure’ of the multilayer GRs is a result of the catalytic particle “laying down” carbon in the form of graphene layers in the central region of the ribbon. The longitudinal growth rate of the GRs was independent of the particle size, suggesting a surface diffusion versus bulk diffusion delivery of carbon for GR longitudinal growth. Based on ¹³C-labelling and kinetics studies, we propose a surface diffusion

particle-mediated VLS growth model to describe the longitudinal growth of GRs, and that if growth occurs along the sides, it is by vapor solid (VS) growth from decomposition of the hydrocarbon precursor on the bare Cu surface adjacent to the elongating GR. By controlling the growth temperature, we were able to change the morphology of GRs from needle shape to rectangular—and to achieve fine control of the “taper” angle. We note that our method provides the possibility of growing GR (sub-10nm) on Cu(111) foil, which if achieved can open a bandgap by the quantum confinement effect.^{1,38} Since the VLS (VSS) growth mechanism allows growth of CNTs³⁹ or other nanoribbons^{14,15,40} on dielectric substrates, it is possible that our method will allow growth on dielectric substrates; further study of this is indicated. Finally, pertaining to growth and kinetics, we use a very simple method to obtain the enthalpy of activation without ¹³C-labeling and thus without Raman mapping, that is based on assuming that the largest structures found (here, islands and ribbons) nucleated at time zero, and grew continuously throughout the exposure time to ethylene. This is supported by having many of the ‘high end’ values for length (VLS) or width (VS) of GRs clustering near a single maximum value, and for size of large graphene islands (VS) clustering near a single maximum value, for each growth temperature.

Some possible uses of these single crystal GRs include graphene-enhanced Raman scattering^{41,42} for specific molecular recognition, such as for in vitro diagnostic testing sensors^{43,44} and in lateral flow assays.⁴⁵ They might be useful in nano-photonics applications,⁴⁶⁻⁴⁹ including devices whose characteristics depend on the taper angle, and others likely to be invented.

4.4 Experimental section

4.4.1 Materials and chemicals

Cu foil (Nilaco, 50 μm thick, 99.98% purity); Silica particles (Skyspring Nanomaterials, Inc.; Lot# 6808-100417); 30% Hydrogen peroxide (H₂O₂) (CAS: No.7722-84-1, Daejung chem, South Korea); 37% hydrochloric acid (HCl) (CAS: 7647-01-0, Daejung chem, South Korea); poly methyl methacrylate (PMMA) (Micro chem, 950 PMMA C4, Lot# 17030195); Acetone (C₃H₆O) (CAS: No. 67-64-1, Daejung chem, South Korea); Ethanol(C₂H₆O) (CAS: No. 64-17-5, Daejung chem, South Korea).

4.4.2 Detailed methods

GR-FETs fabrication and Electrical measurements: GRs were transferred onto 1-cm² pieces of 300 nm SiO₂/Si substrates. First, electron beam lithography was used to pattern drain and source electrodes, after which 5 nm Cr/ 45 nm Au were deposited using an e-beam evaporator. A probe station equipped with a Keithley 4200SCS system was used to test the GFETs in air at room temperature (300 K). A low

temperature Lakeshore CRX-4K system equipped with Keithley 4200SCS system was used for measurements in vacuum (2.4×10^{-6} mbar) at 10K.

Statistical Analysis: The angle (θ) shown in Figure 4d, was measured three separate times by a protractor function in our SEM (an average was thereby obtained with std dev <0.6 degree). Then the overall averaged values were obtained by using the “mean \pm SD” function in *Microsoft Excel* and drawing of the figure using *Origin* software. The angle (θ) shown in Figure 4e, was measured 3x by a protractor function in SEM (average, std dev <0.8 degree), then the mean values in the figure were plotted.

References

- [1] M. Y. Han, B. Ozyilmaz, Y. B. Zhang, P. Kim, *Phys. Rev. Lett.* **2007**, *98*, 206805.
- [2] W. J. Yu, S. H. Chae, D. Perello, S. Y. Lee, G. H. Han, M. Yun, Y. H. Lee, *Acs Nano* **2010**, *4*, 5480.
- [3] H. Chen, Y. M. Lin, M. J. Rooks, P. Avouris, *Physica E* **2007**, *40*, 228.
- [4] J. B. Park, W. Xiong, Y. Gao, M. Qian, Z. Q. Xie, M. Mitchell, Y. S. Zhou, G. H. Han, L. Jiang, Y. F. Lu, *Appl. Phys. Lett.* **2011**, *98*, 123109.
- [5] L. Y. Jiao, L. Zhang, X. R. Wang, G. Diankov, H. J. Dai, *Nature* **2009**, *458*, 877.
- [6] D. V. Kosynkin, A. L. Higginbotham, A. Sinitskii, J. R. Lomeda, A. Dimiev, B. K. Price, J. M. Tour, *Nature* **2009**, *458*, 872.
- [7] M. Sprinkle, M. Ruan, Y. Hu, J. Hankinson, M. Rubio-Roy, B. Zhang, X. Wu, C. Berger, W. A. de Heer, *Nat. Nanotechnol.* **2010**, *5*, 727.
- [8] L. Cai, W. Z. He, X. D. Xue, J. Y. Huang, K. Zhou, X. H. Zhou, Z. P. Xu, G. Yu, *Natl. Sci. Rev.* **2021**, *8*.
- [9] H. Sun, F. Liu, L. Zhang, B. McLean, H. An, M. Huang, M. Willinger, R. S. Ruoff, Z. Wang, F. Ding, (*preprint*) *arXiv.org*, 2201.00684, v1, submitted: 1, **2022**.
- [10] C. C. Chen, C. C. Yeh, C. H. Chen, M. Y. Yu, H. L. Liu, J. J. Wu, K. H. Chen, L. C. Chen, J. Y. Peng, Y. F. Chen, *J. Am. Chem. Soc.* **2001**, *123*, 2791.
- [11] D. Tsivion, M. Schwartzman, R. Popovitz-Biro, P. von Huth, E. Joselevich, *Science* **2011**, *333*, 1003.
- [12] R. S. Wagner, W. C. Ellis, *Appl. Phys. Lett.* **1964**, *4*, 89.
- [13] S. N. Mohammad, *Nano Lett.* **2008**, *8*, 1532.
- [14] S. S. Li, Y. C. Lin, W. Zhao, J. Wu, Z. Wang, Z. H. Hu, Y. D. Shen, D. M. Tang, J. Y. Wang, Q. Zhang, H. Zhu, L. Q. Chu, W. J. Zhao, C. Liu, Z. P. Sun, T. Taniguchi, M. Osada, W. Chen, Q. H. Xu, A. T. S. Wee, K. Suenaga, F. Ding, G. Eda, *Nat. Mater.* **2018**, *17*, 535.
- [15] X. F. Li, B. C. Li, J. C. Lei, K. V. Bets, X. H. Sang, E. Okogbue, Y. Liu, R. R. Unocic, B. I. Yakobson, J. Hone, A. R. Harutyunyan, *Sci. Adv.* **2021**, *7*.
- [16] X. J. Weng, R. A. Burke, J. M. Redwing, *Nanotechnology* **2009**, *20*, 085610.
- [17] J. T. Huang, Z. H. Huang, S. Yi, Y. G. Liu, M. H. Fang, S. W. Zhang, *Sci. Rep.* **2013**, *3*, 3504.
- [18] H. Y. Tuan, D. C. Lee, B. A. Korgel, *Angew. Chem. Int. Edit.* **2006**, *45*, 5184.
- [19] C. B. Maliakkal, D. Jacobsson, M. Tornberg, A. R. Persson, J. Johansson, R. Wallenberg, K. A. Dick, *Nat. Commun.* **2019**, *10*, 4577.
- [20] R. M. Jacobberger, M. S. Arnold, *Chem. Mater.* **2013**, *25*, 871.
- [21] A. Eckmann, A. Felten, I. Verzhbitskiy, R. Davey, C. Casiraghi, *Phys. Rev. B.* **2013**, *88*, 035426.
- [22] L. Gan, Z. T. Luo, *Acs Nano* **2013**, *7*, 9480.
- [23] S. Kim, J. Nah, I. Jo, D. Shahrjerdi, L. Colombo, Z. Yao, E. Tutuc, S. K. Banerjee, *Appl. Phys. Lett.* **2009**, *94*, 062107.
- [24] M. H. Tajarro, H. R. Saghai, *Beilstein J. Nanotech.* **2015**, *6*, 2062.
- [25] C. G. Kang, J. W. Kang, S. K. Lee, S. Y. Lee, C. H. Cho, H. J. Hwang, Y. G. Lee, J. Heo, H. J. Chung, H. Yang, S. Seo, S. J. Park, K. Y. Ko, J. Ahn, B. H. Lee, *Nanotechnology* **2011**, *22*, 295201.
- [26] I. Martin-Fernandez, D. B. Wang, Y. G. Zhang, *Nano Lett.* **2012**, *12*, 6175.
- [27] D. B. Wang, H. Tian, Y. Yang, D. Xie, T. L. Ren, Y. G. Zhang, *Sci. Rep.* **2013**, *3*, 1348.
- [28] L. X. Chen, H. M. Wang, S. J. Tang, L. He, H. S. Wang, X. J. Wang, H. Xie, T. R. Wu, H. Xia, T. X. Li, X. M. Xie, *Nanoscale* **2017**, *9*, 11475.
- [29] D. Luo, M. H. Wang, Y. Q. Li, C. Kim, K. M. Yu, Y. H. Kim, H. J. Han, M. Biswal, M. Huang, Y. Kwon, M. Goo, D. C. Camacho-Mojica, H. F. Shi, W. J. Yoo, M. S. Altman, H. J. Shin, R. S. Ruoff, *Adv. Mater.* **2019**, *31*, 1903615.
- [30] B. Hallstedt, *Calphad* **1992**, *16*, 53.

- [31] O. H., *J. Phase Equilib.* **2002**, *23*, 281.
- [32] M. Huang, P. V. Bakharev, Z. J. Wang, M. Biswal, Z. Yang, S. Jin, B. Wang, H. J. Park, Y. Q. Li, D. S. Qu, Y. Kwon, X. J. Chen, S. H. Lee, M. G. Willinger, W. J. Yoo, Z. Lee, R. S. Ruoff, *Nat. Nanotechnol.* **2020**, *15*, 289.
- [33] A. T. Murdock, A. Koos, T. Ben Britton, L. Houben, T. Batten, T. Zhang, A. J. Wilkinson, R. E. Dunin-Borkowski, C. E. Lekka, N. Grobert, *Acs Nano* **2013**, *7*, 1351.
- [34] S. Hofmann, G. Csanyi, A. C. Ferrari, M. C. Payne, J. Robertson, *Phys. Rev. Lett.* **2005**, *95*, 036101.
- [35] R. T. K. Baker, M. A. Barber, R. J. Waite, P. S. Harris, F. S. Feates, *J. Catal.* **1972**, *26*, 51.
- [36] M. Song, Y. T. Zhang, J. Chun, S. Y. Hu, M. Tang, D. S. Li, *Nanoscale* **2020**, *12*, 7538.
- [37] E. I. Givargizov, *J. Cryst. Growth* **1975**, *31*, 20.
- [38] X. R. Wang, Y. J. Ouyang, X. L. Li, H. L. Wang, J. Guo, H. J. Dai, *Phys. Rev. Lett.* **2008**, *100*, 206803.
- [39] E. F. Kukovitsky, S. G. L'vov, N. A. Sainov, *Chem. Phys. Lett.* **2000**, *317*, 65.
- [40] A. Aljarb, J. H. Fu, C. C. Hsu, C. P. Chuu, Y. Wan, M. Hakami, D. R. Naphade, E. Yengel, C. J. Lee, S. Brems, T. A. Chen, M. Y. Li, S. H. Bae, W. T. Hsu, Z. Cao, R. Albaridy, S. Lopatin, W. H. Chang, T. D. Anthopoulos, J. Kim, L. J. Li, V. Tung, *Nat. Mater.* **2020**, *19*, 1300.
- [41] V. Vales, K. Drogowska-Horna, V. L. P. Guerra, M. Kalbac, *Sci. Rep.* **2020**, *10*, 4516.
- [42] S. X. Huang, X. Ling, L. B. Liang, Y. Song, W. J. Fang, J. Zhang, J. Kong, V. Meunier, M. S. Dresselhaus, *Nano Lett.* **2015**, *15*, 2892.
- [43] A. J. Driscoll, M. H. Harpster, P. A. Johnson, *Phys. Chem. Chem. Phys.* **2013**, *15*, 20415.
- [44] B. R. Goldsmith, L. Locascio, Y. N. Gao, M. Lerner, A. Walker, J. Lerner, J. Kyaw, A. Shue, S. Afsahi, D. Pan, J. Nokes, F. Barron, *Sci. Rep.* **2019**, *9*, 434.
- [45] M. B. Lerner, D. Pan, Y. N. Gao, L. E. Locascio, K. Y. Lee, J. Nokes, S. Afsahi, J. D. Lerner, A. Walker, P. G. Collins, K. Oegema, F. Barron, B. R. Goldsmith, *Sensor Actuat. B-Chem.* **2017**, *239*, 1261.
- [46] Y. Y. Dai, X. L. Zhu, N. A. Mortensen, J. Zi, S. S. Xiao, *J. Optics* **2015**, *17*, 065002.
- [47] C. Yang, R. K. Chen, Y. P. Jia, L. W. Guo, J. N. Chen, *Chinese Phys. B.* **2017**, *26*, 074220.
- [48] Q. Y. Xu, T. Ma, M. Danesh, B. N. Shivananju, S. Gan, J. C. Song, C. W. Qiu, H. M. Cheng, W. C. Ren, Q. L. Bao, *Light-Sci. Appl.* **2017**, *6*, e16204.
- [49] J. N. Chen, M. Badioli, P. Alonso-Gonzalez, S. Thongrattanasiri, F. Huth, J. Osmond, M. Spasenovic, A. Centeno, A. Pesquera, P. Godignon, A. Z. Elorza, N. Camara, F. J. G. de Abajo, R. Hillenbrand, F. H. L. Koppens, *Nature* **2012**, *487*, 77.
- [50] S. Jin, M. Huang, Y. Kwon, L. N. Zhang, B. W. Li, S. Oh, J. C. Dong, D. Luo, M. Biswal, B. V. Cunning, P. V. Bakharev, I. Moon, W. J. Yoo, D. C. Camacho-Mojica, Y. J. Kim, S. H. Lee, B. Wang, W. K. Seong, M. Saxena, F. Ding, H. J. Shin, R. S. Ruoff, *Science* **2018**, *362*, 1021.

Perspective

In our work, we studied the dissolution of single crystal diamond (100) and (110) in Ni and Co films. We understood the kinetics of diamond dissolving in the presence of water vapor. As we can precisely control the dissolution rates, then a thin diamond film can be formed through properly controlled. So, this method provides an alternative option to prepare thin diamond films. However, continuous diamond dissolution is available in the presence of water vapor, whereas it's hard to form flat surface for specific uses. Even though the dissolution rate is much faster than conventional RIE technique, but RIE does form flat surface, which is applicable for further uses. Following this idea, we are thinking about some other method to optimize the condition or replace water vapor but form flat structures and maintain high dissolution rate.

On the other hand, micrometer sized graphene ribbon was synthesized by vapor-liquid-solid growth mechanism and the taper angle could be controlled primarily by the growth temperature. However, since the width of graphene ribbon is larger than 200 nm, we cannot open the bandgap of it. To open the bandgap, we need to decrease the width for monolayer graphene ribbon. So, the challenging is how to decrease the width of it. 20 nm sized silica particle was used in our study. Perhaps a narrower graphene ribbon could be synthesized if we use smaller sized silica particle. Besides, since the growth of graphene ribbon was catalyzed by the silica particle, potentially we can grow graphene ribbon on dielectric substrate with silica particle assistance. The future work we are planning to do is growing narrower graphene ribbon to open the bandgap or growing graphene ribbon on dielectric substrate.

Acknowledgement

First of all, with my greatest respect to my advisor, Prof. Rodney Scott Ruoff, I appreciate his guidance and encouragement in the past four years. Thank you for giving me the freedom environment and excellent platform for scientific research. I learned more about how to find the problems, how to solve the problems and how to be a researcher.

Then, I would like to thank to Dr. Pavel V. Bakharev and Dr. Sunghwan Jin who taught me during the research. I also thank to Dr. Sunghwan Jin for teaching me something about research life. And I would like to thank to the group members for their help and accompany in my daily life.

I also thank to Myeonggi Choe, Yongchul Kim, Prof. Zonghoon Lee, Prof. Tae Joo Shin and Prof. Geunsik Lee for their valuable contributions and good collaborations during my research. Besides, I would like to appreciate the UCRF faculties: Kang O Kim, Goh Myeong Bae, Hyung Il Kim, Daehye Lee, Kyungsun Lee, Sunyi Lee and Mi Sun Cho for their attention and patient help in my work.

Furthermore, I would like to thank to my qualifying exam committee members: Prof. Feng Ding and Prof. Hyung-Joon Shin for their attendance and for their valuable comments and suggestions. And I would like to thank to my PhD defense committee members: Prof. Geunsik Lee, Prof. Tae Joo Shin, Prof. Hyung-Joon Shin and Prof. Zonghoon Lee.

Finally, I sincerely appreciate my parents, my girlfriend and my friends. Thanks for encouraging me and giving me your help when I felt tired and depressed, and also thanks for sharing the happiness with me during these years.